MAGNETIC HEAD FLYABILITY ON PATTERNED MEDIA

A Thesis
Presented to
The Academic Faculty

By

Brian David Horton

In Partial Fulfillment
of the Requirements for the Degree
Master's of Science in Mechanical Engineering

Georgia Institute of Technology
July 2004

MAGNETIC HEAD FLYABILITY ON PATTERNED MEDIA

Approved:

Jeffrey Streator, Ph.D., Advisor

Itzhak Green, D.Sc.

Peter Hesketh, Ph.D.

Date Approved: 6 July 2004

ACKNOWLEDGEMENTS

I would like to say thank you to everyone who has supported, helped and guided me in completing this work.

First, thank you to my parents, Ken and Vicki Wheeler and Dave Horton. You have been my strongest supporters in this and every other major decision in my life. Thank you to my good friend Peter Grant for your thoughts when no one else was awake to ask. Thank you for planting the seed which led to my graduate studies at Georgia Tech. Thank you to Rob Jackson for sharing your knowledge and opinions on my thesis work and class work. Thank you for giving your friendship.

Thank you to Professor Bill King for overseeing the nano-patterning process and opening your laboratory for the work. Thank you to Harry Rowland for your dedication to making the nano-patterning successful on a tight schedule. Thank you to John Graham for making parts and teaching me how to make the machined components of the test stand. Thank you to Christina Freyman for your FIB patterning work.

Thank you to Professor Itzhak Green and Professor Peter Hesketh for providing feedback and serving on my reading committee. A special thank you goes to my advisor, Professor Jeff Streator, for your support, help and guidance. You have made this experience both challenging and enjoyable.

Financial support for this work was provided by The National Science Foundation through grant number CMS – 0205069.

TABLE OF CONTENTS

ACKNOWLEDGEMENTS iii

LIST OF FIGURES vii

LIST OF TABLES x

SUMMARY xi

CHAPTER 1 Introduction 1

1.1 Motivation 1

1.2 Industrial Application 1

1.3 Objective 2

CHAPTER 2 Literature review 4

2.1 Data Degradation 4

2.1.1 Superparamagnetism 4
2.1.2 Exchange Coupling 5

2.2 Data Storage above the Superparamagnetic Limit 5

2.2.1 Thermomagnetic Recording 5
2.2.2 Perpendicular Recording 6
2.2.3 Patterned Media 7
2.2.3.1 Non-Masked Patterning 7
2.2.3.1.1 Electron Beam Lithography 7
2.2.3.1.2 Focused Ion Beam Lithography 8
2.2.3.2 Masked Patterning 9
2.2.3.2.1 Self Assembled Masking 9
2.2.3.2.2 Other Masking Techniques 12

CHAPTER 3 Apparatus 15

3.1 Primary Systems 15

3.1.1 Data Acquisition System 20
3.1.2 Drive System 23
3.1.3 Positioning System 24

3.2 Sensors 24

3.2.1 Strain Gages 25
3.2.2 Capacitance Sensor 29
3.2.3 Acoustic Emission Sensor 33
3.2.4 Optical Reflectivity Sensor 34

CHAPTER 4 Experimental Methodology 36

4.1 Sample Preparation 36
4.1.1 FIB Samples 36
4.1.2 Thin Film Self Assembly 37
4.1.3 Sliders 38
4.2 Experimental Procedure 39
4.2.1 General Procedure 39
4.2.2 Special Procedures 42
4.3 Signal Processing 42
4.3.1 Friction Calculations 43
4.3.2 Capacitance Calculations 43
4.3.3 Acoustic Emission Calculations 44
4.3.4 Optical Reflectivity Calculations 44
CHAPTER 5 Results and Discussion 45
5.1 Patterning 45
5.1.1 FIB Patterning 45
5.1.2 Thin Film Self Assembly 47
5.2 Slider Heads 49
5.3 Testing Results 52
5.3.1 4” Disk Baseline Results 52
5.3.2 FIB Low Density Pattern Results 55
5.3.2.1 FIB Low Density Whole Disk Calculation Results 55
5.3.2.2 FIB Low Density 3 mm Region Calculation Results 59
5.3.3 FIB High Density Pattern Results 60
5.3.3.1 FIB High Density Whole Disk Calculation Results 60
5.3.3.2 FIB High Density 1 mm Region Calculation Results 62
5.3.4 Thin Film Self Assembly Experimental Results 65
5.3.4.1 Thin Film Self Assembly Full Load Results 65
5.3.4.2 Thin Film Self Assembly Half Load Results 66
5.4 General Discussion 68
CHAPTER 6 Conclusions 70
APPENDIX A: THEORETICAL AND EXPERIMENTAL STRAIN DERIVATION 72
APPENDIX B: STIFFNESS RATIO DERIVATION 74
APPENDIX D: MODEL WITH SYSTEM CAPACITANCE FOR HEAD TO DISK INTERFACE CAPACITANCE MEASUREMENT CIRCUIT 80
APPENDIX E: PHYSICAL MODEL FOR HEAD TO DISK INTERFACE CAPACITANCE MEASUREMENT CIRCUIT AND MAXIMIZING SENSITIVITY AROUND EXPECTED CAPACITANCE 82

APPENDIX F: SOFTWARE MASK FOR LOW DENSITY FIB SAMPLE 84

APPENDIX G: SOFTWARE MASK FOR HIGH DENSITY FIB SAMPLE 85

APPENDIX H: OPTICAL IMAGES OF SLIDER HEADS 86

LIST OF FIGURES

Figure 1: Block Copolymer Configuration. Each colored strand represents a polymer block composed of a linear sequence of same-type monomers, Where type A is red and type B is blue. The two blocks are bonded at one end thereby creating the diblock copolymer. 10

Figure 2: Diblock Copolymer Ordering. Regions are shaded according to monomer type, with blue for type A and red for type B monomers. Mass fractions of the blocks are not equal. 11

Figure 3: Schematic of NIL Process 14

Figure 4: Test Stand Overview Diagram 16

Figure 5: Test Stand Overview Photograph 17

Figure 6: Test Stand 4" Disk Configuration 18

Figure 7: Test Stand 1" Disk Configuration 19

Figure 8: High Speed Data Logger Virtual Instrument 21

Figure 9: High Speed Data Reader – B Virtual Instrument 22

Figure 10: Spin Speed Calibration for Motor and Hub 24

Figure 11: Four Active Arm (left) and Two Active Arm Wheatstone Bridge Circuits 25

Figure 12: CAD Model of the Dual Cantilever Beam 26

Figure 13: Calibration of Strain Gages – Horizontal Loading 27

Figure 14: Calibration of Strain Gages – Vertical Loading 28

Figure 15: Comparison of Disks - No Load Friction 29

Figure 16: Physical Capacitance Circuit (left) and Model with System Capacitance 30

Figure 17: Capacitance Sensor Calibration Curve 31

Figure 18: Capacitance Sensor Sample Data 32

Figure 19: Comparison of Disks - No Load Capacitance 33

Figure 20: Comparison of Disks – No Load Acoustic Emission 34

Figure 21: Optical Reflectivity Sensor Sample Signal 35

Figure 22: Diagram of Thin Film Self Assembly Process 41

Figure 23: AFM Image of Low Density FIB Sample 46

Figure 24: AFM Image of High Density FIB Sample 46
Figure 25: AFM Image of Thin Film Self Assembly After Step 5, Anneal 48
Figure 26: AFM Image of Thin Film Self Assembly After Step 8, Sputter Ti 48
Figure 27: AFM Image of Thin Film Self Assembly, Zoomed Out 49
Figure 28: Slider With Particulate Contamination 50
Figure 29: Slider #5, No Contamination After Use in Four Consecutive Tests 50
Figure 30: Example of Wear Track Formation and Si Wafer Configuration 51
Figure 31: 4” Disk Baseline Data – Friction 52
Figure 32: 4” Disk Baseline Data – Capacitance 53
Figure 33: 4” Disk Baseline Data – Acoustic Emission 54
Figure 34: FIB Low Density Whole Disk Calculation Results – Friction 56
Figure 35: FIB Low Density Whole Disk Calculation Results – Capacitance 56
Figure 36: FIB Low Density Whole Disk Calculation Results – Acoustic Emission 57
Figure 37: FIB Low Density 3 mm Region Calculation Results – Friction 58
Figure 38: FIB Low Density 3 mm Region Calculation Results – Capacitance 58
Figure 39: FIB Low Density 3 mm Region Calculation Results – Acoustic Emission 59
Figure 40: FIB High Density Whole Disk Calculation Results – Friction 60
Figure 41: FIB High Density Whole Disk Calculation Results – Capacitance 61
Figure 42: FIB High Density Whole Disk Calculation Results – Acoustic Emission 61
Figure 43: FIB High Density 1 mm Region Calculation Results – Friction 63
Figure 44: FIB High Density 1 mm Region Calculation Results – Capacitance 64
Figure 45: FIB High Density 1 mm Region Calculation Results – Acoustic Emission 64
Figure 46: Thin Film Self Assembly Full Load Results – Friction 65
Figure 47: Thin Film Self Assembly Full Load Results – Acoustic Emission 66
Figure 48: Thin Film Self Assembly Half Load Results – Friction 66
Figure 49: Thin Film Self Assembly Half Load Results – Acoustic Emission 67
Figure 50: Schematic of Cantilever Beam #1 74

Figure 51: Schematic of Cantilever Beam #2 76
Figure 52: Acoustic Emission Sensor Calibration Certificate 79
Figure 53: Software Mask for Low Density FIB Sample 84
Figure 54: Software Mask for High Density FIB Sample 85
Figure 55: Air Bearing Surface, Style #1 86
Figure 56: Air Bearing Surface, Style #2 86
Figure 57: Air Bearing Surface, Style #3 (After Use) 87
Figure 58: Front View of Slider Head 87
Figure 59: Back View of Slider Head 87

LIST OF TABLES

Table 1: Quantization Error and Corresponding Dimensional Value Error 22

Table 2: Strain Comparison of the Dual Cantilever Beam 26

Table 3: Stiffness Ratio Comparison of the Dual Cantilever Beam 26

Table 4: Copolymer Properties 38

Table 5: Slider Performance Characteristics 38

Table 6: High Speed Data Logger.vi Settings 39

Table 7: Conserved Surface Area Ratios for Experimental Samples 69

SUMMARY

The goal of this thesis is to experimentally characterize the flyability of current generation read/write heads over media patterned to densities above the superparamagnetic limit.

The superparamagnetic limit is the physical limit to magnetic storage density. In magnetic storage, superparamagnetism is the uncontrollable switching of stored bits during the lifespan of a hard disk. Theoretical analysis has predicted that densities of ~50 Gbit/in^2 are not possible using traditional continuous media. One strategy to achieve high storage density, above the superparamagnetic limit, is patterned media. With patterned media the physical separation of magnetic domains increases their stability.

One of the major challenges of development of patterned media is achieving acceptable flyability of the read/write head. In that vein, a test stand is built to measure head liftoff speed, head to disk intermittent contact and head fly height. Tangential friction, an indicator of head liftoff is measured by a Wheatstone bridge strain circuit attached to a cantilever beam. Intermittent contact is quantified by the amount of noise emanating from the interface, which is measured by a high frequency acoustic emission sensor. Head fly height is measured indirectly with a capacitance circuit built around the head to disk interface.

Experimental samples of current generation read/write heads and media are obtained from industry. Current generation media is patterned using focused ion beam milling to a density of 10 Gbit/in^2. Other, extremely dense samples, above 700 Gbit/in^2, are created via thin film self assembly on silicon substrate.

Conclusions on slider head flyability over patterned media are based on

comparison with flyability over non-patterned media. It is demonstrated that loss of hydrodynamic lubrication is small for small pattern regions with high conserved surface area ratio. Conserved surface area ratio is defined as total surface area minus etched surface area all divided by the total surface area of the storage media. For wafer scale patterned media with low conserved surface area ratio, head liftoff cannot be achieved at designed normal load. However, a 50% reduction of load allows slider head liftoff.

CHAPTER 1

INTRODUCTION

In this work the flyability of current slider heads over patterned media is characterized experimentally. A test rig with normal load, friction, acoustic emission and capacitance sensors was built. Patterned media was created by two methods each with different benefits and characteristics. Experiments were carried out using both types of patterned media as well as control specimens of standard longitudinal media hard disk.

1.1 Motivation

Since the first hard disk device, the IBM RAMAC, the density of magnetic storage has grown 25% or more per year. Recently, that growth rate has increased to 100% per year.[1] At this rate, the physical limit of areal density, known as the superparamagnetic limit, will be reached in the near future. Superparamagnetism becomes important when the stored energy per magnetic grain starts competing with thermal energy.[2] The exact density at which it occurs is a function of storage media material properties and microstructure, and has been increased over time with improvements in writing technology and media material properties. An upper limit to achievable densities has been estimated to be about 36 Gbit/in^2 in longitudinal media.[3] In this condition, magnetic domains representing bits of data can spontaneously change polarity causing loss of stored information. The loss of data is considered a failure if it occurs in the five year design life of a hard drive.

1.2 Industrial Application

To motivate a solution to this problem the National Storage Industry Consortium (NSIC) announced, in 2000, the goal to demonstrate 1 Tb/in^2 storage density within five

years. Reaching this goal will clearly require technology to delay the onset of superparamagnetism and open the door to extremely high storage densities.

In the last four years several technologies have been improved such that the goal of demonstrating data storage at that density is nearly within reach, in the laboratory at least. February 2004 work at IBM Almaden Research Laboratory demonstrated 400 Gbit/in^2 areal density using thermomagnetic recording.[4] Thermomagnetic or thermally assisted recording uses localized heating to lower the coercivity of a highly thermally stable magnetic material that would otherwise not be writable with current read/write technology.

A different architecture, called perpendicular recording, orients the magnetic domains normal to the media surface to achieve a higher domain volume and therefore increase the thermal stability. Finally, patterned media separates the bit domains so that exchange coupling can be limited and improve thermal stability. This is different from the longitudinal, continuous storage media used in current production hard disk drives. These technologies are not mutually exclusive, patterned media can also be used to compliment thermomagnetic storage or perpendicular recording.

Manufacturing technologies, including nano-imprint lithography (NIL), step and flash imprint lithography (SFIL) and nanometer scale self assembled thin films have potential for low cost, full scale industrial applications. These technologies can facilitate the manufacture of patterned surface media.

1.3 Objective

With all the promise that patterned media holds, it is not known if current production slider heads can generate sufficient pressure fields to limit head to disk

contact, or achieve full hydrodynamic lubrication (known as 'flying' over media). Therefore, the focus of this work is to characterize the flyability of current production slider heads over patterned media through experiments.

In support of this, patterned disks were created at densities around the superparamagnetic limit using two methods. First, focused ion beam (FIB) etching is used for its simplicity. However, the Hitachi FB-2000A has limited pattern density and limited surface area coverage. Second, nanometer scale self assembled thin film lithography with wet chemical etching is used for superior pattern density and high surface area coverage. The patterned disks have been tested with several commercial read/write heads to determine lift off speed, flying friction and fly height. Experiments were carried out on a test rig with 2 sets of strain gauges, an acoustic emission sensor, a capacitance measurement circuit and an optical reflectivity sensor. These sensors are used to characterize normal load, tangential load, interface contact, fly height, and rotation rate, respectively.

CHAPTER 2

LITERATURE REVIEW

The data storage industry has been relentless in pushing the limits of technology to drive areal storage densities higher. An overview of efforts related to this work is presented here.

2.1 Data Degradation

Of utmost importance in data storage is the quality and reliability of stored information. There are two mechanisms primarily responsible for the degradation of magnetically recorded information, superparamagnetism and exchange coupling. Both effects lead to density limits and both are the focus of current work in increasing areal density in thin film magnetic storage.

2.1.1 Superparamagnetism

The superparamagnetic effect is a significant barrier to increasing magnetic data storage density in thin film magnetic data storage. Qualitatively, superparamagnetism describes an inability of magnetic bits to reliably maintain a charge for the five year design life of a hard disk drive. Quantitatively, superparamagnetism is characterized by the 'stability ratio,' defined in Equation 1[6]:

$$\frac{K_u V}{kT} \tag{1}$$

Where:

K_u is the uniaxial anisotropy energy density;

V is the switching volume;

k is Boltzman's constant;

T is temperature.

The top half of the equation is characteristic of the stored energy of the bit domain while the bottom half is the thermal energy of the domain. Clearly it is desirable to have this ratio as high as possible so that thermal noise is negligible compared to data energy. If the stability ratio is above 45-60[5,6] superparamagnetism can be considered negligible for the five year life of the hard disk.

2.1.2 Exchange Coupling

Exchange coupling is an inter-granular interaction that can cause data loss in magnetically stored data. Qualitatively, exchange coupling describes the formation of magnetic moments between adjacent bit domains. This unwanted coupling between bits can cause unwanted magnetic noise and unpredictable magnetic moment switching, i.e. data loss. Fang[7] compares media noise power for data storage with and without exchange coupling. He clearly shows that media without exchange coupling has significantly less noise. Also, according to Ouchi and Honda[8], shrinking data domain size will require reduction in magnetic exchange coupling between adjacent grains.

2.2 Data Storage above the Superparamagnetic Limit

There are three technologies under strong investigation for data storage above the superparamagnetic limit. Thermomagnetic recording and perpendicular recording are competing technologies that both have the potential to circumvent the superparamagnetic limit. However it is possible to improve the performance of both by incorporating magnetic isolation of stored data bits. Patterned media is this third technology. Patterning the storage media is a method of limiting exchange coupling to improve thermal stability.

2.2.1 Thermomagnetic Recording

With thermomagnetic recording, data storage architecture is oriented the same as traditional longitudinal media. Since this same architecture is used the domain size must be proportionally smaller to achieve storage densities above the superparamagnetic limit. Yet, superparamagnetism becomes a concern at domain sizes significantly smaller than those in use today. To circumvent superparamagnetism a media material with high remnant magnetic moment must be used. Unfortunately, these materials also have high coercivity, the minimum magnetic field that must be applied to manipulate a data bit. It is known that coercivity lowers with increasing temperature. Thermomagnetic storage takes advantage of this effect. Before writing a bit, a laser heats the region where the bit is to be written. This is done immediately in front of the slider because cooling happens rapidly at such small length scales. After heated writing, data can be read without additional heating.

Despite its technical difficulties, work published in 2004 demonstrated 400 Gbit/in^2 density using thermomagnetic recording.[4] It continues to be a primary alternative to longitudinal media along with perpendicular recording.

2.2.2 Perpendicular Recording

Perpendicular recording has been studied as an alternative to longitudinal media since 1980.[9] Iwasaki showed that the normal orientation of the magnetic moments lowers inter-granular exchange coupling and makes recorded data more stable. This will allow bit domains to be closer together without the degradation effects of exchange coupling found in longitudinal media. He states, “In practice, it is expected that the length of the magnetization transition region [between bit domains] can be decreased to the grain [size] or crystal line structure of the medium.”

Recently, Wang et. al.[10] studied the effects of exchange coupling in perpendicular media with conditions based on a proposed 100 Gbit/in^2 storage density. This corresponds to a simulation testing density of 1.134 million flux changes per inch at a recording width of 112nm. They conclude that media noise increases with exchange coupling especially at high linear storage density. The best way to limit exchange coupling without lowering storage density is to physically separate the magnetic domains into regular patterns. This is achieved by patterning media.

2.2.3 Patterned Media

The creation of patterned media requires physical etching. In addition, some techniques require masking for selective material removal, and some do not. For the processes that require a mask, there are two schools of thought on how to make them. Masks can be manually created, or they can be self assembled. Promising mechanically created masking techniques include step and flash imprint lithography (SFIL) and nanoimprint lithography (NIL). Self assembled masks can be made from thin films of monodisperse block copolymers that form regular, thermodynamically stable patterns when annealed above glass transition temperature.

2.2.3.1 Non-Masked Patterning

There are two methods for creating patterned media without at mask. Electron beam lithography and focused ion beam lithography both offer a directed beam of matter to etch via ablation.

2.2.3.1.1 Electron Beam Lithography

Electron beam lithography (EBL) is an ideal etching method with respect to its resolution, accuracy and precision. Depth can be precisely controlled by the delivered

energy dose and an inherent large depth of focus from continuous focusing. Resolution of 10nm is common in solids. Selective etching is achieved by computer controlled magnetic fields which direct the beam according to a software mask.[11]

However, the process must be done in vacuum to avoid beam scattering from interaction with air particles. EBL is also notoriously slow for wafer scale applications and has high overall system cost. Typically, EBL is used to manufacture photolithographic and other masks, specialty ICs and in research applications.[11]

2.2.3.1.2 Focused Ion Beam Lithography

Focused ion beam lithography (FIB) is similar to and shares many of the benefits and drawbacks of EBL. It has been studied extensively[12,13,14,15,16,17] for use as a patterning technique.

FIB must occur in vacuum, like EBL, and has good depth control in the same way EBL does. Resolution in the best FIB systems is slightly better, at 8 nm. FIB is also very slow when etching wafer scale applications.[11]

However, FIB has the added benefit that it deposits the etchant material, most commonly gallium, in the work piece. When used to etch patterns in longitudinal media hard disks, it has the effect of achieving magnetic domain isolation without etching completely through the magnetic medium. Rettner[17] demonstrated stable, single domain islands with a 100nm period. These were formed from 6 nm deep, 25 nm wide trenches surrounding 75 x 75 nm islands. Indeed, the six nanometer trench depth is only slightly deeper than the 5 nm carbon overcoat on the disk, yet gallium was found throughout the 20nm depth of the media material. This suggests that a primary cause of magnetic isolation is the gallium implantation which acts in combination with material removal.

Because of the speed of non-masking techniques other more complicated but less expensive methods are also used to create patterned media.

2.2.3.2 Masked Patterning

Masking techniques have different benefits from non-masking techniques. More steps are required to get the same results; however, the etching takes less time and is typically less expensive. The most promising methods include self assembled masking, nanoimprint lithography, and step and flash imprint lithography.

2.2.3.2.1 Self Assembled Masking

A superior self assembled masking technique has been in development for several years, and was recently optimized by Guarini, Black and Yeung.[18] The process was described succinctly by Kellogg et. al.[22] saying, " … diblock copolymers consist of polymer chains … covalently connected at one end. Because the blocks of the copolymer are usually immiscible, phase separation occurs. But unlike conventional mixtures, where macroscopic domains may grow, the connectivity of the diblock copolymer restricts phase separation to chain dimensions typically tens of nanometers."[22] Figure 1 pictorially shows a common diblock copolymer architecture. To date, thin film masking has focused on the diblock AB architecture, where A is polystyrene (PS) and B is poly(methyl methacrylate) (PMMA).

Diblock copolymer microphase separation had been studied extensively. Phase diagrams have been developed theoretically and verified experimentally. A comparison of theoretical and experimental phase diagrams is thoroughly discussed by Bates.[19]

In 1994, Walton et. al.[20] presented a model for lamellar morphologies based on the 'free energy' of the system. Specifically, it modeled interfacial energy based on the

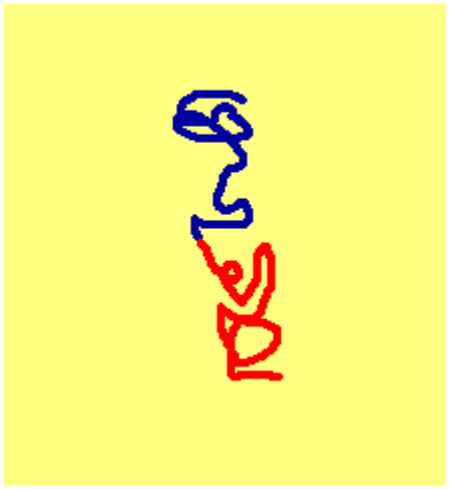

Figure 1: Block Copolymer Configuration. Each colored strand represents a polymer block composed of a linear sequence of same-type monomers, Where type A is red and type B is blue. The two blocks are bonded at one end thereby creating the diblock copolymer.

segregation of the two blocks with an entropy correction for deforming the chains of polymers. The model was validated experimentally by predicting the lamellar period of PS and PMMA between two hard, parallel surfaces.

Similar studies have been carried out for other polymer pairs. Specifically, PS and polyvinylpyridine (PVP) was studied by Yokohama et. al. in 2000.[21]

In 1996, Kellog et. al.[22] began to understand how to control the phase separation phenomena. They coated the walls that confine the diblock copolymer and observed that varying the surface properties of the walls affected the morphology. Wall properties were modified by spin coating random copolymers onto them before introduction of the diblock copolymer.

Mansky et. al.[23,24], in 1997, described how surface properties could be modified by end-grafting random copolymer chains to the surface. This process creates a brush whose properties dominate the interaction with the diblock copolymer in place of the

substrate surface. The random copolymer chains are composed of the same components of the diblock copolymer, PS and PMMA. The effects of varying the monomer fraction of PS, denoted *f*, are explored. Mansky[23] showed that by changing *f*, an affinity to either polymer, both polymers, and any combination thereof can be achieved. Subsequently[24], the technique used to produce the results was detailed and operational parameters were investigated.

In 2001, a team from IBM combined the techniques to produce self assembled masks[25], and then used them to etch patterns into silicon wafers. The masks were created by neutralizing the surface properties with the method described by Mansky[24], then spin coating a layer of the PS-PMMA copolymer. The film was annealed to "… promote self assembly into nanometer-scale domains …"

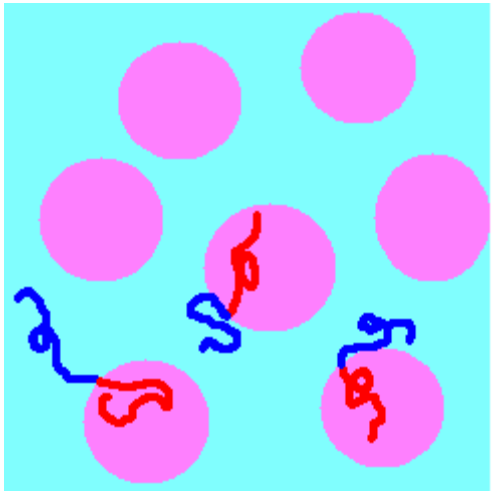

Figure 2: Diblock Copolymer Ordering. Regions are shaded according to monomer type, with blue for type A and red for type B monomers. Mass fractions of the blocks are not equal.

A pictorial description is shown in Figure 2. In the described procedure, f_{PS} = 0.70, specifically matching the phase separation shown in Figure 2b.

Next, the film was exposed to 1800 mJ of UV light, which cross-linked the PS and degraded the PMMA. 100% Acetic acid was used to develop the film for 3 minutes at room temperature. It selectively removed the PMMA, leaving a porous PS film. This porous film was effectively used to mask areas of silicon to reactive ion etching (RIE), thereby creating an eight inch diameter pattern of nanometer scale holes in the silicon wafer. Subsequently, metal was sputtered onto the wafer. The metal filled the holes left by the RIE and coated the PS mask. Finally, the mask was removed with a lift off technique revealing an array of gold dots with a 25 nm average diameter on an average 52 nm period.

This process is desirable for two reasons. First, the technique is relatively simple. It can be done in a standard chemical wet lab, with the addition of a spin coater and hot plate. Viewing the mask does require more expensive equipment, namely a scanning electron microscope (SEM), atomic force microscope (AFM) or similarly capable imaging device. Second, it is desirable because of its low cost. Materials are relatively inexpensive and the process does not require expensive processing equipment. This combination makes thin film self assembly highly accessible.

2.2.3.2.2 Other Masking Techniques

NIL is a combination of masking and non-masking techniques that is capable of high resolution patterning at the nanometer scale and holds promise for scalable, high throughput, low cost per-unit production.

NIL starts with a spin coat of resist onto the substrate. Next, the work piece is placed in a press with a mold. In the press, heat and pressure help the resist form to the mold. When the work piece is removed and cooled the negative of the mold pattern has

been formed in the resist. It can be transferred to the substrate using reactive ion etching. Figure 3 shows this graphically.

The NIL process itself can be completed in less than an hour; however, the mask used for shaping the resist must be made by another technique, typically EBL. Since the cost of EBL is high for a wafer size mold, the benefit of NIL is volume production that offsets the initial cost of a mold.

Chou demonstrates an application of NIL to create patterned magnetic structures.[26] After pattern transfer to the substrate he deposits a metal into the holes by sputtering. The result is a rectangular pattern of dots of 10 nm diameter on a 40 nm period. Step and flash imprint lithography offers many of the same benefits as NIL, with the added benefit of higher aspect ratio capabilities. This comes from the fact that the masking material, usually PS, is pressed with the mold while in a liquid state. The liquid fills cavities in the mold more easily than the solid film in NIL. While the mold is held under pressure, the masking material is exposed to UV light, cross linking and solidifying the polymer mask. Because of this requirement the mold must be transparent. It is typically made of quartz.

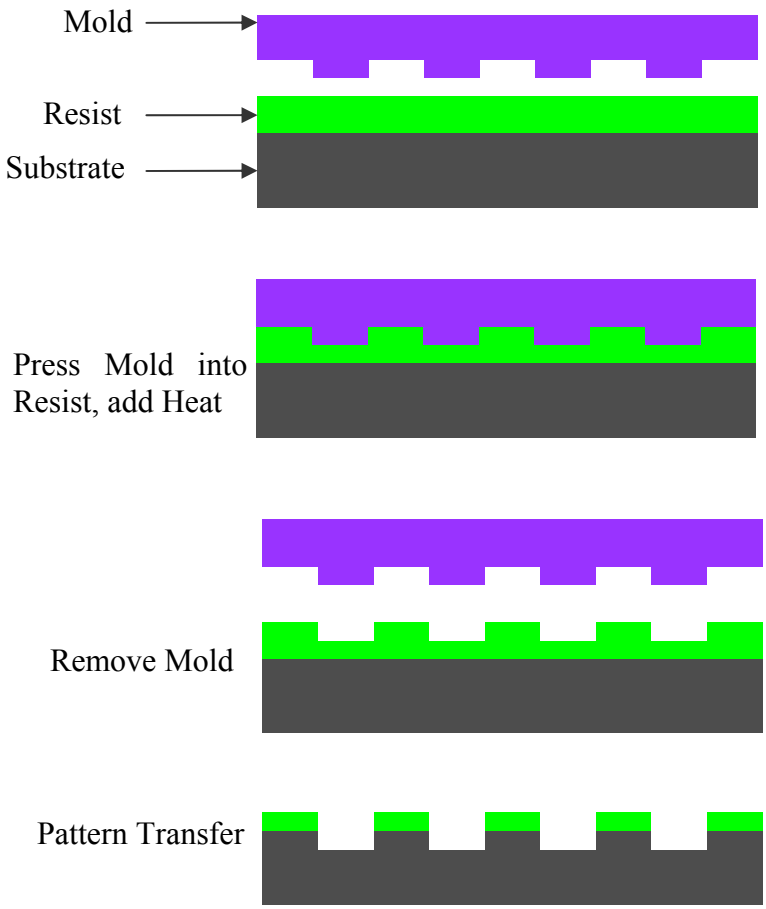

Figure 3: Schematic of NIL Process

CHAPTER 3

APPARATUS

In support of the primary thrust of this work, a test stand was designed and built to test the flyability of current generation sliders over patterned media. When a slider is flying, or, has achieved full hydrodynamic lubrication (HDL), several characteristics change. First, drag friction in full HDL is significantly lower than drag friction when the slider is in contact with the spinning disk. Second, the slider emits noise, or acoustic emission, as the disk is rotated underneath. When the slider is flying the noise that is emitted from the slider head to disk interface is significantly lower. Finally, the electrical connection between the slider head and the disk adds a capacitive impedance to a resistive one, where capacitance is a function of flying height.

The test stand was designed to measure each of these changes; friction, acoustic emission, and head to disk interface capacitance. In doing so it has three concurrent measurements to determine if the slider head is flying over the disk, in contact with the disk, or some combination of the two. The overall diagram layout of the test stand can be seen in Figure 4 and labeled pictures of the test stand can be seen in Figure 5, Figure 6 and Figure 7.

3.1 Primary Systems

The test stand can be segmented into several primary systems that set the testing environment. First is the data acquisition system, consisting of those components whose function is to record data. Second is the drive system that provides the steady rotational speed during testing. Third is the positioning system that locates and loads the slider relative to the spinning disk.

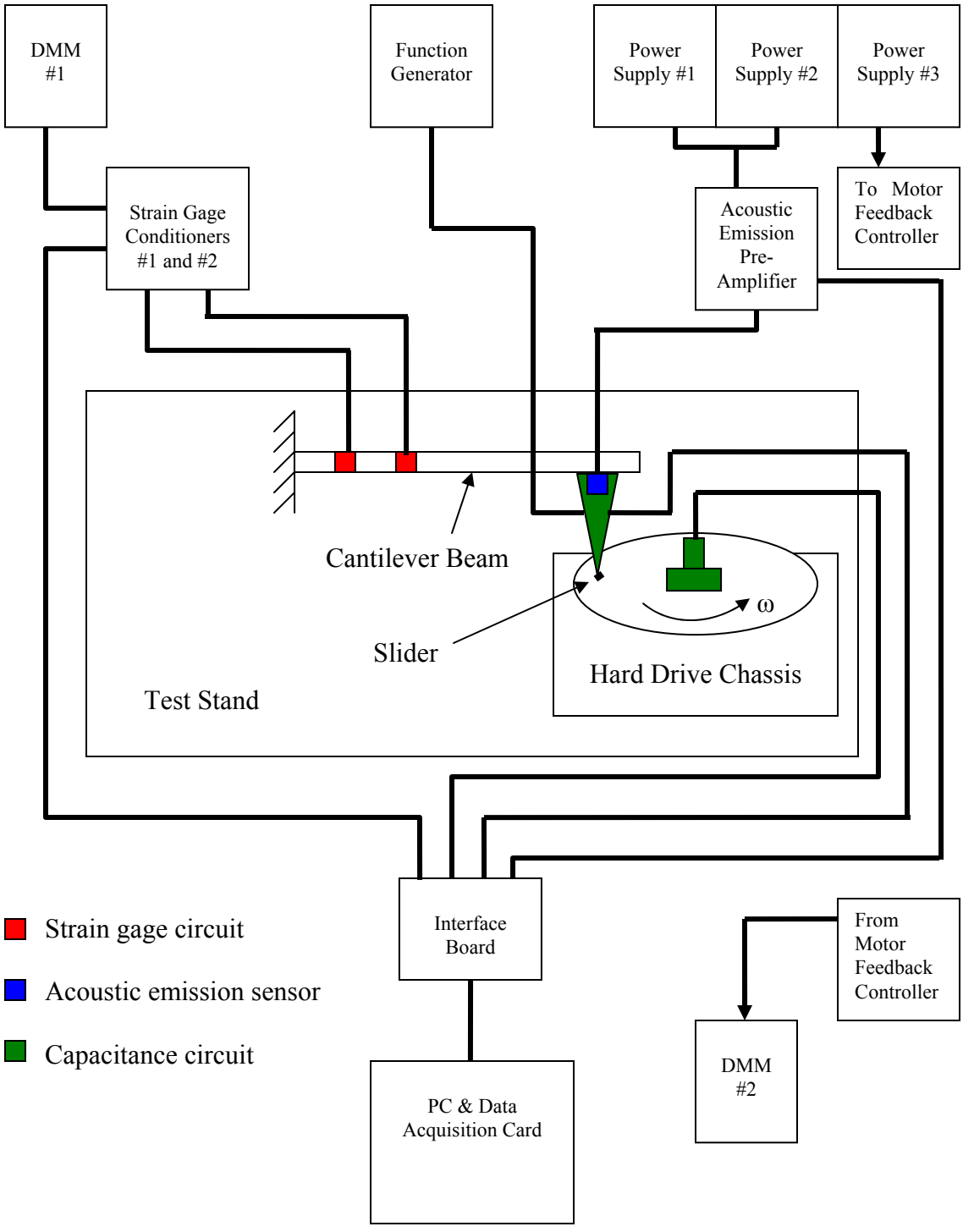

Figure 4: Test Stand Overview Diagram

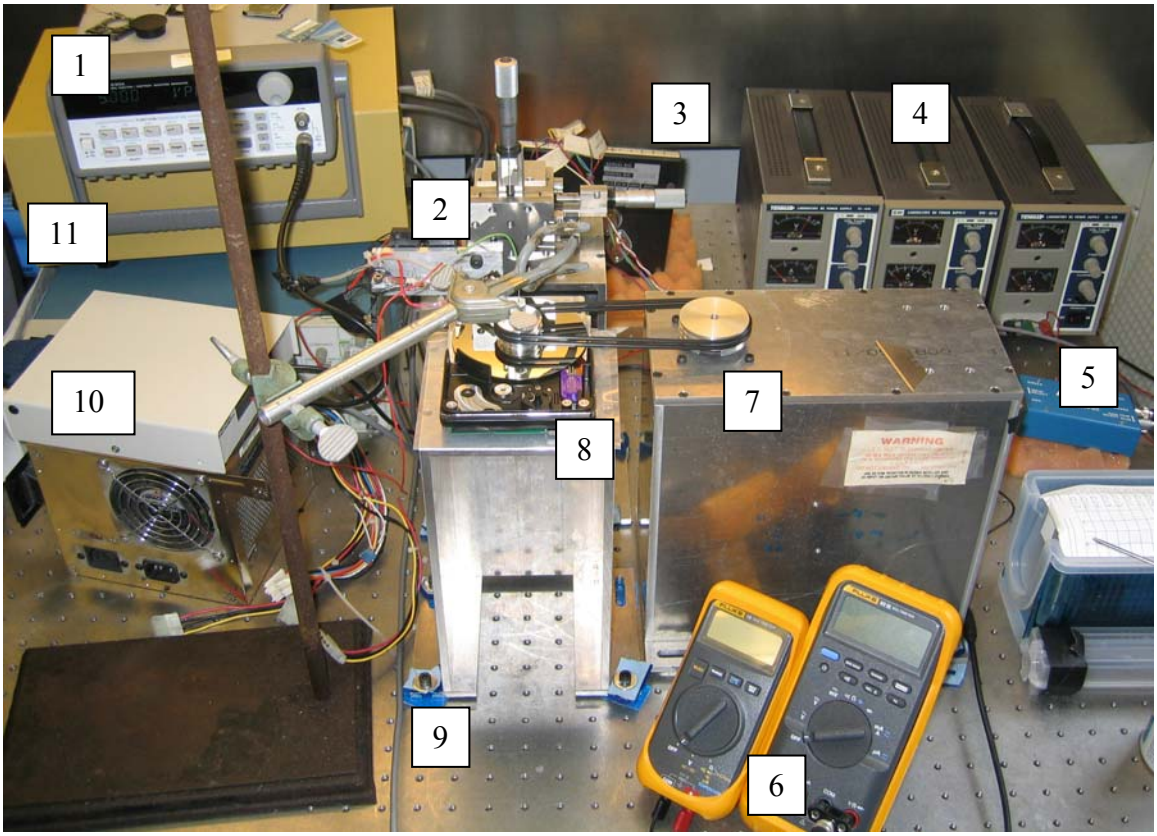

Item Number	Component Name	Function
1	Function generator	Create sine wave for capacitance circuit
2	Cantilever and sensors	See
3	Motor feedback controller	Maintain constant motor speed
4	Power supplies	Set constant voltage for AE Pre-amp(1,2) and motor (3)
5	AE pre-amplifier	Amplify AE signal
6	Digital multi-meters	Display normal load (L) and motor feedback voltage (R)
7	Motor and drive pulley	Spin test specimen
8	Hard drive chassis	Provide low run-out bearing
9	Vibration absorbers	Reduce vibration noise
10	Interface board	Connect sensors to data acquisition board
11	Strain gage conditioner	Amplify friction signal

Figure 5: Test Stand Overview Photograph

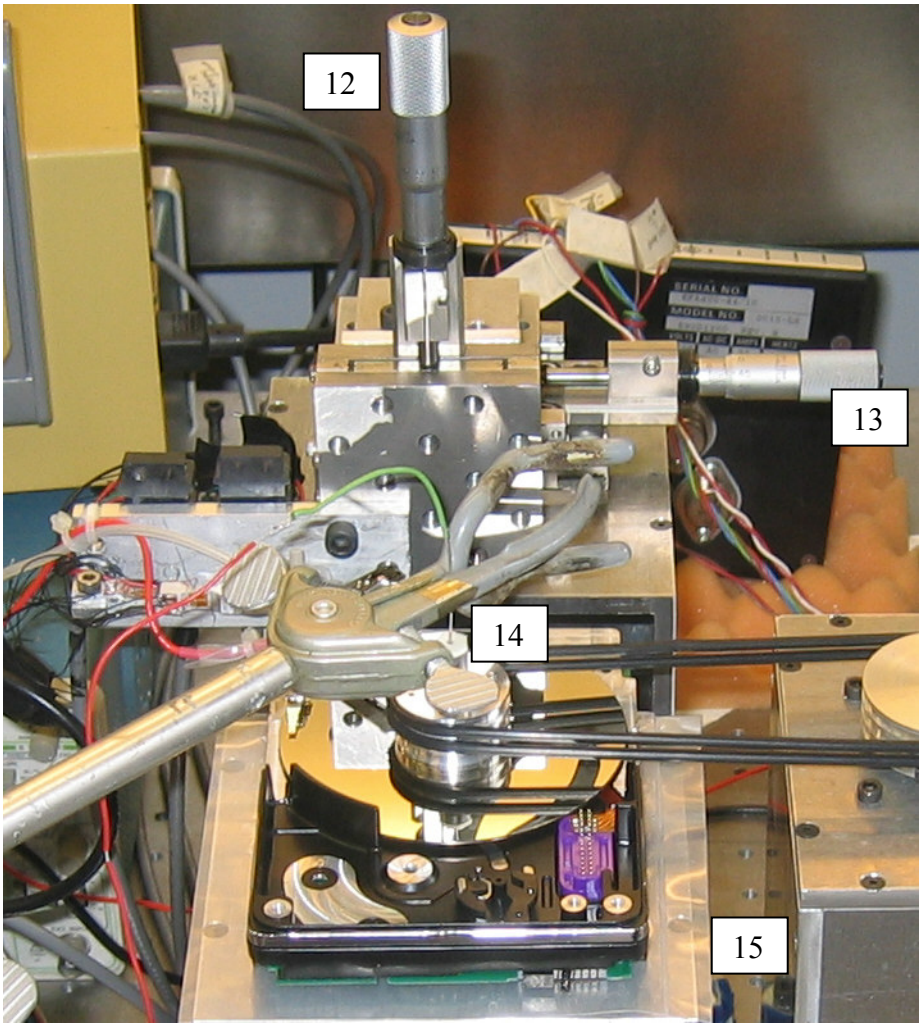

12	Vertical micrometer stage	Provide precise vertical loading and positioning
13	Radial micrometer stage	Provide precise radial positioning
14	Mercury cup	Provide electrical connection for a rotational to stationary interface
15	Plastic sheeting	Provide secondary electrical isolation between chassis and base

Figure 6: Test Stand 4” Disk Configuration

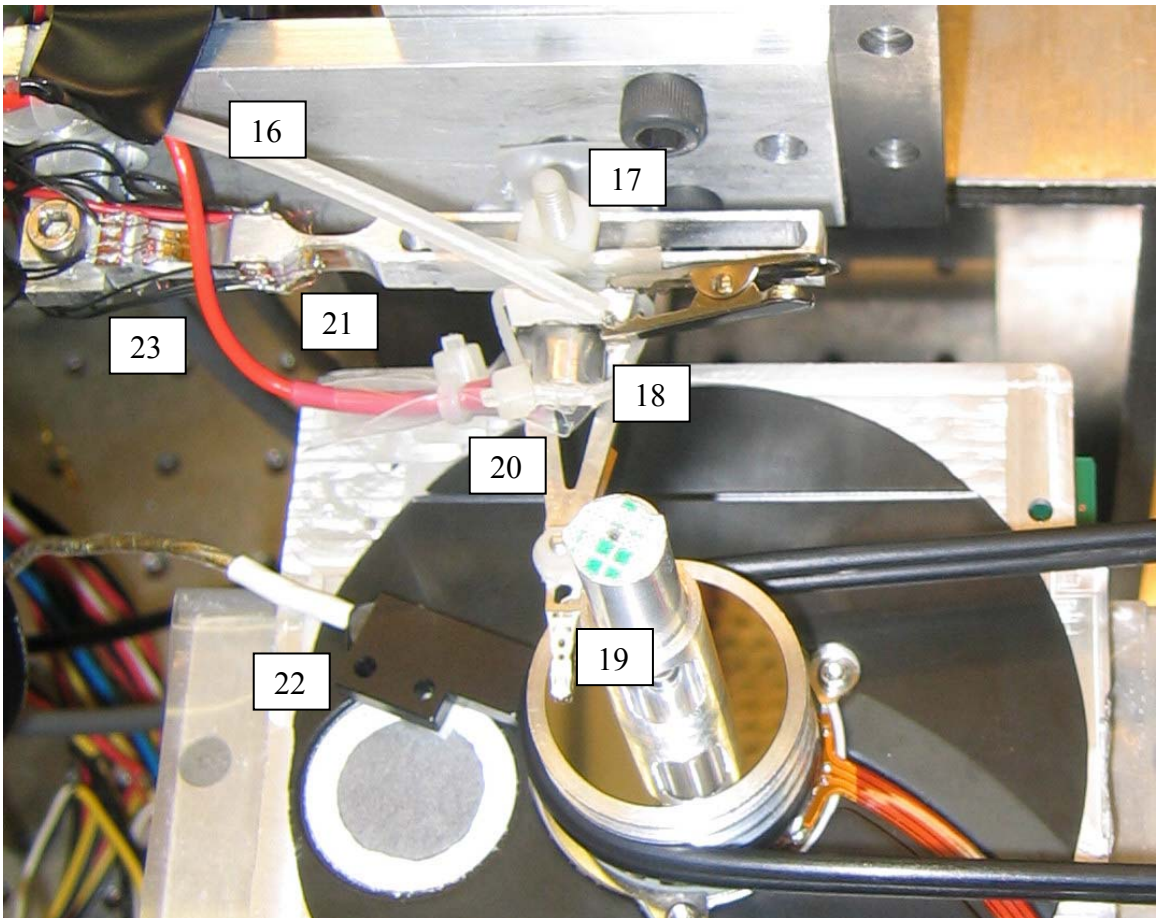

16	Capacitance input signal wire	Carry capacitance signal
17	Plastic sheet and fasteners	Provide electrical isolation
18	AE sensor	Tranduce measurable noise signal
19	Slider head (underside) and suspension arm	Fly over various disks
20	Gimble	Supporting arm for slider
21	Friction strain circuit	Transduce measureable friction signal
22	Optical reflectivity sensor	Provide measurable marker hub and disk rotation
23	Normal load strain circuit	Transduce measureable load signal

Figure 7: Test Stand 1” Disk Configuration

3.1.1 Data Acquisition System

The data acquisition system consists of the interfaced board, data acquisition board, data acquisition software and virtual instruments. The interface board serves to provide a connection from the sensor wires to the data acquisition board. It is a National Instruments model SCB-68, shielded connection board. The data acquisition board is a National Instruments model PCI-6115E. It has four channels of double ended analog inputs, each with its own 12-bit digital to analog converter (DAC). The voltage range for each channel can be set independently such that the resolution can be maximized for the signal measured on each channel. For example, the optical reflectivity signal varied from -4.88 V to +2 V. To sample this signal the data acquisition voltage range was set to +/- 5 V. The quantization error for this signal is calculated in Equation 2. Quantization error for measurements taken from a digital multi-meter is simply half of the least significant digit shown. Table 1 is a listing of quantization error and corresponding dimensional value error for each measured signal.

$$\frac{1}{2} \times \frac{10V}{2^{12} bits} = 1.2mV \tag{2}$$

Each DAC can sample up to 10 MHz, and all channels sample simultaneously. The board has 8 million samples of onboard storage for each channel.

Data acquisition software was LabVIEW version 6.1. Within LabVIEW, two virtual instruments (VI) were used to sample data. Both were standard VIs from National Instruments that were modified for these experiments. First, High Speed Data Logger.vi , seen in Figure 8, was designed to efficiently record data at high speeds. It records data in

a LabVIEW binary form. Next, High Speed Data Reader.vi was modified to High Speed Data Reader – B.vi, seen in Figure 9. This virtual instrument allows scrolling through the data visually to see what it looks like. The modification added data conversion from LabVIEW binary to Matlab binary, or .mat, files which are subsequently used for data manipulation.

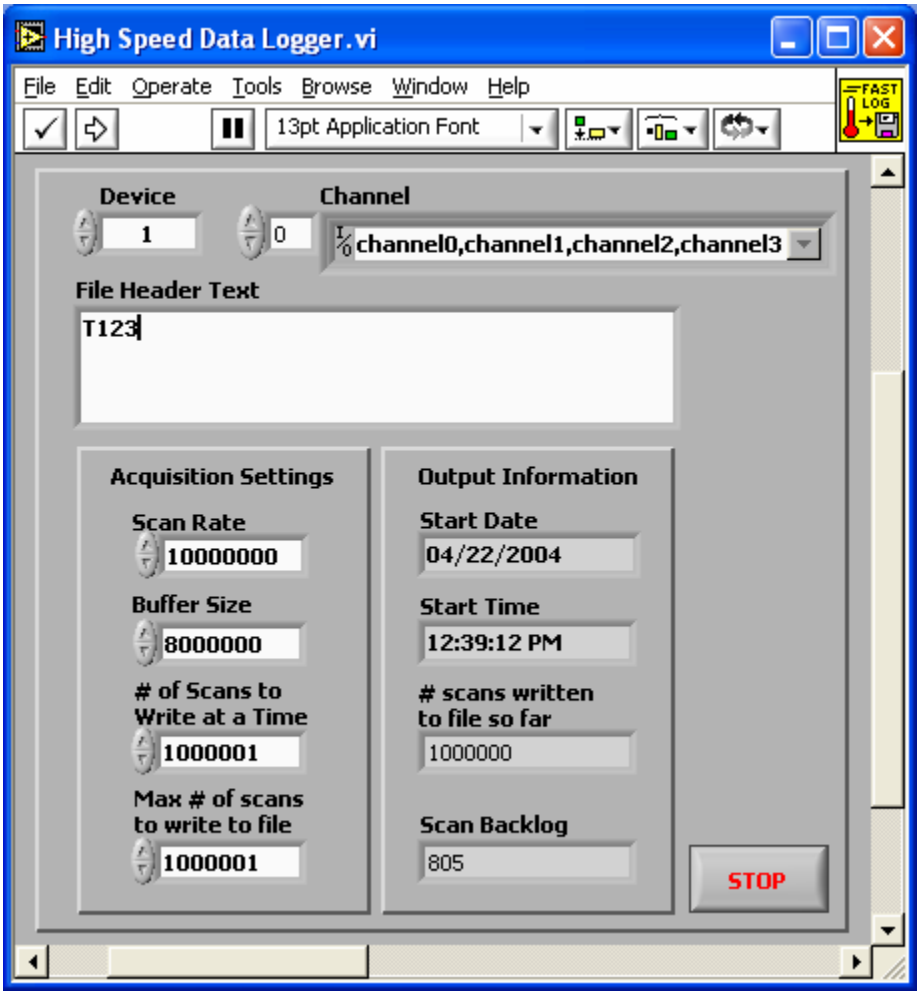

Figure 8: High Speed Data Logger Virtual Instrument

Table 1: Quantization Error and Corresponding Dimensional Value Error

Signal	Voltage range (V)	Quantization Error (mV)	Dimensional Value
Friction	+/- 2	0.49	12 mg
Load	N/A	0.5	15 mg
Acoustic Emission	+/- 2	0.49	0.35 mV
Capacitance Input	+/- 3	0.73	N/A
Capacitance Output	+/- 3	0.73	1.5 pF
Optical Reflectivity	+/- 5	1.2	Negligible RPM
Speed	N/A	50-0.5	0.01-0.0001 m/s

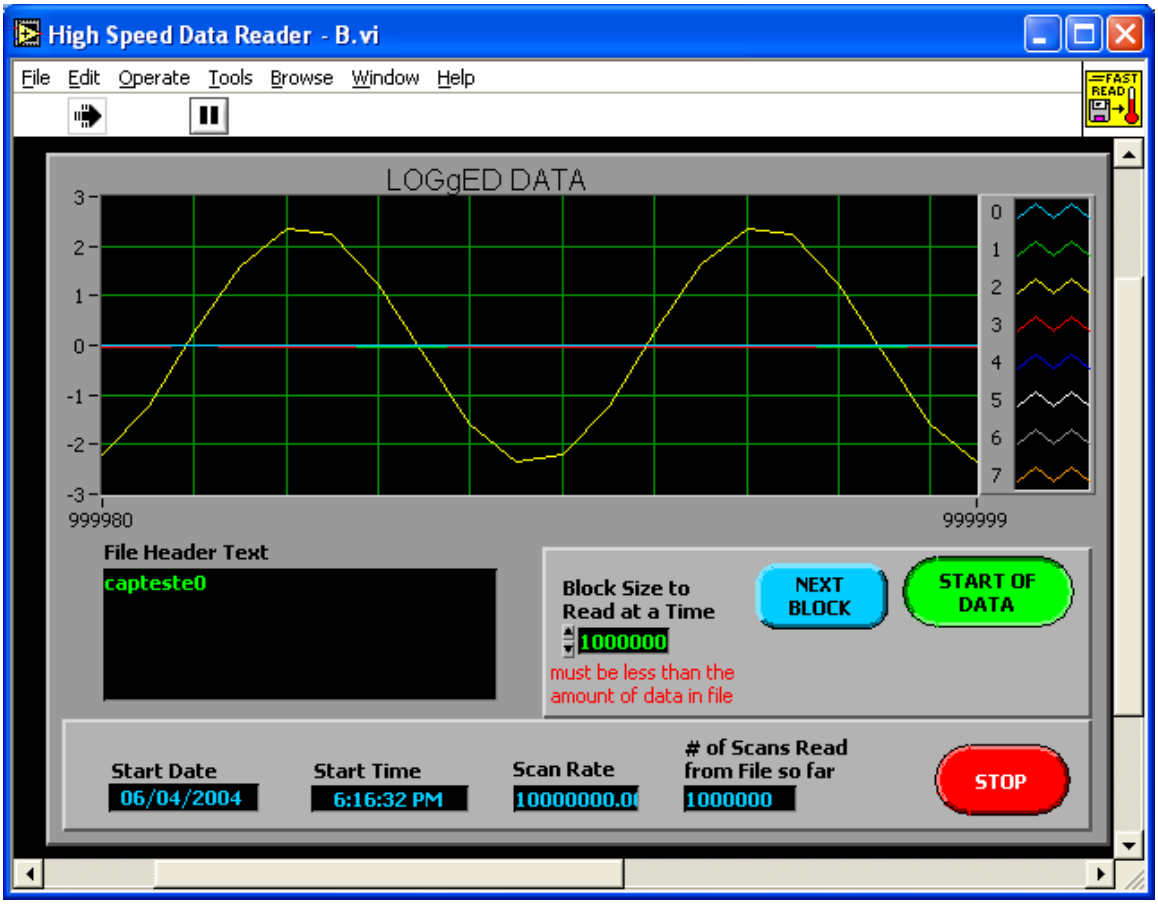

Figure 9: High Speed Data Reader – B Virtual Instrument

3.1.2 Drive System

The drive system consists of a power supply, feedback controller, multi-meter, DC motor, pulleys, belts and the hard drive chassis.

The power supply is a Tenma model 72-420 0-20 V DC power supply. It provides a reference voltage to the motor controller, an Aerotech Servo Controller model 3010-LS, so that motor speed varies directly with reference voltage. The controller serves to maintain a steady speed despite varying torque loads; so long as the torque loads are kept within the rated load range of the motor. The motor, Aerotech model 1030-01-1000-03, is connected to the hard drive chassis hub through the pulley system seen in Figure 5, label 7. The pulleys are sized such that there is a 60% increase in the angular speed from the motor to the hub. The effective angular speeds are measured with the feedback voltage of the motor controller and can be seen in the calibration plot, Figure 10. Feedback from the motor controller is measured on a Fluke model 83 III digital multi-meter.

The hub of a hard disk drive was used as the base component of the test stand for two reasons. First, the bearing vertical runout was low, at approximately +/- 0.001", or +/- 25 μm, as measured with a dial indicator. Second, the bearing elements were thermoplastic resin. These provide electrical isolation from the inner race to the outer race of the bearing. This isolation is important to keep the capacitance circuit a closed loop and limit measurement noise.

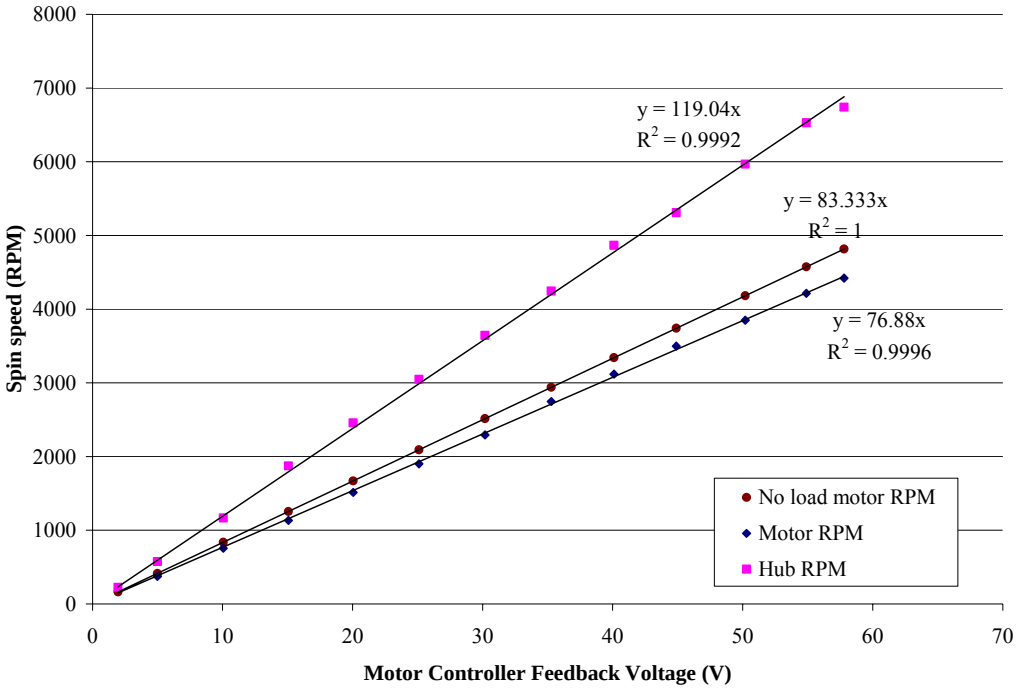

Figure 10: Spin Speed Calibration for Motor and Hub

3.1.3 Positioning System

The last primary system is the positioning system consisting of two Newport Corp. micrometer stages and a Fluke model 16 digital multi-meter. Position uncertainty is +/- 0.5 μm based on a Vernier scale built into the stages. This dimension is rarely used. Load height is not a slider design parameter; rather, load force is the governing parameter. Similarly, radial position is varied to maximize linear speed for each specimen.

3.2 Sensors

There are four types of sensors used in the test stand. Strain gages are used to measure force in both the horizontal plane (friction) and vertical plane (load). A capacitance circuit is constructed around the head to disk interface to measure spacing

between the slider and disk which is assumed to have a capacitive type impedance. An optical reflectivity sensor is used to measure revolutions of a marker attached to the hub. Lastly, an acoustic emission sensor is used to measure noise emanating from the slider to disk interface.

3.2.1 Strain Gages

Eight individual strain gages, Micro Measurements part number EA-06-062AQ-350, were attached to the cantilever beam, and wired into two sets of four active arm Wheatstone bridge configurations, Figure 11. To this point the beam has been called a cantilever beam, when in fact that is a misnomer. In reality it is a dual cantilever beam with additional regions of relative rigidity, see Figure 12. During preliminary trials a strain gage measuring vertical load was damaged. Due to a lack of time the vertical load was rewired into a two active arm Wheatstone Bridge Configuration, shown in Figure 11.

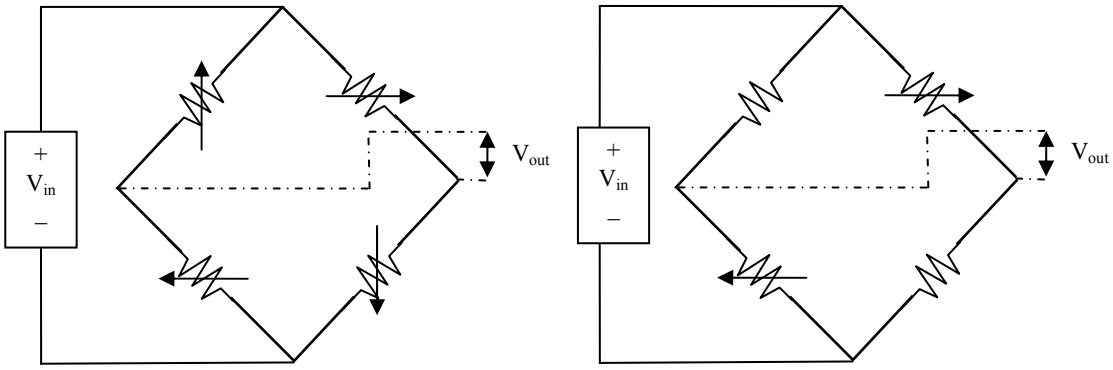

Figure 11: Four Active Arm (left) and Two Active Arm Wheatstone Bridge Circuits

The design of the dual cantilever beam (DCB) makes the strain measurements inherently orthogonal as well as providing a high stiffness ratio. A comparison of

theoretical and experimental strain is shown in Table 2, based on calculations in APPENDIX A: THEORETICAL AND EXPERIMENTAL STRAIN DERIVATION. A comparison of theoretical and experimental stiffness ratios is shown in Table 3, based on calculations in APPENDIX B: STIFFNESS RATIO DERIVATION. Because of the two different moment arms from the point of applied force to the base of each cantilever beam, there

Table 2: Strain Comparison of the Dual Cantilever Beam

	Theoretical Strain	Experimental Strain
Cantilever #1	$49*10^{-6}$	$64*10^{-6}$
Cantilever #2	$28*10^{-6}$	$41*10^{-6}$

Table 3: Stiffness Ratio Comparison of the Dual Cantilever Beam

	Vertical Stiffness		Horizontal Stiffness	
	Theoretical (N/m)	Experimental (V/g)	Theoretical (N/m)	Experimental (V/g)
Cantilever #1	3119	30.5	250450	476
Cantilever #2	241000	1250	10018	24.1
Stiffness Ratio(ND)	77	41	25	20

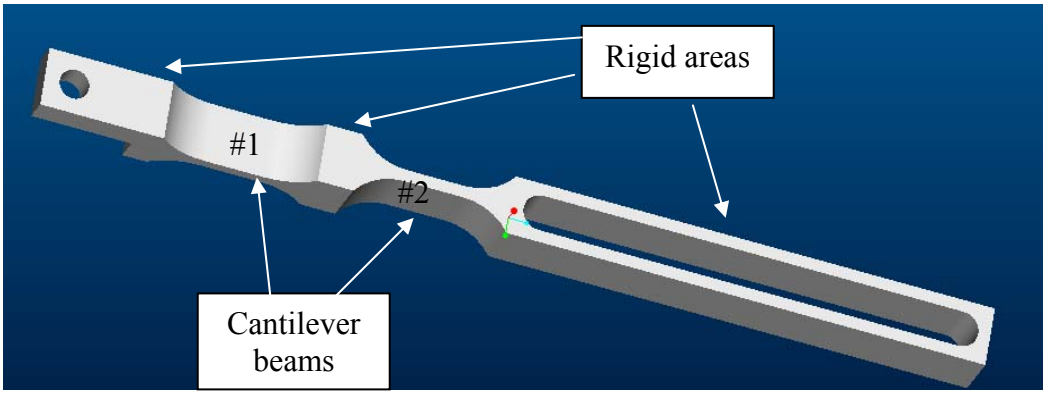

Figure 12: CAD Model of the Dual Cantilever Beam

were two different stiffness ratios, one in the horizontal direction and one in the vertical direction. Numerical results are summarized in Table 3.

From Table 2 and Table 3 it can be seen that theoretical and experimental strain and stiffness values are not the same, yet, they are on the same order of magnitude. This difference could come from many sources such as machining errors in the cantilever beam thickness, signal amplification differences or torsion on the DCB from the length of the gimble arm. These comparisons are of secondary importance. What is truly important is that the voltage output from the strain / friction sensor is linear with load.

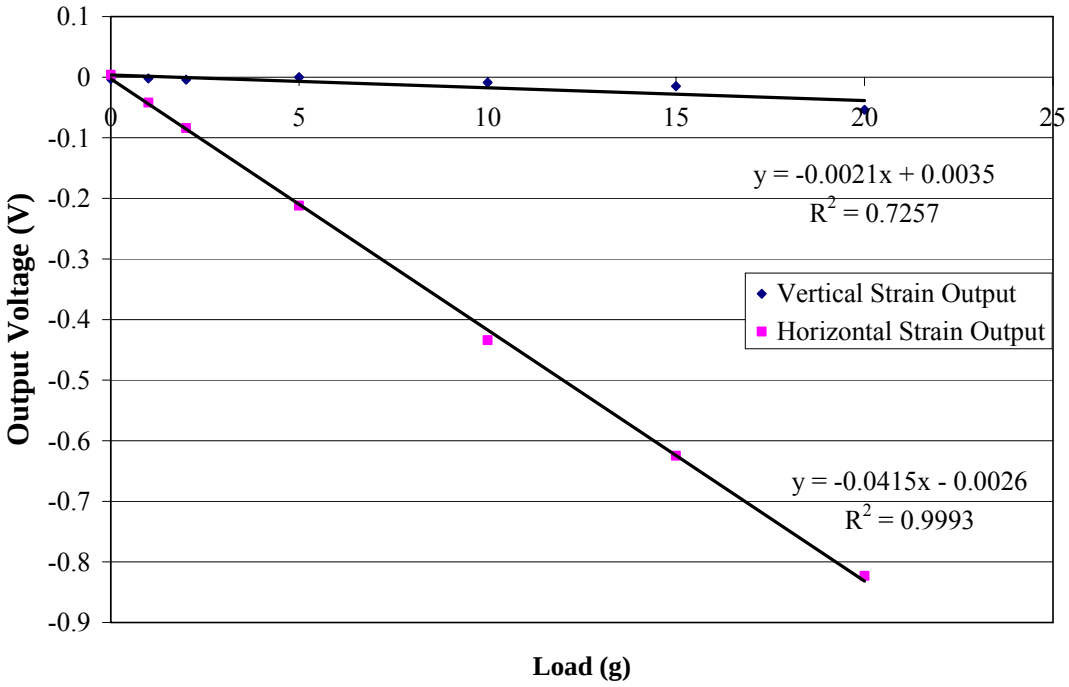

Figure 13: Calibration of Strain Gages – Horizontal Loading

Experimental values in Table 2 and Table 3 come from the calibration curves in both the horizontal, Figure 13, and vertical, Figure 14, directions. Calibration was performed over a range well in excess of the expected values of friction load.

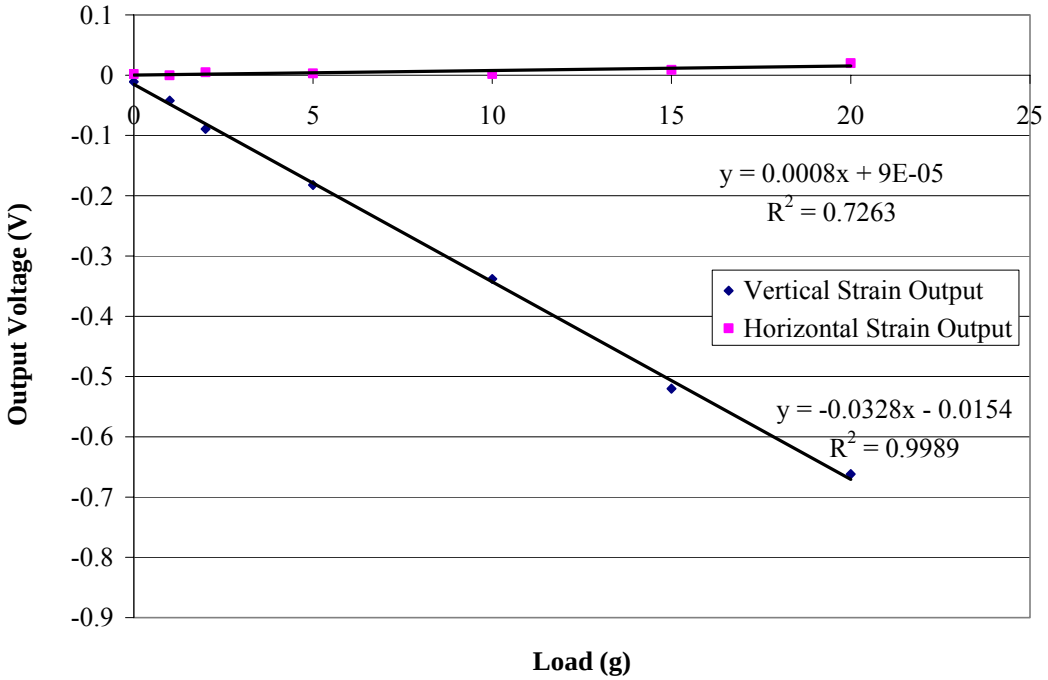

Figure 14: Calibration of Strain Gages – Vertical Loading

Understanding of the strain gage response to noise comes from measurements of "no load" output. Data was taken as would be in an experiment, with the exception that the slider was out of contact with the disk. This was performed for all three disk configurations: 4", 1" and 100 mm silicon wafer. This condition provides baseline data to compare against friction data taken with the slider loaded to design specification. No load friction data is seen in Figure 15. This no load data represents the noise that may be included in the sampled friction data. Figure 15 shows that friction noise is less than 0.1g at any speed for all disk types.

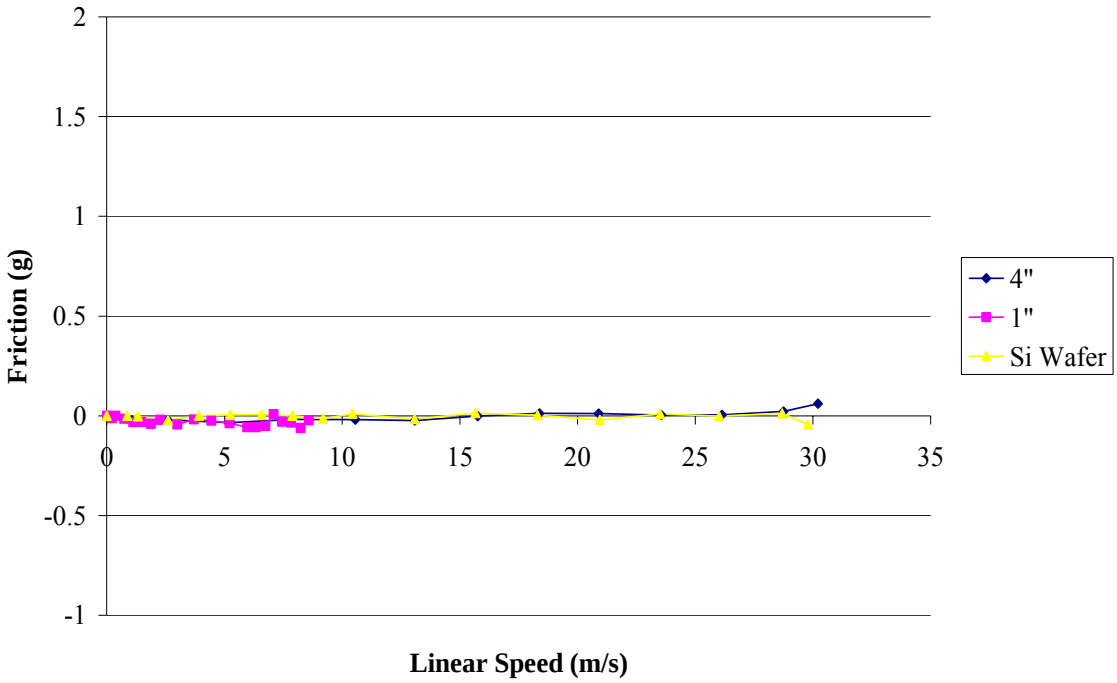

Figure 15: Comparison of Disks - No Load Friction

3.2.2 Capacitance Sensor

The second type of sensor on the test stand is a electrical circuit designed to measure the capacitance of the slider to disk interface. Physically, the slider head and disk form a parallel plate capacitor with air as the dielectric material between the two. This method was previously used by Streator[27] to measure slider fly height in slider head to disk interfaces. The impedance circuit model presented in that work is re-derived in APPENDIX D: MODEL WITH SYSTEM CAPACITANCE FOR HEAD TO DISK INTERFACE CAPACITANCE MEASUREMENT CIRCUIT.

In addition, comparable physical circuit equations are derived to maximize sensitivity of the circuit near the expected capacitance of the interface. Calibration of the capacitance circuit is done using impedance circuit model with system capacitance from [27]. Both models are displayed in Figure 16. Before implementation of the sensor, the

shunt resistor was sized to provide optimum sensitivity at the capacitance calculated by the parallel plate equation using the design fly height of the slider, 13.5 nm. These calculations can be seen in APPENDIX E: PHYSICAL MODEL FOR HEAD TO DISK INTERFACE CAPACITANCE MEASUREMENT CIRCUIT AND MAXIMIZING SENSITIVITY AROUND EXPECTED CAPACITANCE. Using the parallel plate equation is not an ideal approximation because if the slider were parallel to the disk no hydrodynamic lift would be generated and fly height would be zero. Yet, for the purposes of centering the capacitance measurement sensor this approximation is satisfactory.

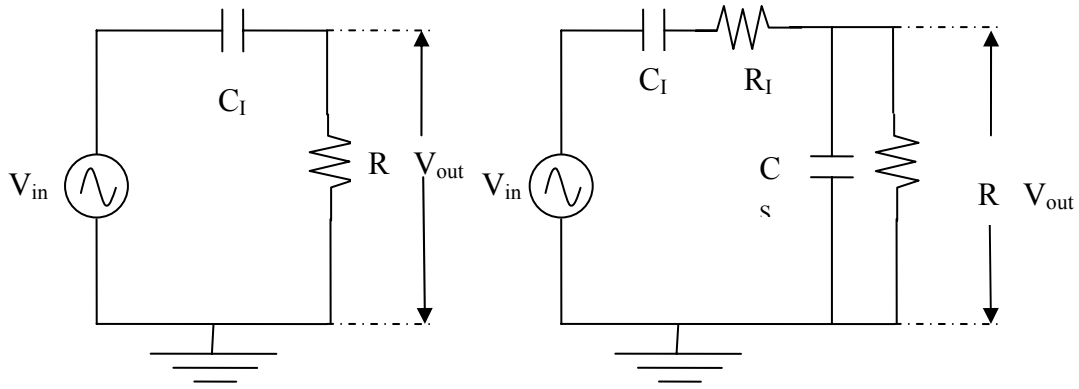

Figure 16: Physical Capacitance Circuit (left) and Model with System Capacitance

To maximize capacitance sensor linear resolution the input frequency and sample frequency are increased to 1 MHz and 10 MHz respectively. Linear resolution is the length of the disk under the flight path of the slider in the time between two data points. Linear resolution is directly proportional to speed of the disk. One additional factor in the linear resolution of the capacitance sensor is the number of samples used in the Fast Fourier Transform (FFT) of the signals. In this work 10 samples are used in the FFT

calculation of one capacitance data point. So, the linear resolution of the capacitance sensor is the length of the disk traversed along the flight path of the slider in the time between a sampled data point and the 10^{th} following data point.

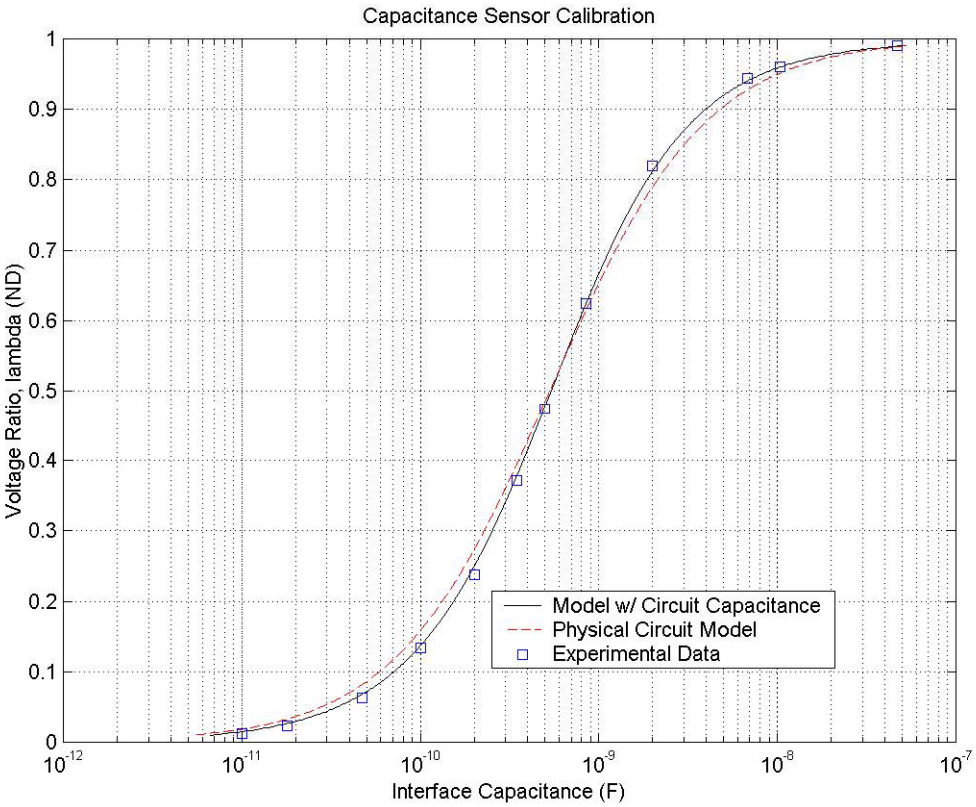

Figure 17: Capacitance Sensor Calibration Curve

Calibration of the capacitance sensor is shown in Figure 17. Experimentally this was carried out by replacing the slider head to disk interface with a known capacitor. For comparison, both the model with circuit capacitance and physical circuit model were plotted with the experimental data. The model with circuit capacitance was fit to the experimental data by adjusting the value of the circuit capacitance until it coincided with experimental data. This method was highly effective. However, if the physical circuit

model was used, relative changes in capacitance would still be detectable. Given that the slider head to disk interface is not an ideal parallel plate capacitor the difference in these two models is negligible for the purpose of this work.

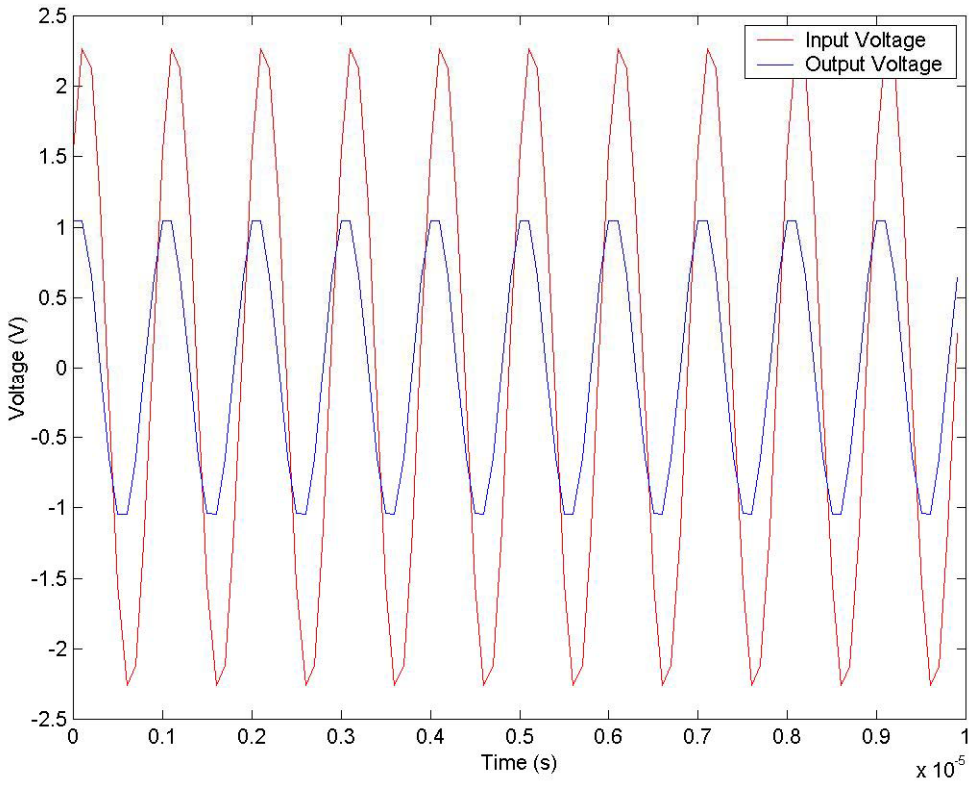

Figure 18: Capacitance Sensor Sample Data

The capacitance sensor is a modulating sensor, it accepts an input signal and changes it in a predictable way. Sample data from the capacitance sensor is shown in Figure 18. The capacitance circuit will modulate the input frequency between the input frequency amplitude and zero. Here the ratio of output voltage to input voltage is about 0.5.

Similarly, no load data was taken to provide a baseline reference for the capacitance circuit. The resulting plot of capacitance versus linear speed is seen in Figure 19.

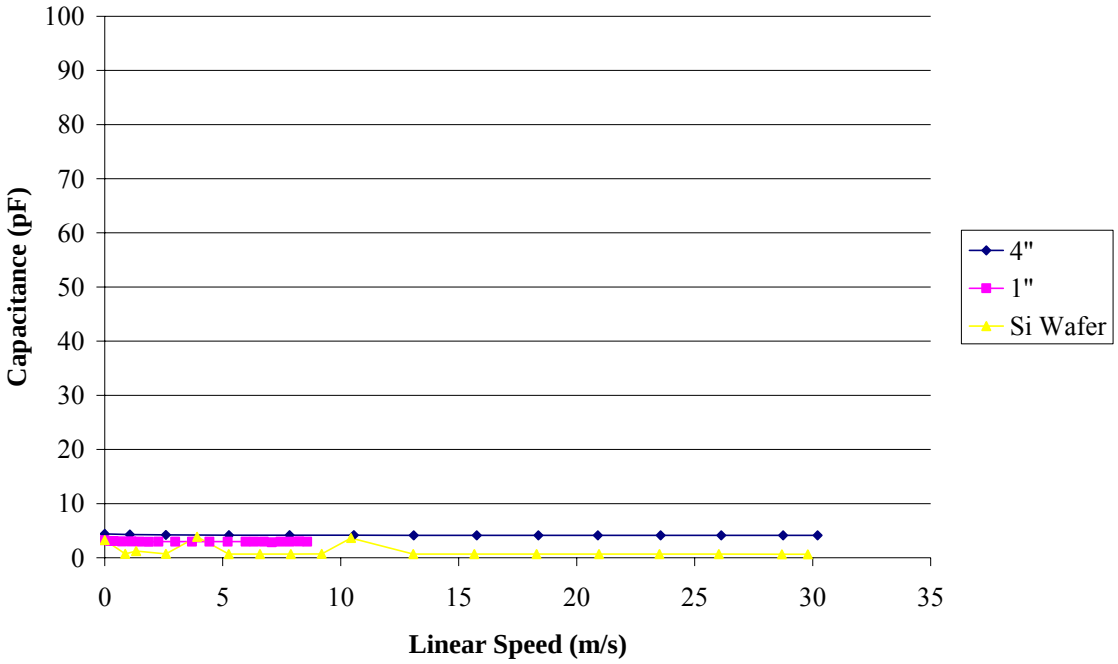

Figure 19: Comparison of Disks - No Load Capacitance

3.2.3 Acoustic Emission Sensor

The third sensor in the test stand, and last used to determine flyability is the acoustic emission sensor. This sensor and pre-amplifier combination was purchased from Physical Acoustics. The sensor is model NANO-30 and the pre-amplifier is model 1220–B. It was recommended and selected because of its wide usable frequency range and compact size. The frequency response was plotted in the sensor calibration certificate, and can be seen in APPENDIX C: ACOUSTIC EMISSION SENSOR CALIBRATION CERTIFICATE. The usable frequency range is roughly 50 kHz to 800

kHz. The sensor wiring diagram is proprietary information. However, it is known that the sensor is piezoelectric based.

No load data was taken for the acoustic emission sensor. It can be seen in Figure 20.

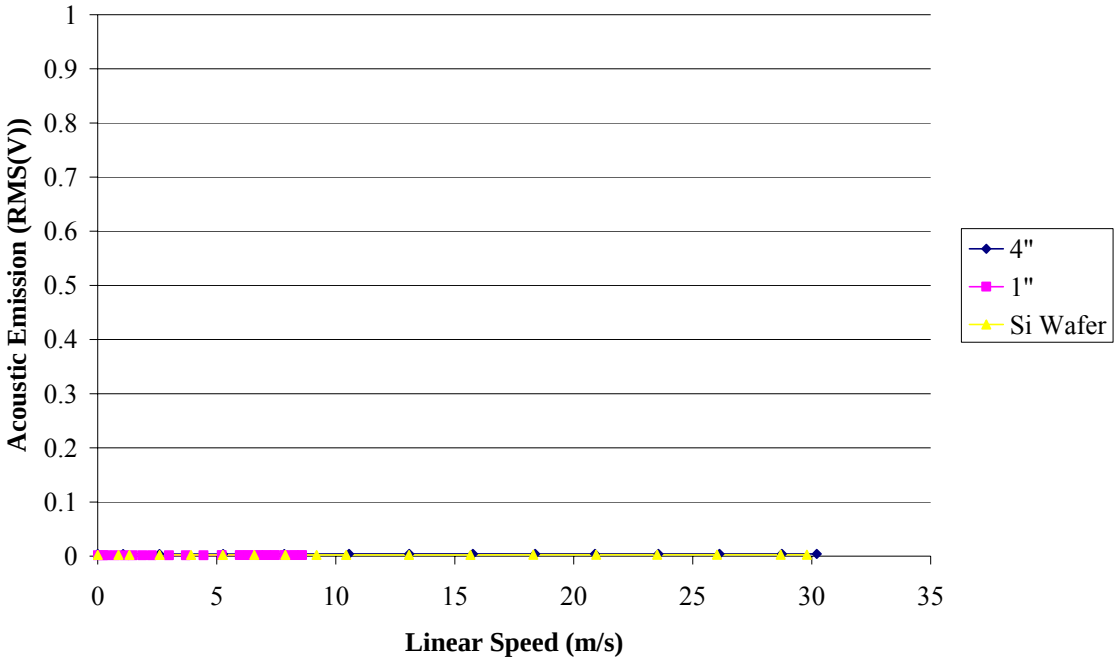

Figure 20: Comparison of Disks – No Load Acoustic Emission

3.2.4 Optical Reflectivity Sensor

The optical reflectivity sensor was used to reliably detect the passing of a specific point on the hub. This is used in two ways. First, two sensors were used concurrently to calibrate the spin speed of the hub to the motor and show that they both vary linearly with motor feedback voltage. Second, it is used to mark the position of the pattern for both FIB patterned samples. Again, the sensor wiring diagram is proprietary information.

No calibration of the sensor was needed. Sample data from an optical reflectivity sensor can be seen in Figure 21.

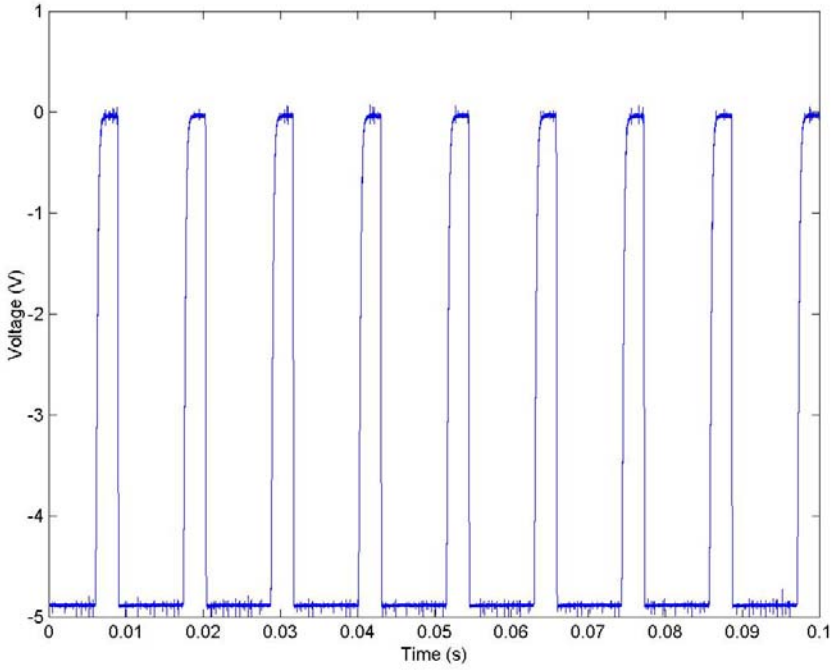

Figure 21: Optical Reflectivity Sensor Sample Signal

CHAPTER 4

EXPERIMENTAL METHODOLOGY

This chapter describes the techniques used throughout the laboratory work and data processing in the experiments. Sample preparation is outlined followed by experimental procedure and data processing.

4.1 Sample Preparation

Experimental specimens were prepared using two methods. Focused ion beam milling was used on industry donated 1" diameter disks while thin film self assembly was used to pattern on silicon wafer substrate.

4.1.1 FIB Samples

One inch diameter hard disk platters were donated by Hitachi Global Storage Technologies. The disks are the same as those purchased in the 1, 2 and 4 gigabyte Microdrive® compact flash form hard drives. Patterning was performed by Christina Freyman, a graduate student in the Department of Materials Science of the Robert R. McCormick School of Engineering and Applied Science at Northwestern University. This was done according to the subcontract agreement of the NSF grant funding this study.

Ideally, an entire disk would be patterned uniformly. However, the Hitachi FB-2000A FIB used to pattern the disks has a maximum etching area of 256 μm square and positioning is done by hand. At that size, etching an entire disk would take weeks of continuous work and would be nearly impossible to align. A compromise was decided to make two different patterns designed to test different scenarios. A low density, large pattern area is made such that the whole slider can be flown over patterned area. A

second pattern area was made at the highest density capability of the FIB. Due to alignment difficulties it is not possible to pattern an area the size of the slider. Instead, two rows of 32 μm square etch areas are etched. In this configuration the slider must fly over the pattern row like an automobile over a speed bump.

The low density, larger pattern area is composed of five 256 μm square burn areas wide by 7 burn areas long, resulting in a total size of 1.23 mm by 1.82 mm. For comparison, the slider is 1.0 mm x 1.3 mm. The burn area pattern came from the software mask discussed in 2.2.3.1.2 on p. 8. It is a black and white bitmap 512 pixels square where black areas are etched by the FIB and white areas are left un-etched. The mask consists of 85 evenly spaced black rows per side length creating 85 white squares per 256 μm side length. The mask can be seen in APPENDIX F: SOFTWARE MASK FOR LOW DENSITY FIB SAMPLE. This mask corresponds to a density of 71 Mbit/in^2.

The high density speed bump patterned area is made of 32 μm square burn areas. Overall, it is 35 burn areas wide by 2 burn areas long resulting in a total size of 1.1 mm by 0.064 mm. The most dense bitmap arrangement resulting in isolated islands is a checkerboard. The bitmap is a 512 pixel square checkerboard. It can be seen in APPENDIX G: SOFTWARE MASK FOR HIGH DENSITY FIB SAMPLE. This mask corresponds to a density of 10 Gbit/in^2.

4.1.2 Thin Film Self Assembly

The thin film self assembly process is outlined in detail in 2.2.3.2.1 starting on p. 9. Work in this thesis simply reproduced results published by others, specifically Guarini.[18,25] Due to time constraints, the process was limited after PMMA development in acetic acid. Instead of transferring the pattern to the silicon substrate by RIE, the PS

matrix is coated with 10 nm of titanium by sputtering. In this condition the pattern can be used as a test specimen. A pictorial description with detailed processing conditions used in this thesis is shown in Figure 22.

Both copolymers used in the thing film patterning were purchased from Polymer Source.[28] Random copolymer (RSMMA) is product number P3437-SMMAramOHT and diblock copolymer (SMMA) is product number P2400-SMMA. Table 4 lists their molecular makeup. Toluene was purchased from Sigma Aldrich Chemical.[29] It is 99.8% toluene, HPLC grade.

Table 4: Copolymer Properties

Property	RSMMA	SMMA
M_W (g/mol)	8900	67100
Composition (%:%::PS:PMMA)	59.4:40.6	70:30
Polydispersity (M_W/M_N)	1.47	1.09

4.1.3 Sliders

Experimental samples of sliders were donated by Read Rite Corporation. Recently Read Rite was purchased by Western Digital. The donated sliders have three different air bearing profiles yet no distinction is made between the three in experimental data. This is done because the performance characteristics of the three sliders are the same. Performance characteristics are found in Table 5.

Table 5: Slider Performance Characteristics

Slider Number	Slider (Part Number)	Gram Load (g)	Fly Height (nm)	Length (mm)	Width (mm)
1	64232-02 A	2.5	13.5	1.3	1.0

2	64296-01 A	2.5	13.5	1.3	1.0
3	64297-01 A	2.5	13.5	1.3	1.0

4.2 Experimental Procedure

A systematic procedure was used to conduct the experiments. It is listed below.

4.2.1 General Procedure

1) All electronics are turned on 30 minutes or more before the start of data acquisition to allow for warm up.

2) A slider is attached to the gimble arm.

3) The sample is loaded onto the appropriate hub and the hub is attached to the hard drive chassis.

4) LabVIEW is started. High Speed Data Logger.vi and High Speed Data Reader – B.vi are opened.

5) Settings on High Speed Data Logger.vi are set as shown in Table 6.

Table 6: High Speed Data Logger.vi Settings

Field	Field Entry
Device	1
Channel	channel0,channel1,channel2,channel3
File Header Text	(Nothing required)
Scan Rate	10000000
Buffer Size	8000000
# of Scans to Write at a Time	1000001
Max # of scans to write to file	1000001

6) The radial position of the slider is adjusted as appropriate.

7) The capacitance circuit wire is inserted into the mercury cup.

8) The slider head is lowered on the disk until the vertical load DMM reaches the proper voltage.

9) Power supply #3 is turned to maximum voltage, bringing the sample to highest rotational speed.

10) High Speed Data Logger.vi is run.

11) High Speed Data Reader-B.vi is run and data is saved in an appropriate folder.

12) Power supply #3 voltage is lowered until motor feedback voltage reaches next sample speed.

If voltage is greater than 0, loop back to 9); otherwise, go to 13).

13) Data processing is done with Matlab.

14) Processed data is plotted in Microsoft Excel, checked for errors and experiments are repeated if necessary.

Step 1: RCA clean wafer. Acetone rinse; methanol rinse; DI rinse; dry with compressed air.	
Step 2: Spin coat RSMMA solution (1% by weight in Toluene) at 1000 RPM until solvent evaporation. ~90nm.	
Step 3: Bond of RSMMA to native SiO_2 by baking at180ºC for 3 hours in air.	
Step 4: Rinse off un-bonded RSMMA by thoroughly rinsing with toluene and spin drying. Repeat twice. ~7nm.	
Step 5: Spin coat SMMA solution (1% by weight in Toluene) at 3000 RPM until solvent evaporation. ~42nm	
Step 6: Anneal, at 160˚C for 5 hours in air, to promote SMMA self assembly.	
Step 7: Expose to 1800mJ of UV light to crosslink PS and degrade PMMA.	
Step 8: Develop for 3 minutes in 100% glacial acetic acid with ultrasonic agitation to remove PMMA. ~30nm.	
Step 9: Sputter deposit 10 nm Ti.	

Figure 22: Diagram of Thin Film Self Assembly Process

4.2.2 Special Procedures

The FIB patterned 1" disks require deviations from the general procedure. Since the disks are patterned only in small regions, an optical sensor was used to locate the data taken over the patterned area from data taken over un-patterned areas. This was done by aligning the edge of a strip of black tape, which is stuck to the hub, with the patterned region. As the tape passed in front of the optical reflectivity sensor the voltage jumps from -5 V to 0 V. Since the data acquisition takes simultaneous measurements, the jump in the optical reflectivity channel of measurement corresponded with other channels' measurement of the patterned region. The difficulty with this method is that the data acquisition card has only four channels. In the standard configuration one channel was allocated to friction, one to AE, and two to capacitance: one input voltage and one output voltage. Adding the optical reflectivity sensor meant some other sensor was disconnected. In order to gather data from all sensors the experiment was run twice. First the optical reflectivity sensor replaced AE, then it replaced friction.

The geometry of the silicon wafer also caused a deviation. Because the thin film patterning was done on silicon wafer there was no way to attach a mercury cup. Hence, the capacitance circuit could not be completed and no capacitance data was taken. Friction and AE measurements are used to judge flyability over the thin film pattern.

4.3 Signal Processing

After the data had been sampled several Matlab scripts were used to process raw data into a usable form. Processing is done on data from the three sensors used to determine flyability. The only processing done on optical reflectivity data was searching for leading or trailing edges of the data spikes.

4.3.1 Friction Calculations

Each time High Speed Data Logger.vi is run 1 million data samples are taken for each of the four channels. The samples spanned 0.1 second of time or 0.2 to 11.5 revolutions of the disk, depending on the speed of the disk. An average of the 1 million friction data points is performed to summarize the samples into a usable value. After averaging, the measurement is still in units of volts. The calibration slope shown in Figure 13 is used to convert volts to grams.

A special case exists for the FIB regional charts. It was observed that the cantilever beam could be excited to vibration at certain frequencies. A technique outlined by Streator[30] was used to mathematically remove the vibration effects from the friction data. Vibrations were subtracted out in the frequency domain based on a one degree of freedom model of the cantilever beam. Then the data was then converted back to time domain for averaging as described above. This is the source of the friction values plotted in Results and Discussion.

4.3.2 Capacitance Calculations

Raw data from the capacitance circuit is shown in Figure 18. FFT of 10 data point windows is first calculated for both input and output data. From the FFTs, the maximum amplitude signal is chosen regardless of the frequency. For input data this is always the amplitude of the input frequency because it's so large. For the output data the largest amplitude will be the output signal, so long as the slider is in close proximity to the disk. If the circuit is completely open, i.e. the slider is more than half a millimeter or so from the disk, the largest amplitude can be ambient noise. However, it becomes obvious when this is the case.

Next, the input voltage amplitude is divided by its corresponding output voltage amplitude to form a voltage ratio. This voltage ratio is used in the quadratic formula to solve Equation 33. At this point data values are capacitance with units of farads. In this work capacitance values are not converted to fly heights for reasons discussed in Results and Discussion.

At this point in the capacitance calculations the data has been reduced to 100,000 points. This is summarized, like friction, by taking the average. That average value is multiplied by 10^{12} to convert units to pF, which are in the range of expected capacitance. This is the source of the capacitance values plotted in Results and Discussion.

4.3.3 Acoustic Emission Calculations

Calibration of the acoustic emission sensor is difficult. A frequency response chart is provided by the manufacturer, but this chart is not flat, or even regular. Also, achieving the same response would require that the same sensor to base coupling method and same base material be used. This was not possible in the test stand. For these reasons the output of the acoustic emission sensor is left as voltage and is evaluated only relative to baseline data. Root mean square (RMS) AE voltage signal is plotted in Results and Discussion.

4.3.4 Optical Reflectivity Calculations

Optical reflectivity is not used to determine flyability. The sampled signal is only used to locate other import regions of data.

CHAPTER 5

RESULTS AND DISCUSSION

This chapter describes the experimental results for determining the flyability of current generation read/write slider heads over patterned media. These results include experiments run with samples created by focused ion beam milling and by thin film patterning. Baseline data is taken as a reference to judge flyability against. Results of the three types of patterning, sliders, and experimental data plots are organized into categories.

5.1 Patterning

Results of the three patterned disks are summarized in the following images.

5.1.1 FIB Patterning

AFM images of the FIB samples can be seen in Figure 23 and Figure 24. Figure 23, of the low density FIB sample, clearly shows an organized pattern. Yet, it is somewhat different from software mask shown in Figure 53. The side trenches are distinct pits when a connected line was desired. The Hitachi FB-2000A has no adjustment for this type of error. Most likely, the pits could have been forced to connect by etching larger trenches or by taking multiple passes during etching to allow beam drift and misplacement to widen the pits. Neither option is a good alternative. Since the pattern is regular and the desired depth is met, the sample was considered satisfactory for tribological testing.

Figure 24 shows the etched result of the high density pattern used by the Hitachi FIB. The sample is not as regular as the low density sample yet some pattern is distinguishable. The sample is considered good enough to test for flyability experiments.

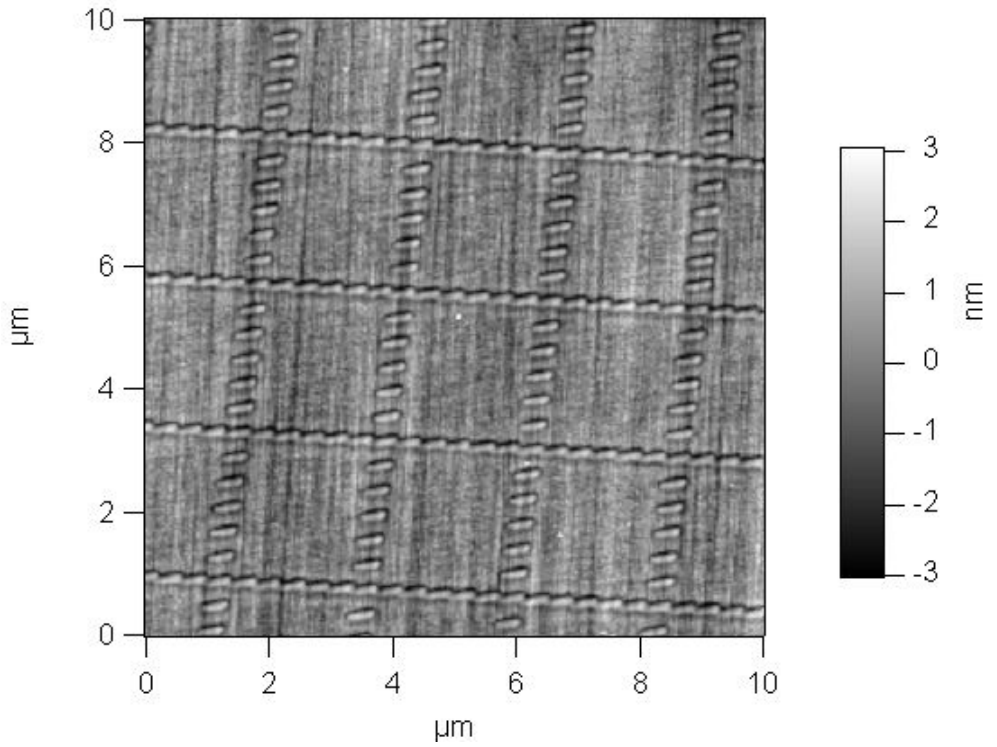

Figure 23: AFM Image of Low Density FIB Sample

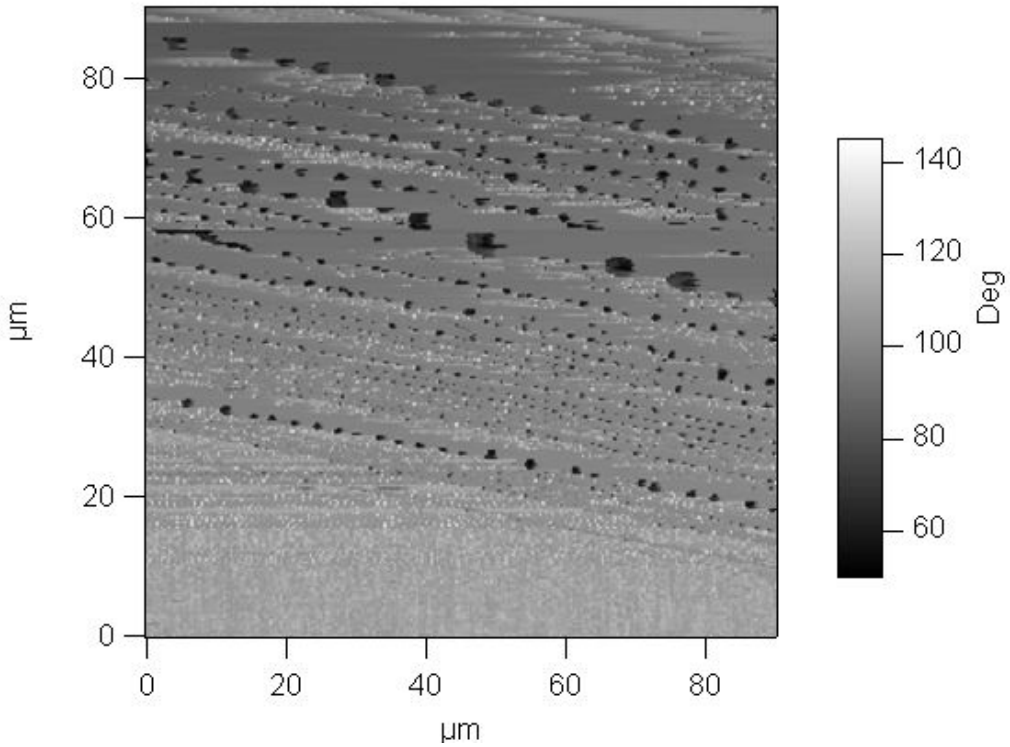

Figure 24: AFM Image of High Density FIB Sample

5.1.2 Thin Film Self Assembly

AFM images were taken at several points during the processing. Two important stages are displayed in Figure 25 and Figure 26. Figure 25 is an image taken after step 4) of the thin film self assembly process. At this stage the polymer has less than 2 nm surface roughness. The dark and light colors are the phase separation of PS and PMMA which can be detected by the AFM because the stiffness of the materials are different.

Figure 26 shows the final testable sample after step 8) of the thin film self assembly process had been finished. The height change from peaks to valley is about 16 nm. Compared to the 6 nm determined by Rettner[12] this is a worst-case scenario for flyability.

Wormlike structures are visible in the final sample. This is caused by the SMMA layer being 5 nm above target thickness. These structures are not considered when calculating the dot density of the thin film self assembly sample. The 700 Gbit/in^2 density calculation is based on a dot periodicity lengths of 36 nm presented by Guarini[18] which have been sufficiently reproduced.

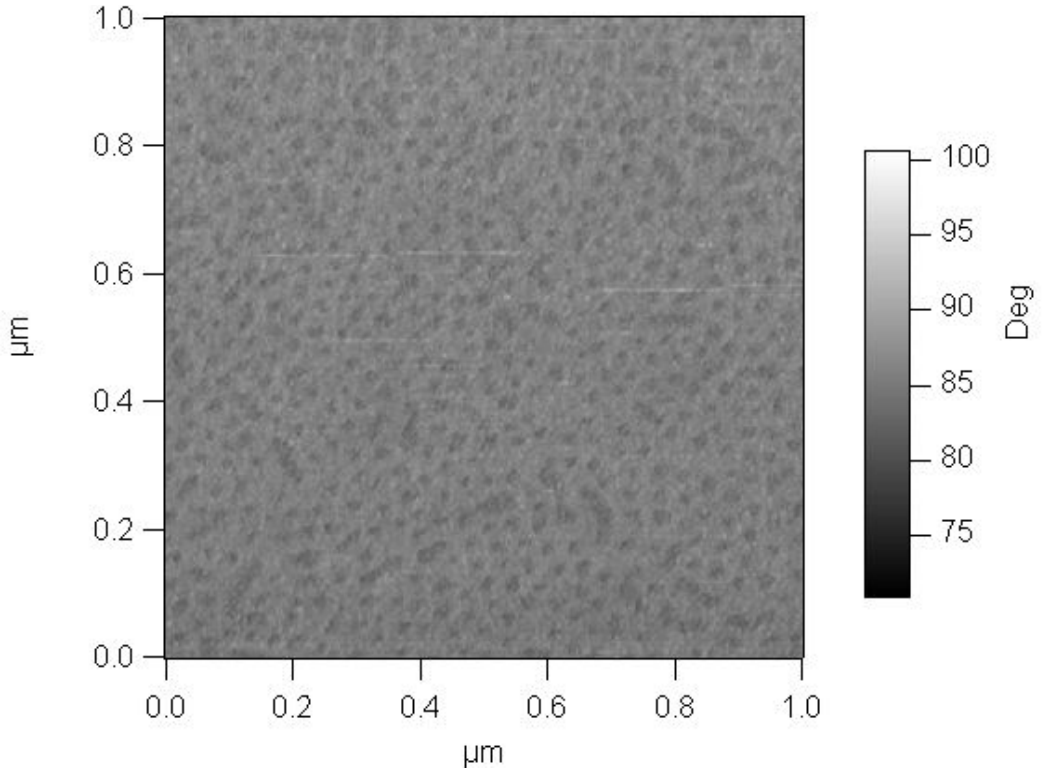

Figure 25: AFM Image of Thin Film Self Assembly After Step 5, Anneal

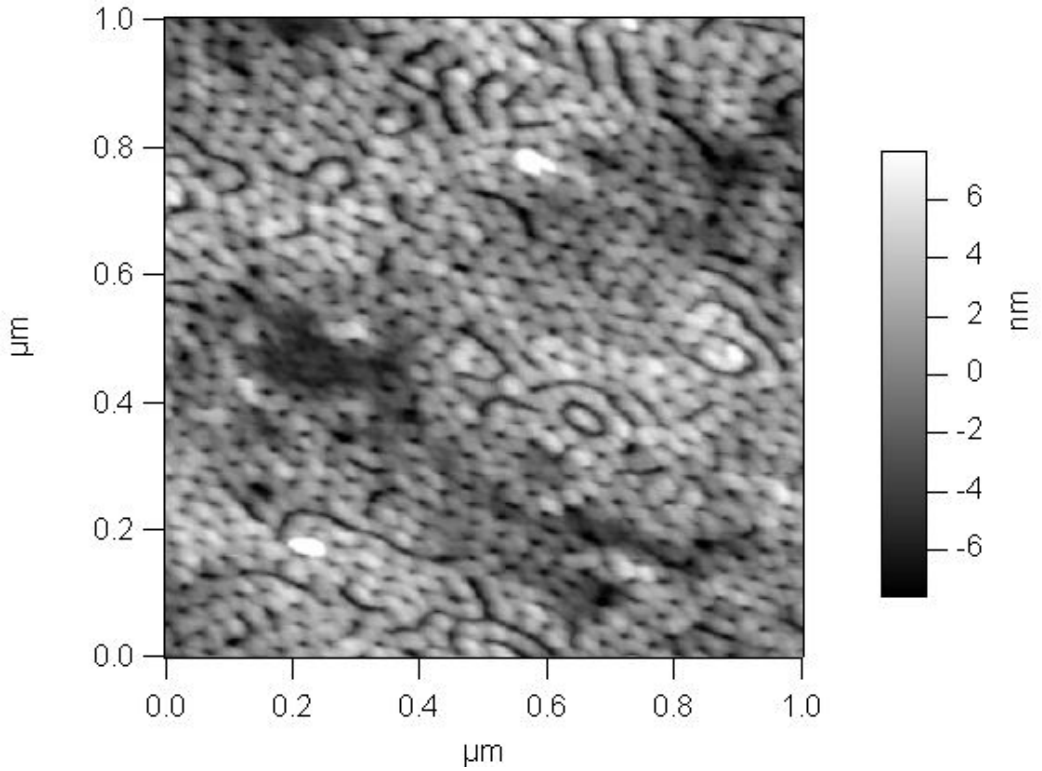

Figure 26: AFM Image of Thin Film Self Assembly After Step 8, Sputter Ti

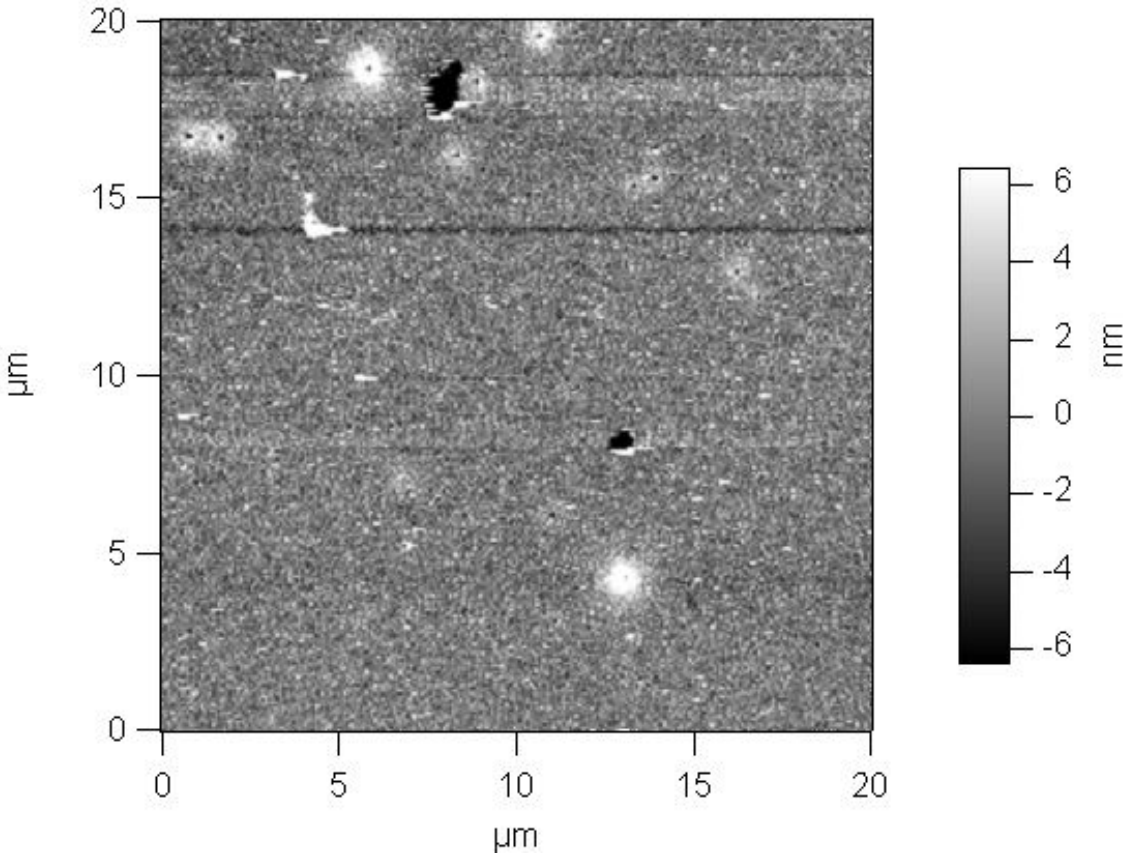

Figure 27: AFM Image of Thin Film Self Assembly, Zoomed Out

5.2 Slider Heads

Slider heads used in this work have three different air bearing (AB) surface profiles. For testing purposes the air bearing surface differences are not considered because the important design characteristics, gram load and fly height, are the same for both AB profiles. Various views of sliders can be seen in APPENDIX H: OPTICAL IMAGES OF SLIDER HEADS.

It was found that wear tracks, as seen in Figure 30, developed for two reasons. First, based on information obtained from Western Digital, the supplier of the slider, lift off of these sliders should be achieved by 7 m/s linear speed. This is not a predicted lift

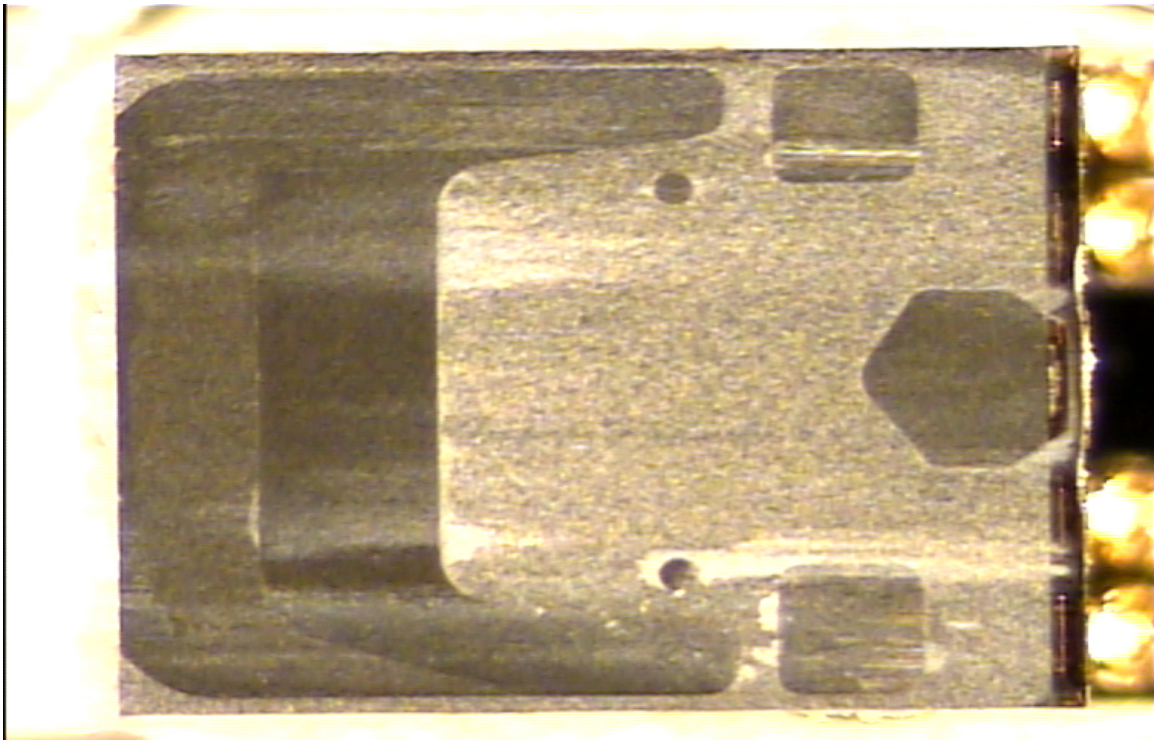

Figure 28: Slider With Particulate Contamination

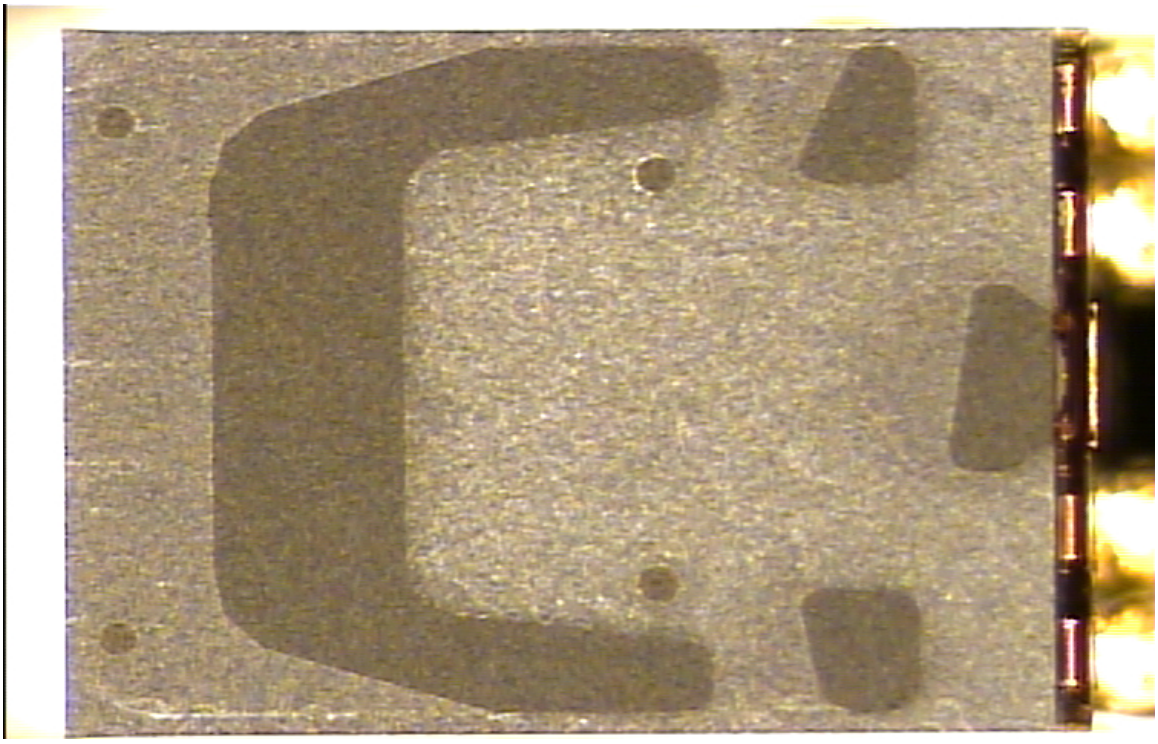

Figure 29: Slider #5, No Contamination After Use in Four Consecutive Tests

off speed, but is a reference speed at which lift off should have occurred. With this in mind, if wear tracks formed immediately in any test it is probably due to particulate contamination of the head to disk interface. Therefore, the test was scrubbed and the slider was replaced. If a wear track formed later during an experiment it was assumed to be from lack of speed and full hydrodynamic lubrication. In this case the experiment would be completed. An image of a particulate contaminated slider that caused a wear track is shown in Figure 28.

In some cases a single slider was used in multiple tests. To confirm that this is acceptable an image was taken of slider #5, after use in 4 consecutive tests. It is shown in Figure 29, and had no visible contamination.

A sample wear track is shown in Figure 30.

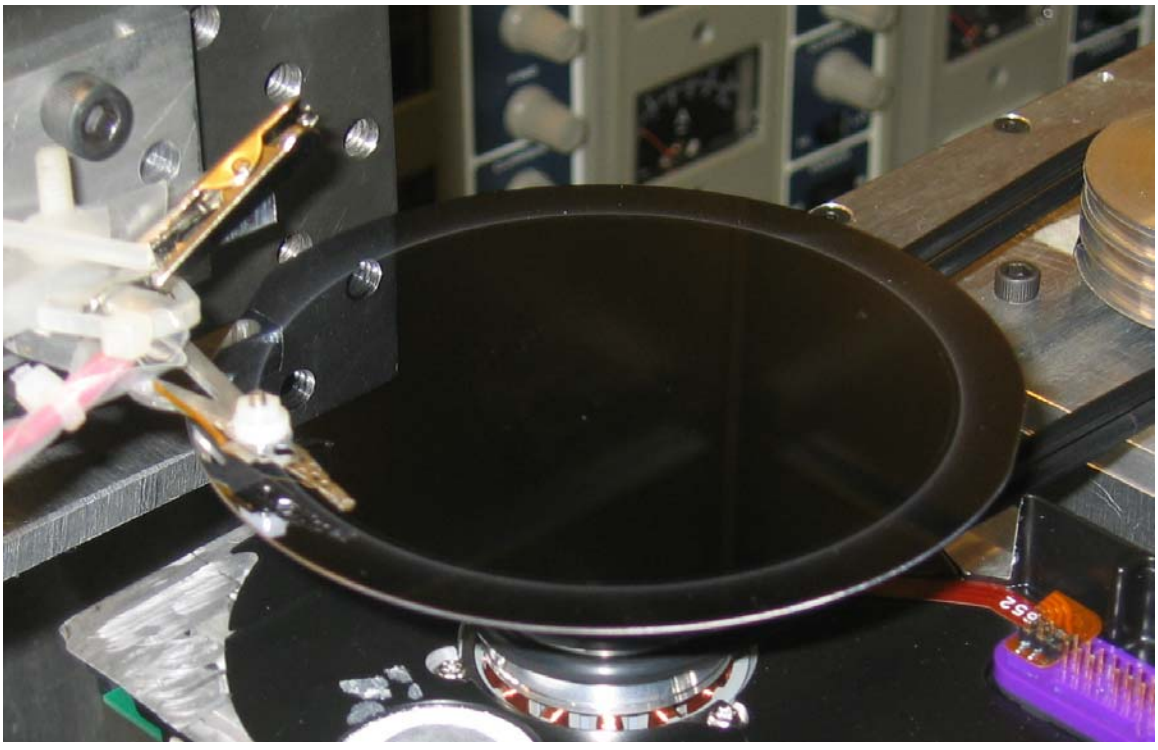

Figure 30: Example of Wear Track Formation and Si Wafer Configuration

5.3 Testing Results

In this section plots of experimental data are shown and discussed by disk type.

5.3.1 4” Disk Baseline Results

4” disks are the most common disk size in the data storage industry. For this reason experimental data taken from non-patterned 4” disks is considered control data for reference other sample types against. No method for patterning a 4” disk was available so there is no experimental data taken for a patterned 4” disk.

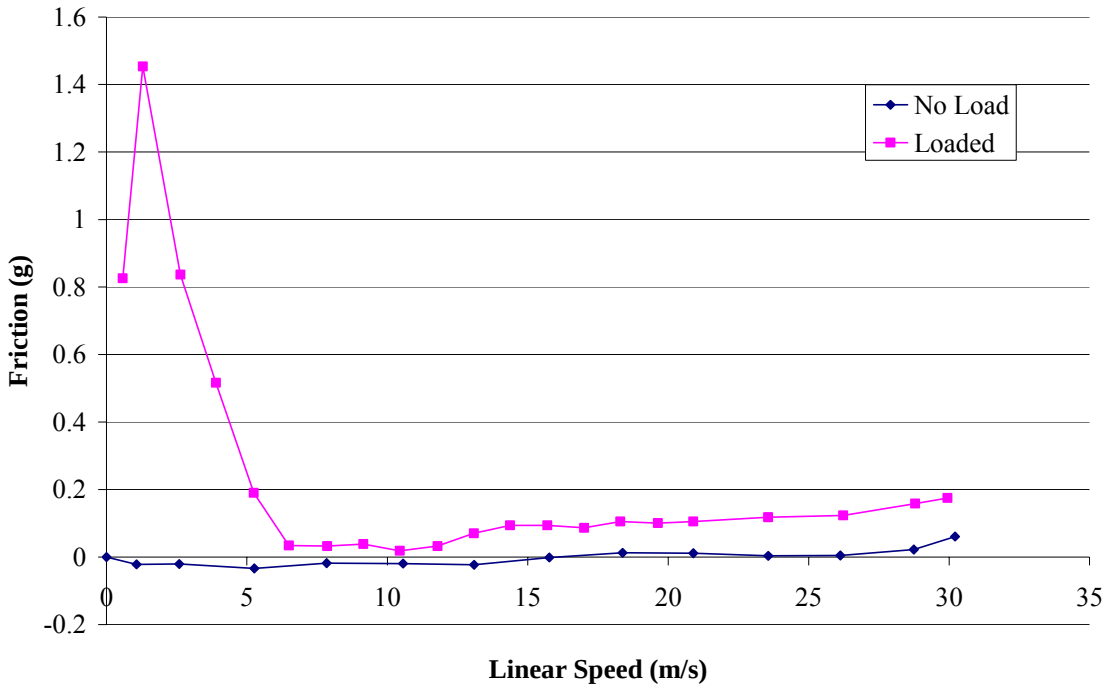

Figure 31: 4” Disk Baseline Data – Friction

Figure 31 shows friction as a function of sliding speed for two data series. The first is no load data taken with the slider head out of contact with the disk. The line gives a clear picture of the amount of background noise that is measured for each speed. Compared to that is loaded data where the slider has been loaded to full design load, 2.5

g. Here the friction at linear speeds lower than ~7 m/s is significantly higher that above 7 m/s. This corresponds with the reference speed given by Western Digital. This change in friction measurements is interpreted as the difference between not flying and flying. The friction is constant from 7-11 m/s then increases slightly but steadily until 31 m/s. Loaded friction data for zero linear speed is never plotted because no flying can exist at zero linear speed and static friction would only skew the vertical axis.

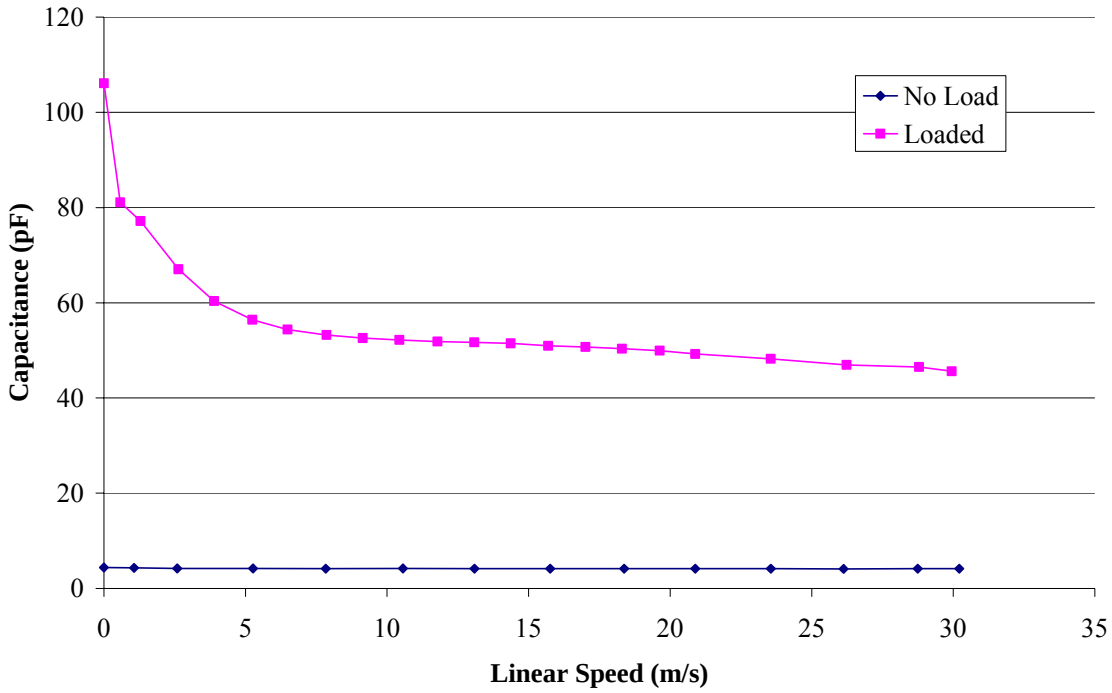

Figure 32: 4" Disk Baseline Data – Capacitance

Figure 32 shows capacitance as a function of sliding speed for no load and design load. As mentioned in 4.3.2 on page 43, capacitance is not converted to actual fly height because our focus is not on the actual flying height. As an example, a capacitance of 100 pF corresponds to a fly height of 115 nm. This number is clearly erroneous because the design fly height of the slider is 13.5 nm. The calculation is complicated by the complex

surface and the non parallel orientation of the flying slider head. However, capacitance can be considered as inversely related to fly height. With that mindset, one arrives at the conclusion that the loaded capacitance data series in Figure 32 shows take off speed in the same region as friction, ~7 m/s. Past 7 m/s capacitance decreases slightly to a minimum at 31 m/s.

Figure 33 shows acoustic emission as a function of sliding speed for no load and loaded conditions. RMS acoustic emission is considered an indicator of the intensity and frequency of head to disk intermittent contact. At zero speed AE is zero. Drastic increases are seen for the first two data points, then AE begins to taper off with ranges of different slopes. The first slope is very steep from 2 to 3 m/s. The slope is less steep from 3 to 7 m/s and even shallower from 7 to 15. From 15 to 25 m/s the trend is still downward, but the slope is slightly steeper. From 26 to 30 m/s the AE is basically flat.

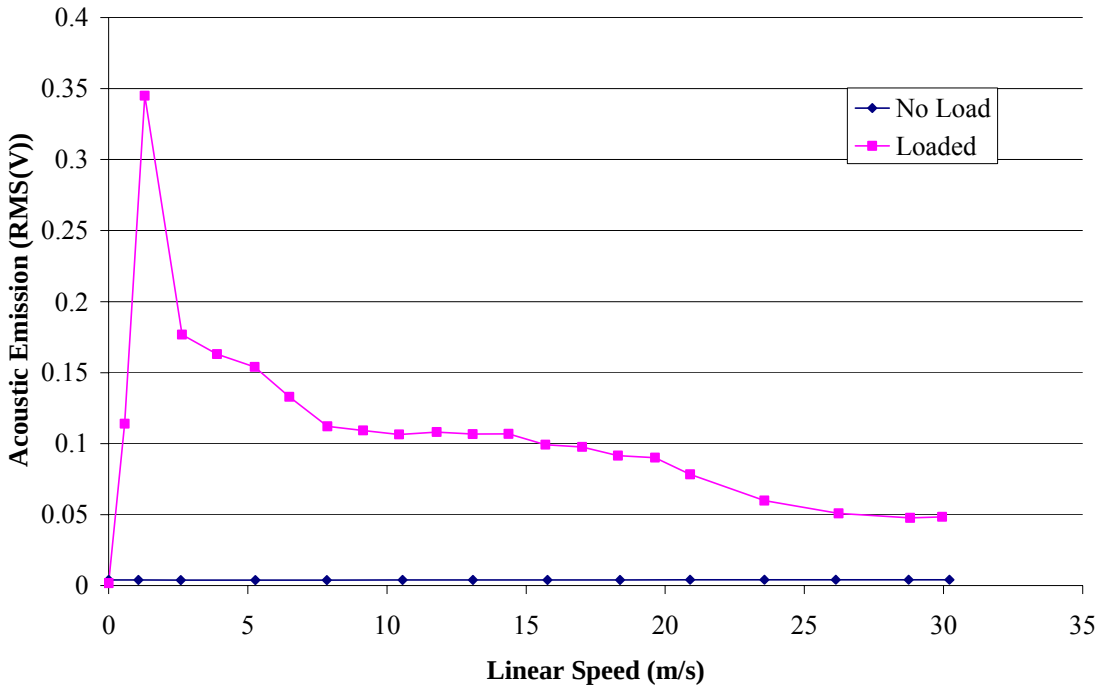

Figure 33: 4" Disk Baseline Data – Acoustic Emission

The point at which liftoff occurs is left to interpretation. Fly height is at a minimum at slider liftoff, therefore intermittent contact with the disk is likely. As the speed and therefore fly height increases the intermittent contact decreases. This relationship would be a function of the asperity size distribution on the disk, which is not covered in this work.

5.3.2 FIB Low Density Pattern Results

Low and High density FIB samples were data processed in two ways. First, data from the entire disk is calculated. Since the patterned area represents a small portion of the sample the results are expected to be similar to non-patterned media. A second method focuses on a given length of disk centered on the pattern. The data outside this area is disregarded. This was done by using the optical reflectivity sensor output to determine the location of the pattern. The actual amount of data processed is a function of linear speed.

5.3.2.1 FIB Low Density Whole Disk Calculation Results

In Figure 34 the low density FIB whole disk friction data is erratic. Friction is about 6 grams from 0-1.8 m/s. By 3.6 m/s it has fallen to 1.2 g. A spike to just over 4 grams is seen at 4.5 m/s. Above 6 m/s friction is down to no load levels.

In Figure 35, which shows low density FIB whole disk capacitance results, irregularity is consistent. Patterned media capacitance values are above non-patterned media data from 0-1.8 m/s, then below from 2-2.2 m/s. Next two large spikes are seen at 3 and 4 m/s. Finally, values are at or below non-patterned data above 4.2 m/s.

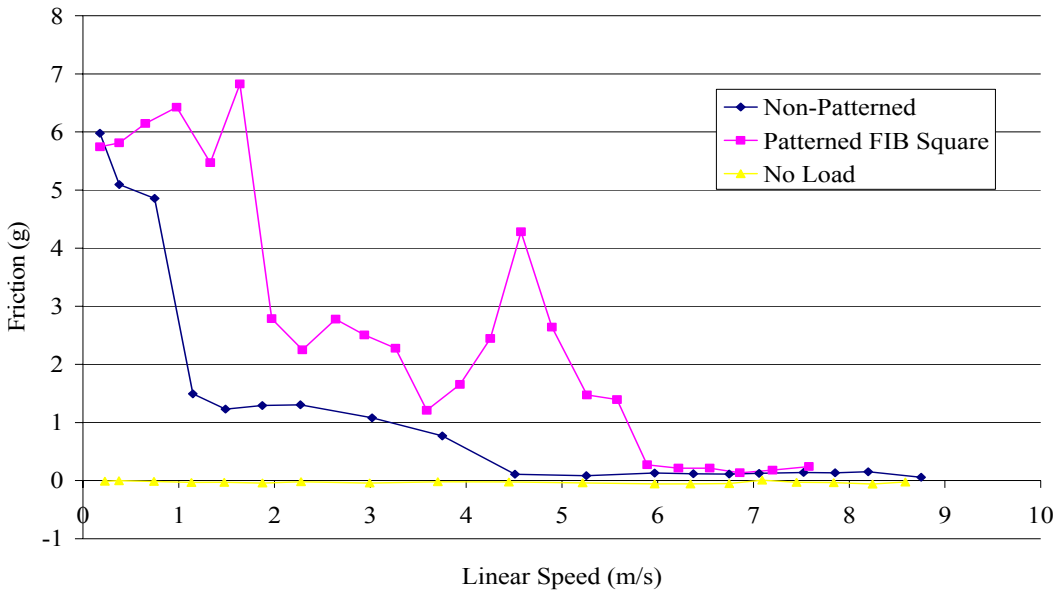

Figure 34: FIB Low Density Whole Disk Calculation Results – Friction

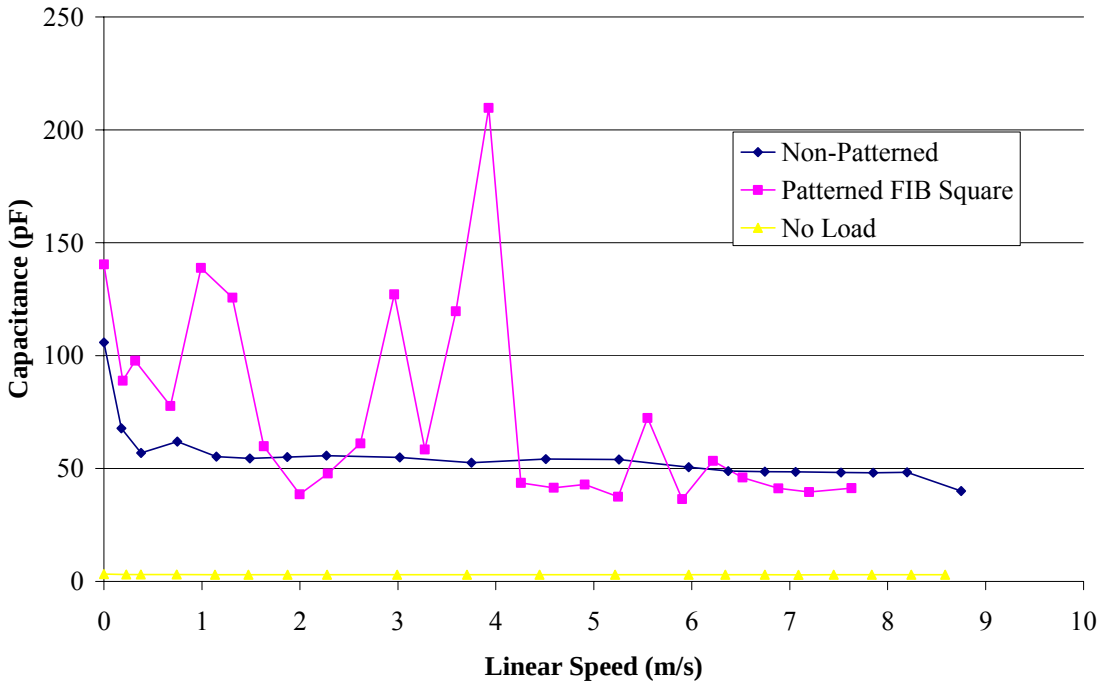

Figure 35: FIB Low Density Whole Disk Calculation Results – Capacitance

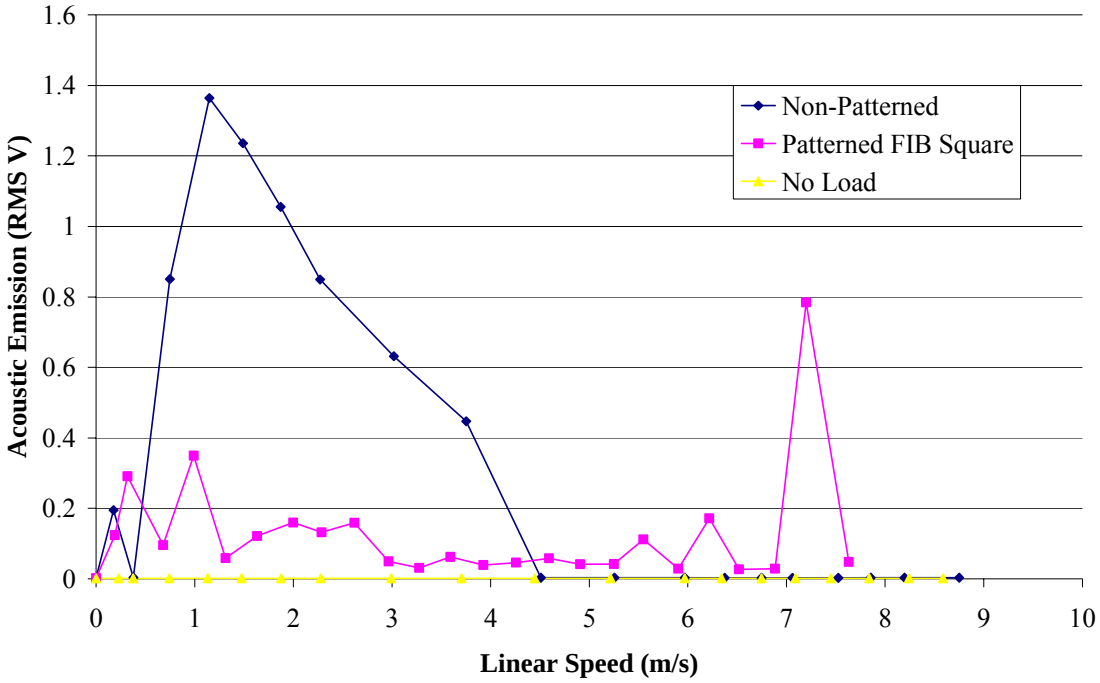

Figure 36: FIB Low Density Whole Disk Calculation Results – Acoustic Emission

In Figure 36, low density FIB whole disk AE spikes are seen at 0.5, 1 and 7.2 m/s. These values are separated by lengths of relative smoothness, making the entire curve erratic.

Figures 34 through 36 show that the friction and capacitance plots agree on a take off speed of 6 m/s, while the acoustic emission does not show any take off speed. This shows some difference between non-patterned and the patterned disks, but the difference is not constant. One possible explanation for this difference is the presence of visible scratches on a portion of the non-patterned area of the patterned disks. Scratches most likely occurred during shipping and handling from Northwestern to Georgia Tech.

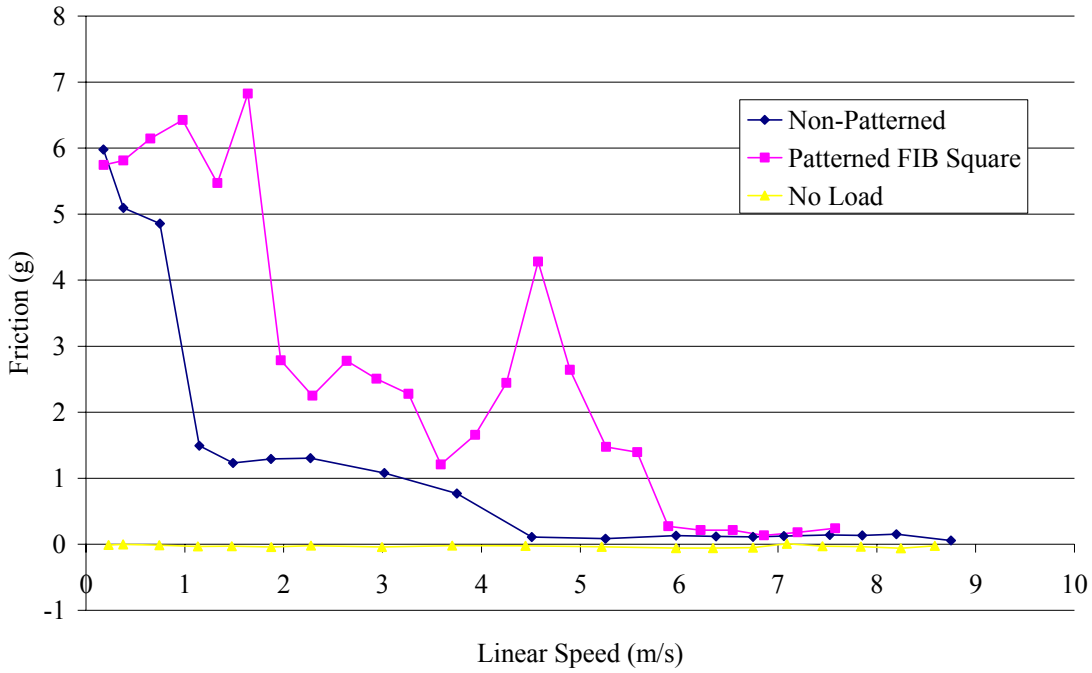

Figure 37: FIB Low Density 3 mm Region Calculation Results – Friction

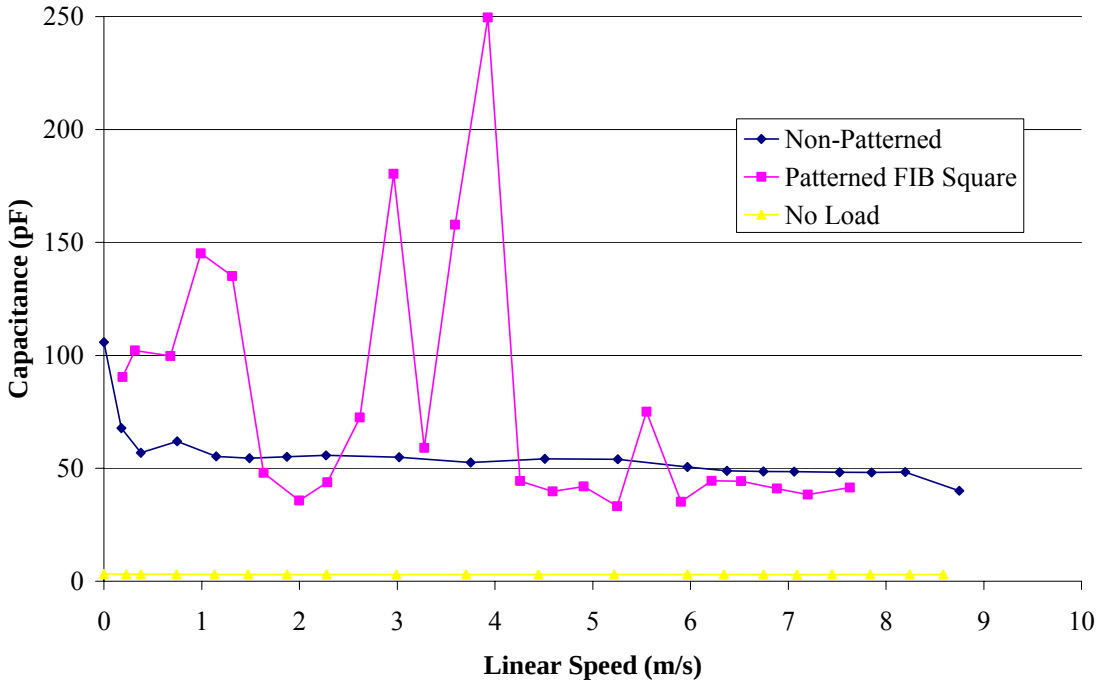

Figure 38: FIB Low Density 3 mm Region Calculation Results – Capacitance

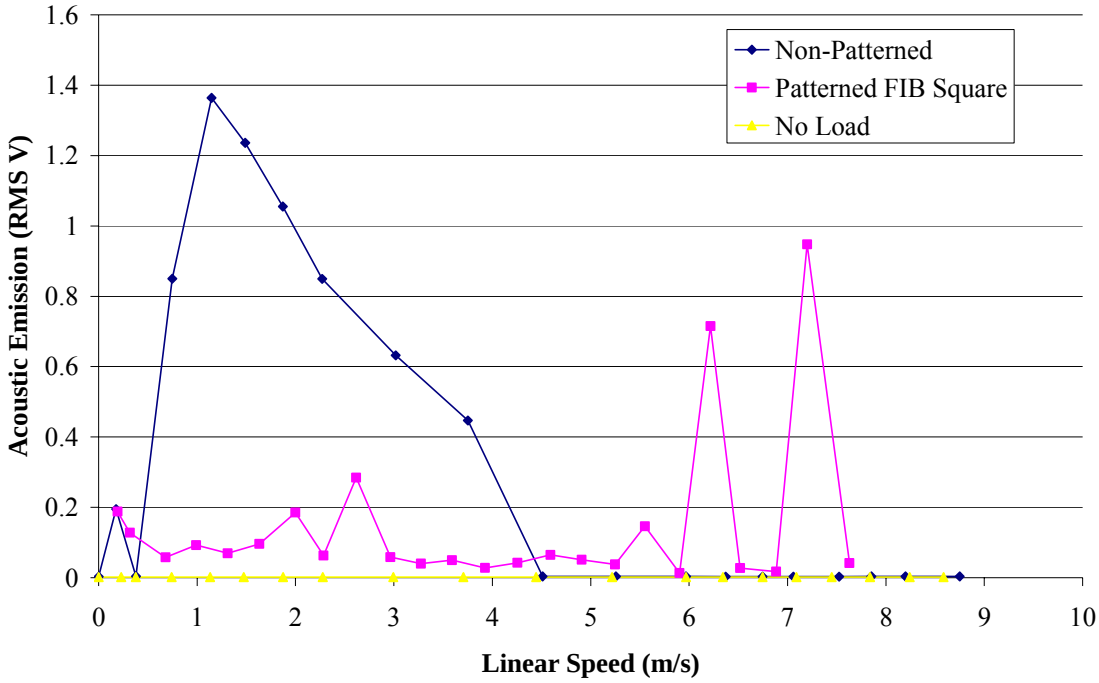

Figure 39: FIB Low Density 3 mm Region Calculation Results – Acoustic Emission

5.3.2.2 FIB Low Density 3 mm Region Calculation Results

Figure 37, low density FIB regional friction results are identical to the whole disk friction calculations. This similarity highlights the fact that low density FIB patterning did not affect flyability.

Figure 38, low density FIB regional capacitance has the same shape as the comparable whole disk calculations, but the peaks at 3 and 4 m/s are amplified somewhat. However, these changes are insignificant and do not change the overall shape in absolute values or relative to the baseline data.

Figure 39, low density FIB regional AE results, are somewhat different than the whole disk results. Peaks formerly at 0.5 and 1 m/s have moved to 2 and 3 m/s. A peak at 6 m/s is added and the spike at 7 m/s is amplified.

Figure 37, Figure 38, and Figure 39 s are highly similar to whole disk calculation

results. Curve shapes are identical with only minor value differences. Again, the friction and capacitance plots agree on a take off speed of 6 m/s, while the acoustic emission does not show any take off speed. All three show some difference between non-patterned and the patterned disk. However no visible scratches were present in the patterned region. The previous speculation on the effects of scratches conflicts with these results. Since there were no scratches in the patterned region and the plots are so similar the effect of the scratches must be negligible.

5.3.3 FIB High Density Pattern Results

The high density experiments were processed in the same ways as the low density results.

5.3.3.1 FIB High Density Whole Disk Calculation Results

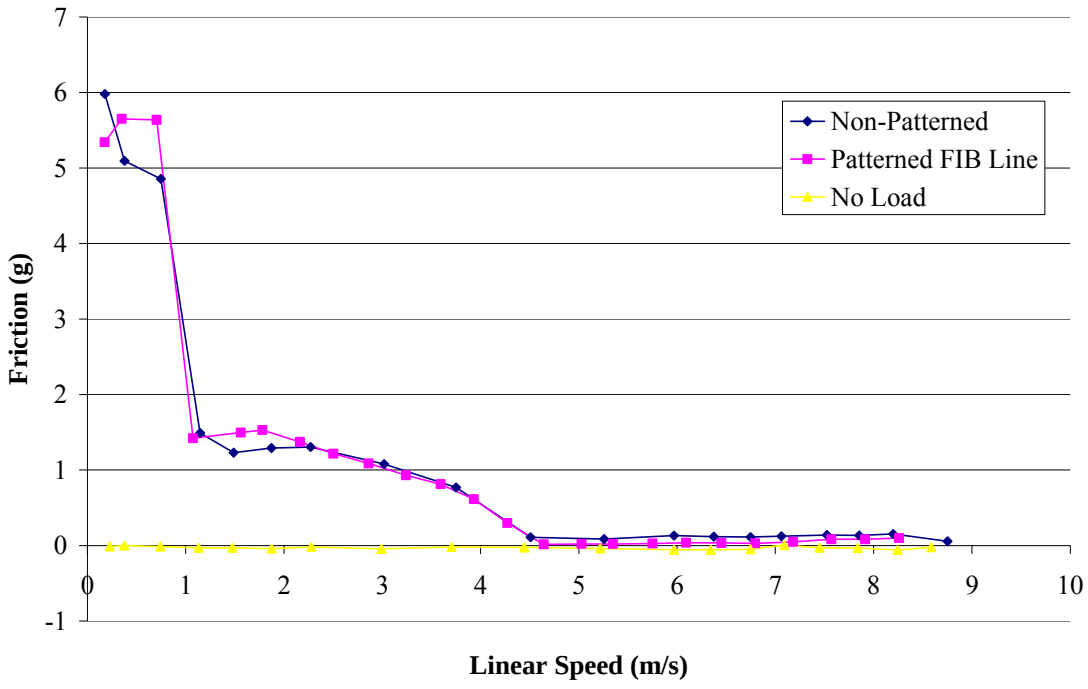

Figure 40: FIB High Density Whole Disk Calculation Results – Friction

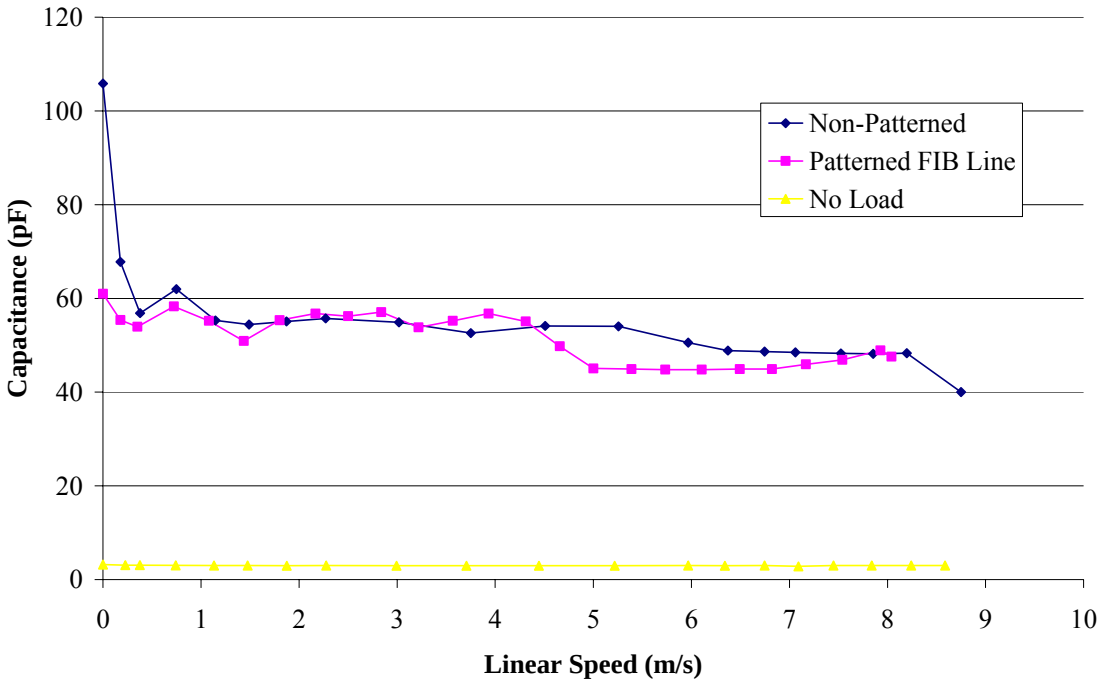

Figure 41: FIB High Density Whole Disk Calculation Results – Capacitance

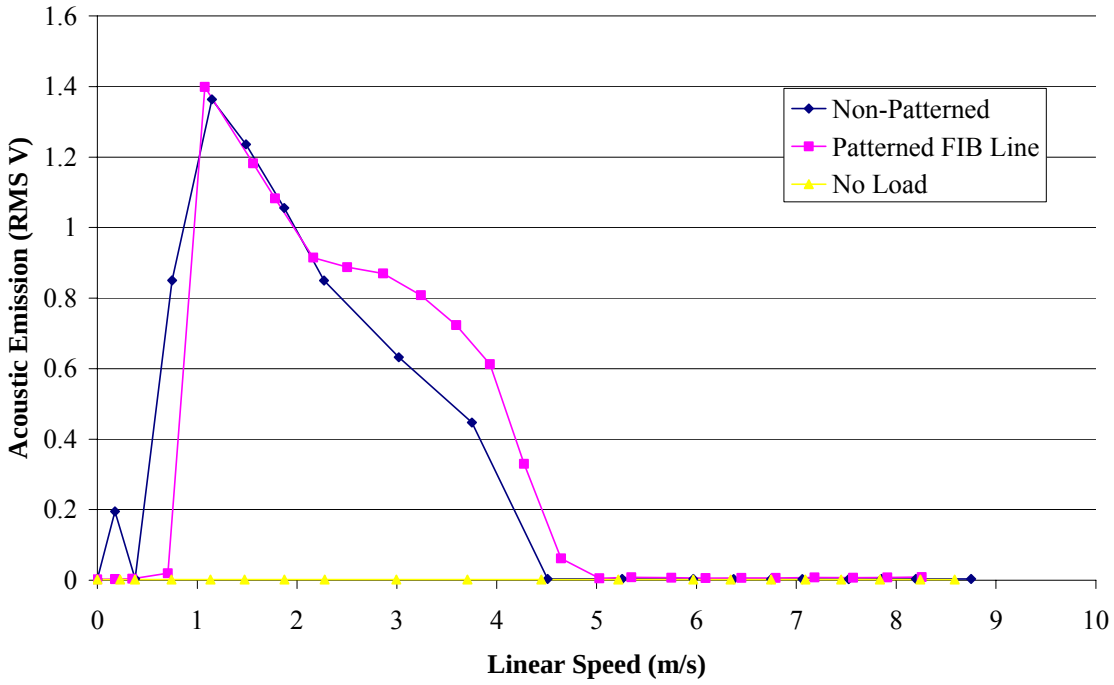

Figure 42: FIB High Density Whole Disk Calculation Results – Acoustic Emission

High density FIB whole disk friction results, Figure 40, are nearly identical to non-patterned data. Below 1 m/s friction is about 5.5 g. At 1 m/s it dramatically falls to 1.5 g, then continues a gentle arc to just more than near zero grams at 4.5 m/s. This is maintained up to 8.2 m/s.

Figure 41, high density FIB whole disk capacitance is generally of the same form as non-patterned data. Yet, the patterned data shows a small dip at 5 m/s that is not seen in the non-patterned data. This point could be an indicator of liftoff, but it could be argued that the change is insignificant because of its small size.

High density FIB whole disk AE, Figure 42, follows the non-patterned trend. A difference exists from 2.2-5 m/s, where the patterned data is roughly 30 % higher. Beyond 5 m/s AE is in line with the non-patterned, and no load data, at less than 10 mV RMS.

Overall, the FIB high density whole disk calculations agree more closely with the non-patterned data than the FIB low density results. All three data types agree and show lift off speed at 5 m/s.

5.3.3.2 FIB High Density 1 mm Region Calculation Results

In Figure 43, high density FIB regional friction results, the general trend follows the non-patterned data like the whole disk calculations. The curve generally looks less smooth than the non-patterned line. There are relatively large deviations at 1.6, 4.5, and 7.6 m/s. The point where friction appears to show lift off is delayed from 4.5 m/s to 5.1 m/s.

High density FIB regional capacitance results, in Figure 44, shows the same shape as the high density FIB whole disk calculations. The same dip is seen at 5 m/s which

could be considered lift off.

In Figure 45, high density FIB regional acoustic emission results, deviation from the non-patterned AE data starts slightly earlier than the whole disk results, at 1.8 m/s. Yet the difference between the whole disk and 1 mm region results is very small.

Overall, the 1 mm region calculations agree closely with the whole disk calculations. This speaks to the fact that the patterning had little effect on the liftoff speed or flyability of the sliders over FIB patterned material.

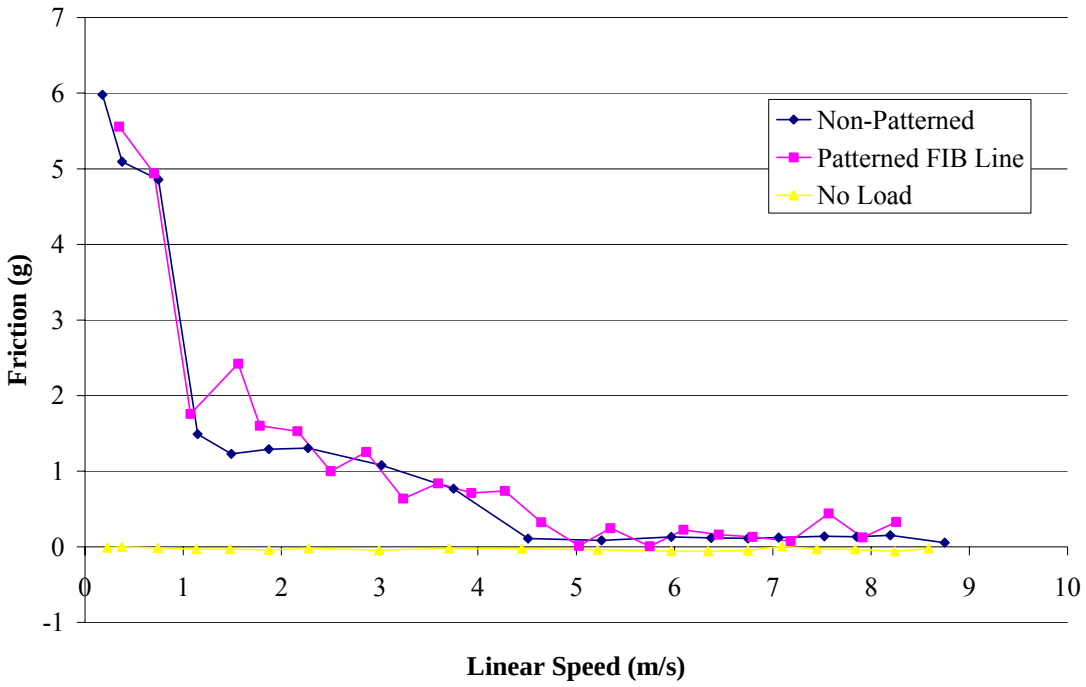

Figure 43: FIB High Density 1 mm Region Calculation Results – Friction

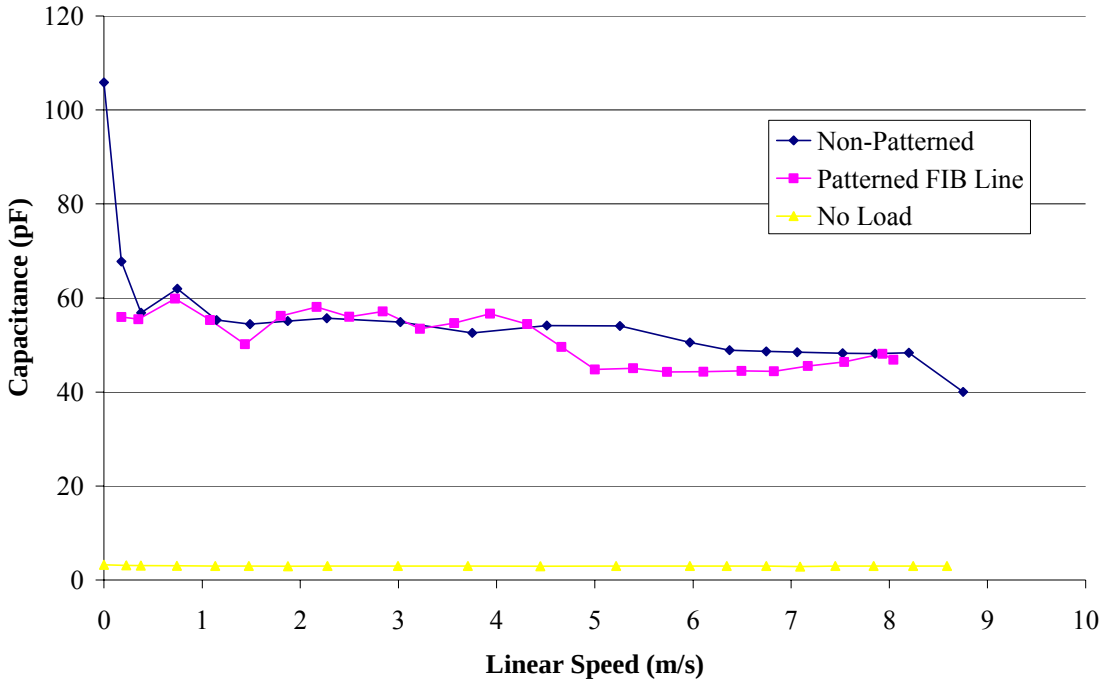

Figure 44: FIB High Density 1 mm Region Calculation Results – Capacitance

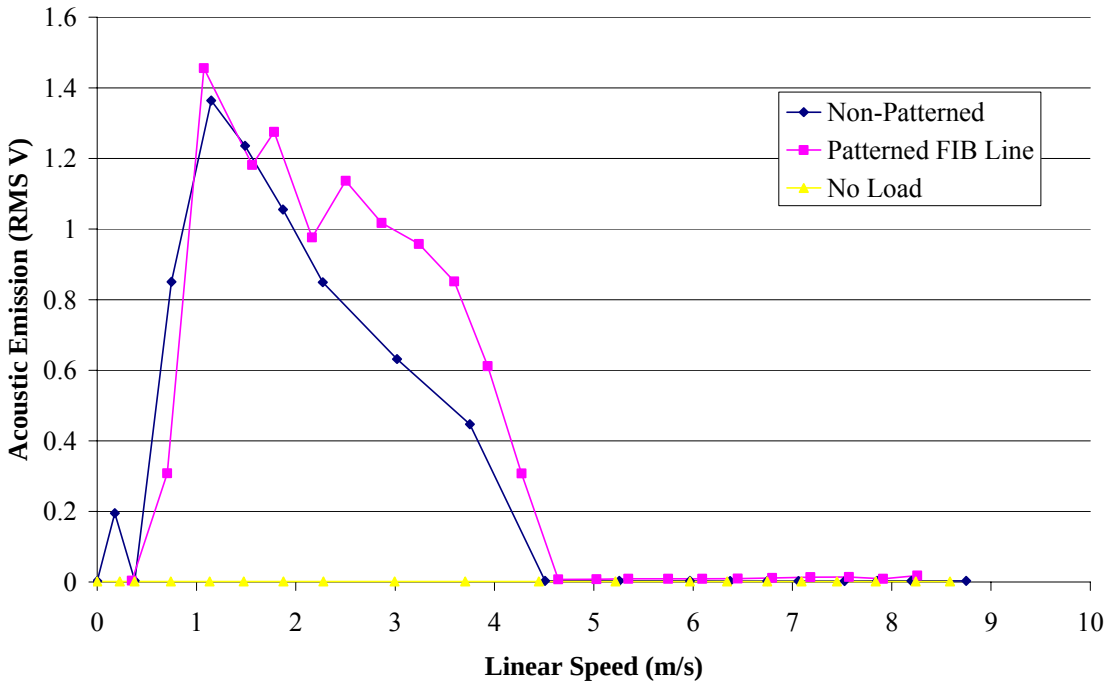

Figure 45: FIB High Density 1 mm Region Calculation Results – Acoustic Emission

5.3.4 Thin Film Self Assembly Experimental Results

The thin film self assembly tests were expanded to include no load, full load and half load results because full load results were inconsistent with that seen in FIB patterned samples. Results are broken down by amount of load.

5.3.4.1 Thin Film Self Assembly Full Load Results

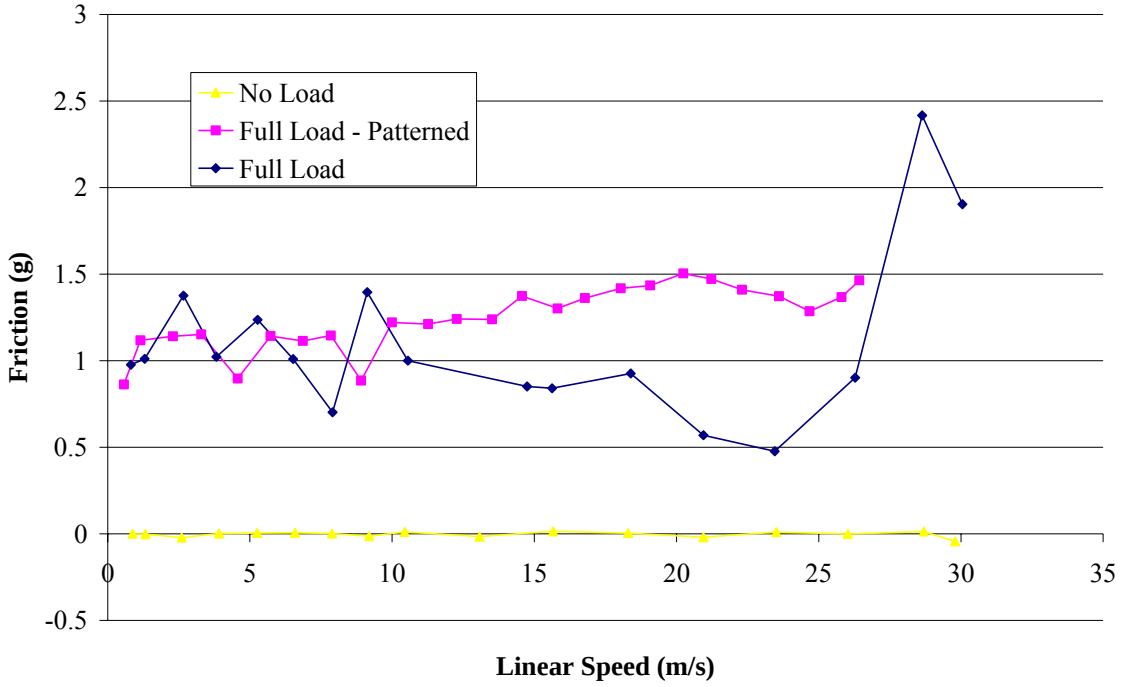

Figure 46: Thin Film Self Assembly Full Load Results – Friction

Full load results for both friction and acoustic emission do not show any take off point for either the non-patterned or patterned data. Friction values in Figure 46 range from 0.8 to 1.5 g. They never fall to the 0.2 g flying range that is seen in the friction baseline data, Figure 31. Full load AE data stays high until 23 m/s, then falls down to the flying level seen in Figure 33, but spikes again at 27 m/s. Overall, it appears that flying was not achieved. This motivated a second trial with the slider loaded to half of the design load to determine if hydrodynamic lubrication was in the boundary region.

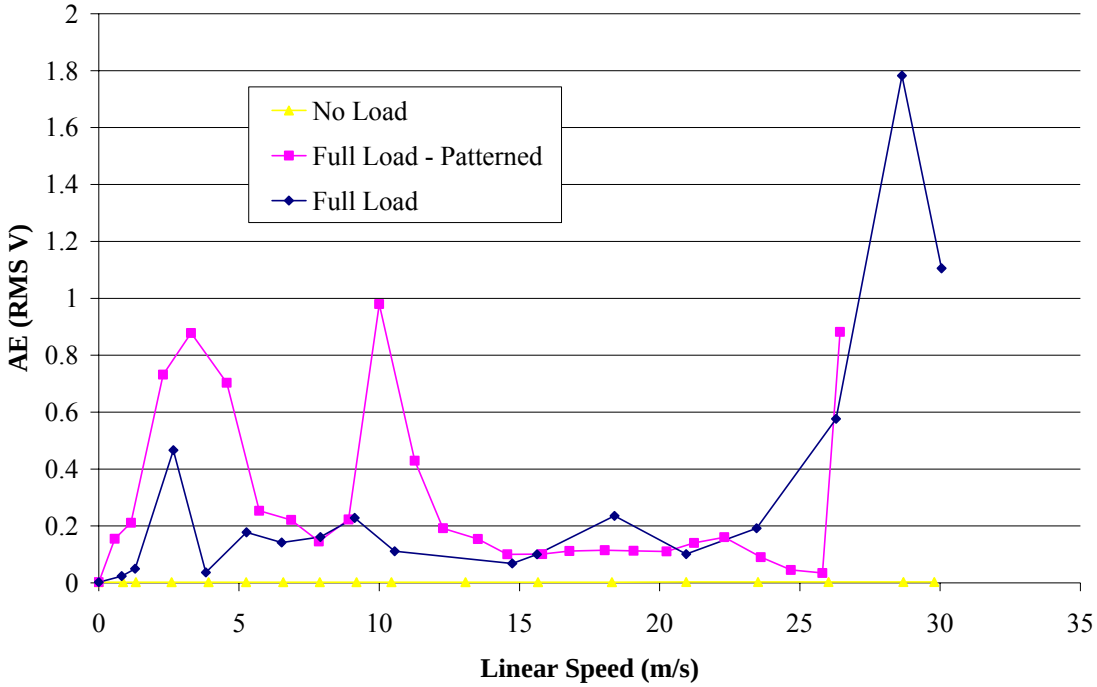

Figure 47: Thin Film Self Assembly Full Load Results – Acoustic Emission

5.3.4.2 Thin Film Self Assembly Half Load Results

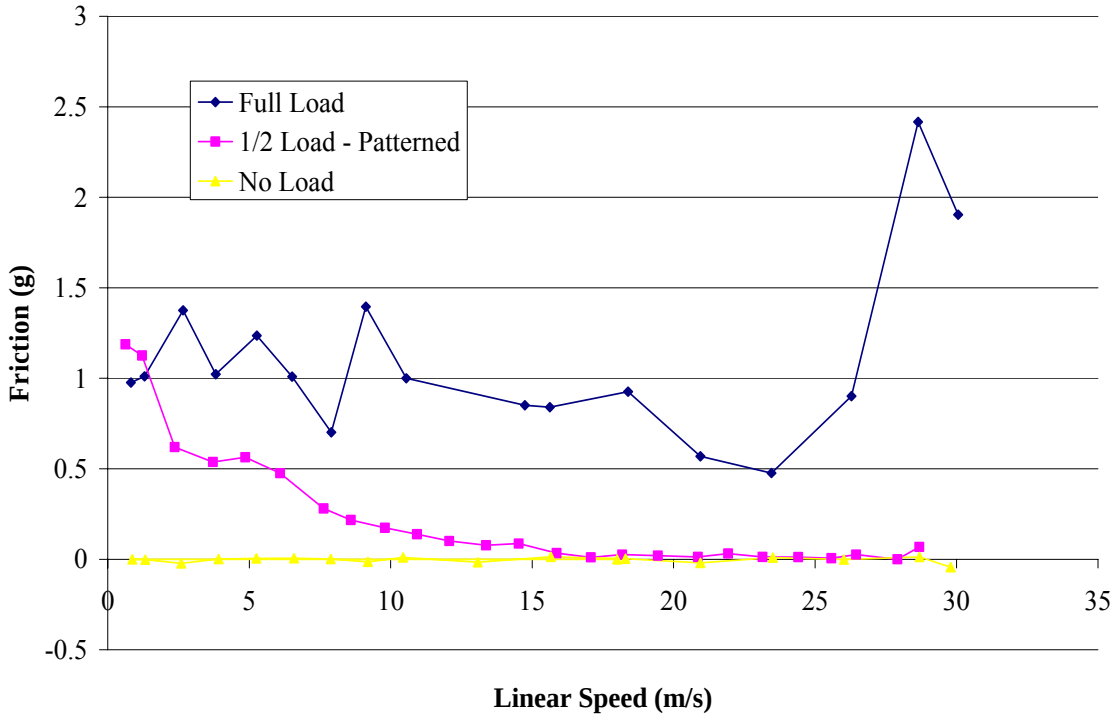

Figure 48: Thin Film Self Assembly Half Load Results – Friction

In Figure 48 and Figure 49 half load patterned data is plotted against full load non-patterned data and no load data. Friction, in Figure 48, for the slider at half design load appears to have a liftoff profile. The significant drop in friction is complete by 16 m/s. The corresponding acoustic emission data, Figure 49, does not show the same trend. At liftoff fly height is at a minimum, so, intermittent contact with the disk could be the reason.

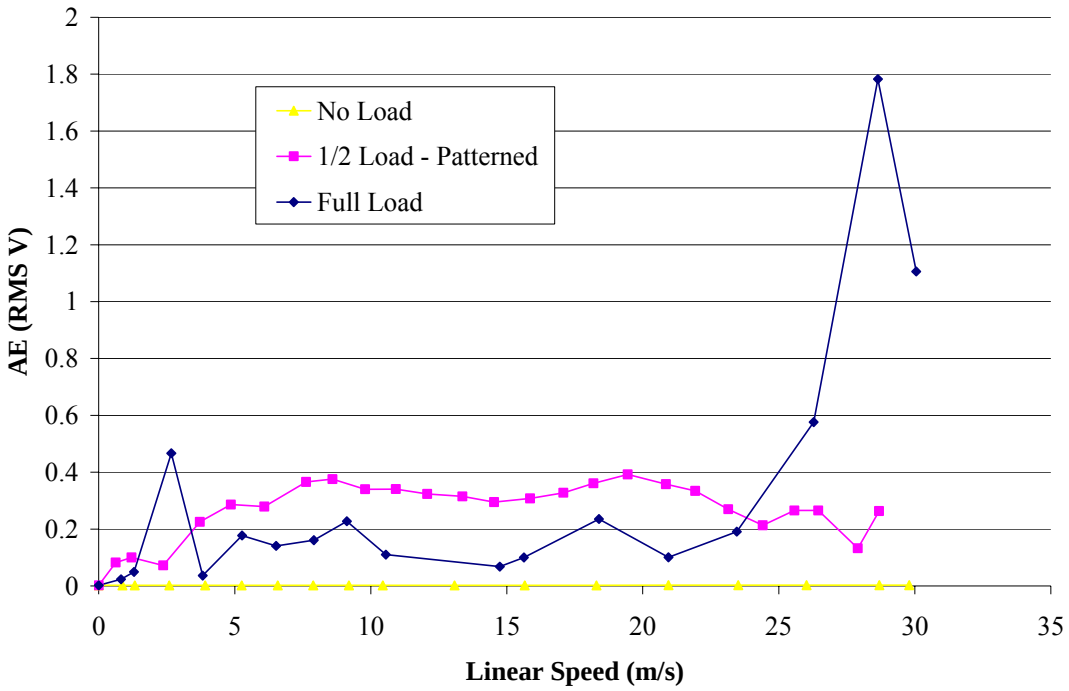

Figure 49: Thin Film Self Assembly Half Load Results – Acoustic Emission

As the speed, and therefore fly height, increases the intermittent contact should decrease. The rate at which this happens would be a function of the asperity size distribution on the disk. This is seen in Figure 49 beyond 21 m/s. This is one explanation of the data trend. However, this work does not advance the argument beyond speculation. An additional observation was made that there was no wear path formed during the experiment. This

supports the idea that flying was achieved, and that continued intermittent contact did not allow the AE data to drop down to flying levels.

5.4 General Discussion

Focused ion beam samples were patterned at 70 Mbit/in^2 (low density) and 10 Gbit/in^2 (high density). Flyability data for the low density sample was generally much rougher than the baseline data. However, a lift off speed was reached and the slider head was able to fly over the disk. The general roughness of the data could have been due to scratches made in shipping, yet it is thought that the scratches had negligible effect because data from a section of the disk known to be free of scratches displays the same trend.

Comparatively, the high density focused ion beam sample matched the baseline data almost identically for whole disk calculations as well as patterned region only calculations. Clearly, these two samples of FIB patterned media can support sufficient hydrodynamic lubrication to provide stable flight of the slider head.

The third patterned sample, created by thin film self assembly, did not provide such conclusive results. There is no data that shows lift off was achieved with the slider loaded to design specification.

At half of design load, the friction measurement takes on a profile that shows lift off near 16 m/s, yet the capacitance profile does not agree. One possible explanation is that lift was achieved but AE data did not decline in tandem because the asperity size distribution of the thin film patterned sample cause continued intermittent contact.

One primary difference between the FIB samples, that support stable flyability, and the thin film patterned sample, that does not clearly support flyability, is the

difference in the fraction of non-patterned media area, which can be called the conserved surface area ratio (CSAR). If the surface of the media is broken up into area that has and area that has not been etched then the conserved surface area ratio could be calculated as in Equation 3. If it is assumed that areas that are etched support no load bearing hydrodynamic pressure then the CSAR could be predictor of how well a particular patterned sample will allow a slider head to fly. Second, it must also be assumed that etched areas do not affect the hydrodynamic pressures generated at non-etched areas. Third the predictor assumes that the etched areas are very small compared to the air bearing surfaces on the slider head. If the etched surfaces were on the order of size as the air bearing surfaces then all hydrodynamic pressure would be lost when the slider passed over the etched area.

$$\frac{\text{total surface area - etched surface area}}{\text{total surface area}} = CSAR \tag{3}$$

The conserved area ratios for the three types of patterned samples are listed in Table 7.

Table 7: Conserved Surface Area Ratios for Experimental Samples

Sample	CSAR (ND)
FIB Low Density	0.69 (theoretical)
FIB High Density	0.50(theoretical)
Thin Film Patterned	0.15(experimental)

Considering CSARs for the three types of samples, it is more easily understood why the FIB samples provide better support for hydrodynamic lubrication.

CHAPTER 6

CONCLUSIONS

The purpose of this work was to determine flyability of current generation slider heads over patterned media. To that end, a test stand was created with normal load, friction, capacitance, acoustic emission and optical reflectivity sensors.

Three patterned samples were created. The first was made using Hitachi FB-2000A focused ion beam milling on a disk donated by Hitachi Global Storage Technologies. The pattern size was slightly larger than the slider to be tested with it. The density was 70 Mbit/in^2. The second sample was also made with the Hitachi FB-2000A on a disk donated by Hitachi Global Storage Technologies. The pattern area is in a speed bump configuration. This second sample was patterned at a density of 10 Gbit/in^2. The third sample was made using thin film self assembly over an entire 100 mm silicon wafer. It was patterned at a density of 700 Gbit/in^2. Slider samples with a design fly height of 13.5 nm were donated by Read Rite Corp. which has since been bought by Western Digital. Experiments with the three samples were taken using the test stand. Baseline data on a 4" disk was also taken to compare against.

The ability to achieve lift off was not affected by the patterned area on either FIB sample. However, the thin film self assembled sample was not able to achieve lift off with slider design load. Yet, the non-patterned silicon wafer was also not able to achieve liftoff at slider design load. However, at half design load the friction sensor appears to show lift off by 16 m/s, which is higher than reference liftoff speed of 7 m/s provided by Western Digital. The acoustic emission sensor does not show the same trend. This conflict could be explained by a nominal liftoff with continued intermittent head to disk

contact. As speed increases, acoustic emission drops off as a function of asperity height. This is seen in the data, which supports the continued intermittent contact theory.

A general predictor of a patterned media's ability to support hydrodynamic pressure is introduced as conserved surface area ratio (CSAR). CSAR is calculated as the total surface area minus the etched surface area all divided by the total surface area. This predictor is made based on three assumptions. First, etched areas support no hydrodynamic pressure. Second, etched areas do not affect hydrodynamic pressures generated at non-etched areas. Third, etched areas are very small compared to the air bearing surfaces of the slider. The closer CASR is to 1 the better it should be able to support hydrodynamic lift.

The low density FIB sample has a CASR of 0.7 while the high density FIB sample has as CASR of 0.5. Thin film patterned sample has a CASR of 0.15. Based on these numbers, the predictor agrees with the experimental data.

APPENDIX A: THEORETICAL AND EXPERIMENTAL STRAIN DERIVATION

Vertical Wheatstone Bridge Circuit (two active arm)

$$\varepsilon_{experimental} = \frac{2}{G} \cdot \frac{\left(\frac{V_{out}}{Gain}\right)}{V_{in}} \tag{4}$$

$$\varepsilon_{theoretical} = 6\frac{FL}{Ebh^2} \tag{5}$$

Where:

$L = 0.060m$

$E = 70GPa$

$b = 0.00635m$

$h = 0.00127m$

$G = 2.145$

$$\varepsilon_{experimental} = \frac{2}{2.145} \cdot \frac{\left(\frac{0.338}{1000}\right)}{4.9} = 64 * 10^{-6}$$

$$\varepsilon_{theoretical} = 6\frac{0.098 \cdot 0.060}{70 * 10^{9} \cdot 0.00635 \cdot 0.00127^2} = 49 * 10^{-6}$$

Horizontal Wheatstone Bridge Circuit (four active arm)

$$\varepsilon_{experimental} = \frac{1}{G} \cdot \frac{\left(\frac{V_{out}}{Gain}\right)}{V_{in}} \tag{6}$$

Where:

$L = 0.035m$

$E = 70GPa$

$b = 0.00635m$

$h = 0.00127m$

$G = 2.145$

$$\varepsilon_{experimental} = \frac{1}{2.145} \cdot \frac{\left(\frac{0.434}{1000}\right)}{4.9} = 41*10^{-6}$$

$$\varepsilon_{theoretical} = 6\frac{0.098 \cdot 0.00.035}{70*10^{9} \cdot 0.00635 \cdot 0.00127^{2}} = 28*10^{-6}$$

APPENDIX B: STIFFNESS RATIO DERIVATION

Vertical Measurement System

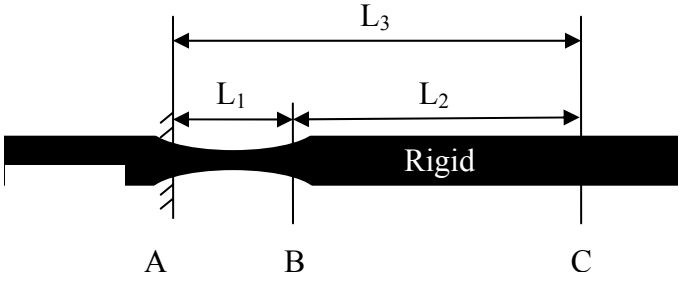

Figure 50: Schematic of Cantilever Beam #1

$$\delta_B = \frac{M_o L_1^2}{2EI} \tag{7}$$

$$\theta_B = \frac{M_o L_1}{EI} \tag{8}$$

$$\delta_C = \delta_B + L_2 \sin\theta_B \tag{9}$$

Substituting equation 7 and 8, into equation 9 produces:

$$\delta_C = \frac{M_o L_1^2}{2EI} + L_2 \sin\frac{M_o L_1}{EI} \tag{10}$$

$$M_o = F\ L_3 \tag{11}$$

$$I = \frac{bh^3}{12} \tag{12}$$

Then substituting equations 11 and 12 into equation 10,

$$\delta_C = \frac{F\ L_3 L_1^2}{2E\frac{bh^3}{12}} + L_2 \sin\frac{F\ L_3 L_1}{E\frac{bh^3}{12}} \tag{13}$$

Using the small angle approximation and simplifying reduces equation 10 to:

$$\delta_C = \frac{12F\ L_3 L_1}{Ebh^3}\left(\frac{L_1}{2} + L_2\right) \tag{14}$$

Solving equation 14 for $\frac{F}{\delta_C}$ produces:

$$K_{V,1} = \frac{F}{\delta_C} = \frac{Ebh^3}{12L_3 L_1\left(\frac{L_1}{2} + L_2\right)} \tag{15}$$

$$K_{H,1} = \frac{F}{\delta_C} = \frac{Ehb^3}{12L_3L_1\left(\frac{L_1}{2} + L_2\right)} \tag{16}$$

Where:

L_1 = 0.00635 m

L_2 = 0.05715 m

L_3 = 0.0635 m

E = 70 GPa

h = 0.00127 m

b = 0.00635 m

Horizontal Measurement System

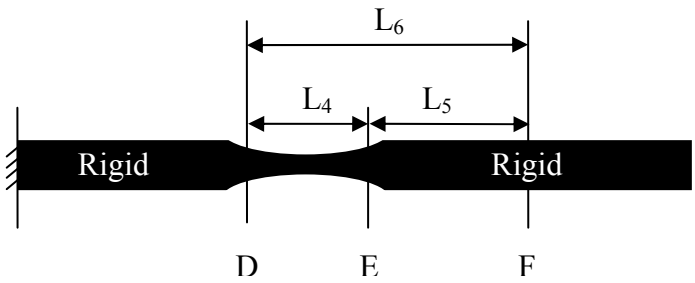

Figure 51: Schematic of Cantilever Beam #2

$$\delta_E = \frac{M_o L_4^2}{2EI} \tag{17}$$

$$\theta_E = \frac{M_o L_4}{EI} \tag{18}$$

$$\delta_F = \delta_E + L_5 \sin\theta_E \tag{19}$$

Substituting equation 17 and 18, into equation 19 produces:

$$\delta_F = \frac{M_o L_4^2}{2EI} + L_5 \sin\frac{M_o L_4}{EI} \tag{20}$$

$$M_o = F_H L_6 \tag{21}$$

$$I = \frac{bh^3}{12} \tag{22}$$

Then substituting equations 21 and 22 into equation 20,

$$\delta_F = \frac{F_H L_6 L_4^2}{2E\frac{bh^3}{12}} + L_5 \sin\frac{F_H L_6 L_4}{E\frac{bh^3}{12}} \tag{23}$$

Using the small angle approximation and simplifying reduces equation 23 to:

$$\delta_F = \frac{12 F_H L_6 L_4}{Ebh^3}\left(\frac{L_4}{2} + L_5\right) \tag{24}$$

Solving equation 24 for $\frac{F_H}{\delta_H}$ produces:

$$K_{H,2} = \frac{F_H}{\delta_H} = \frac{Ebh^3}{12L_6L_4\left(\frac{L_4}{2} + L_5\right)} \tag{25}$$

$$K_{V,2} = \frac{F_H}{\delta_H} = \frac{Ehb^3}{12L_6L_4\left(\frac{L_4}{2} + L_5\right)} \tag{26}$$

Where:

L_4 = 0.00635 m

L_5 = 0.03048 m

L_6 = 0.0638 m

E = 70 GPa

h = 0.00127 m

b = 0.00635 m

APPENDIX C: ACOUSTIC EMISSION SENSOR CALIBRATION CERTIFICATE

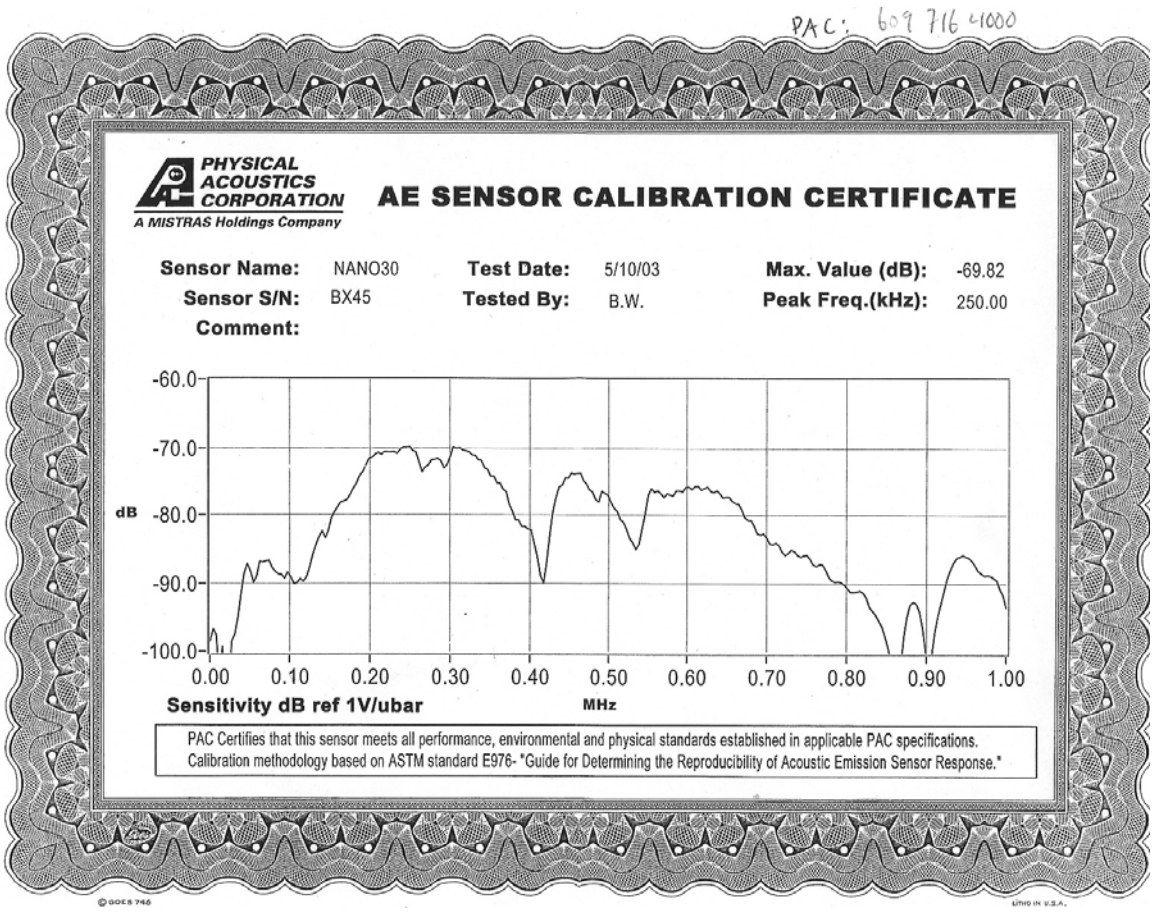

Figure 52: Acoustic Emission Sensor Calibration Certificate

APPENDIX D: MODEL WITH SYSTEM CAPACITANCE FOR HEAD TO DISK INTERFACE CAPACITANCE MEASUREMENT CIRCUIT

$$V_{out} = \frac{z_1}{z_{total}} V_{in} \tag{27}$$

$$z_1 = \frac{1}{\frac{1}{R} + j\omega C_s} \tag{28}$$

$$z_{total} = \frac{1}{j\omega C_I} + R_I + \frac{1}{\frac{1}{R} + j\omega C_s} \tag{29}$$

$$\frac{V_{out}}{V_{in}} = \frac{z_1}{z_{total}} = \frac{\frac{1}{\frac{1}{R} + j\omega C_s}}{\frac{1}{j\omega C_I} + R_I + \frac{1}{\frac{1}{R} + j\omega C_s}} \tag{30}$$

Simplifying produces:

$$\lambda = \frac{V_{out}}{V_{in}} = \frac{j\omega C_I R}{1 - \omega^2 C_S C_I R R_S + j\omega(C_s R + C_I R_I + C_I R)} \tag{31}$$

$$\lambda^2 = \left(\frac{j\omega C_I R}{1 - \omega^2 C_S C_I R R_S + j\omega(C_s R + C_I R_I + C_I R)} \right)^2 \tag{32}$$

Solving above equation for quadratic form with respect to C_I produces:

$$C_I^2\left(\lambda^2\omega^4 C_S^2 R^2 R_I^2 + 2\lambda^2\omega^2 R R_I + \lambda^2\omega^2 R_I^2 + (\lambda^2 - 1)\omega^2 R^2\right) + C_I(2\lambda^2\omega^2 C_S R^2) + (\lambda^2 + \lambda^2\omega^2 C_S^2 R^2) = 0 \quad (33)$$

APPENDIX E: PHYSICAL MODEL FOR HEAD TO DISK INTERFACE CAPACITANCE MEASUREMENT CIRCUIT AND MAXIMIZING SENSITIVITY AROUND EXPECTED CAPACITANCE

$$V_{out} = \frac{R}{R + \frac{1}{j\omega C}} V_{in} \tag{34}$$

Let $$\lambda = \frac{V_{out}}{V_{in}} \tag{35}$$

$$\lambda = \frac{V_{out}}{V_{in}} = \frac{R}{R + \frac{1}{j\omega C}} \tag{36}$$

$$\lambda^2 = \frac{R^2}{\left(R + \frac{1}{j\omega C}\right)^2} \tag{37}$$

Simplifying

$$\lambda^2 = \frac{\omega^2 C^2 R^2}{\omega^2 C^2 R^2 + 2\omega RC + 1} \tag{38}$$

Let λ=0.5, then

$$3(\omega^2 C^2 R^2) = 2\omega RC + 1 \tag{39}$$

Let $\gamma = \omega R$

$$3\gamma^2 C^2 - 2\gamma C - 1 = 0 \tag{40}$$

Using the quadratic formula to solve for γ:

$$\gamma = \frac{2C \pm \sqrt{4C^2 - 4(3C^2)(-1)}}{6C^2} \tag{41}$$

Simplifying

$$\gamma = \frac{1 \pm 2}{3C} \tag{42}$$

Since $\gamma = \omega R$ can't be negative, then

$$\gamma = \frac{1}{C_{EXPECTED}} \approx 2E9 \tag{43}$$

This can be solved for any combination of input frequency, ω, and shunt resistance *R*, such that ω**R* equals one over the expected capacitance.

APPENDIX F: SOFTWARE MASK FOR LOW DENSITY FIB SAMPLE

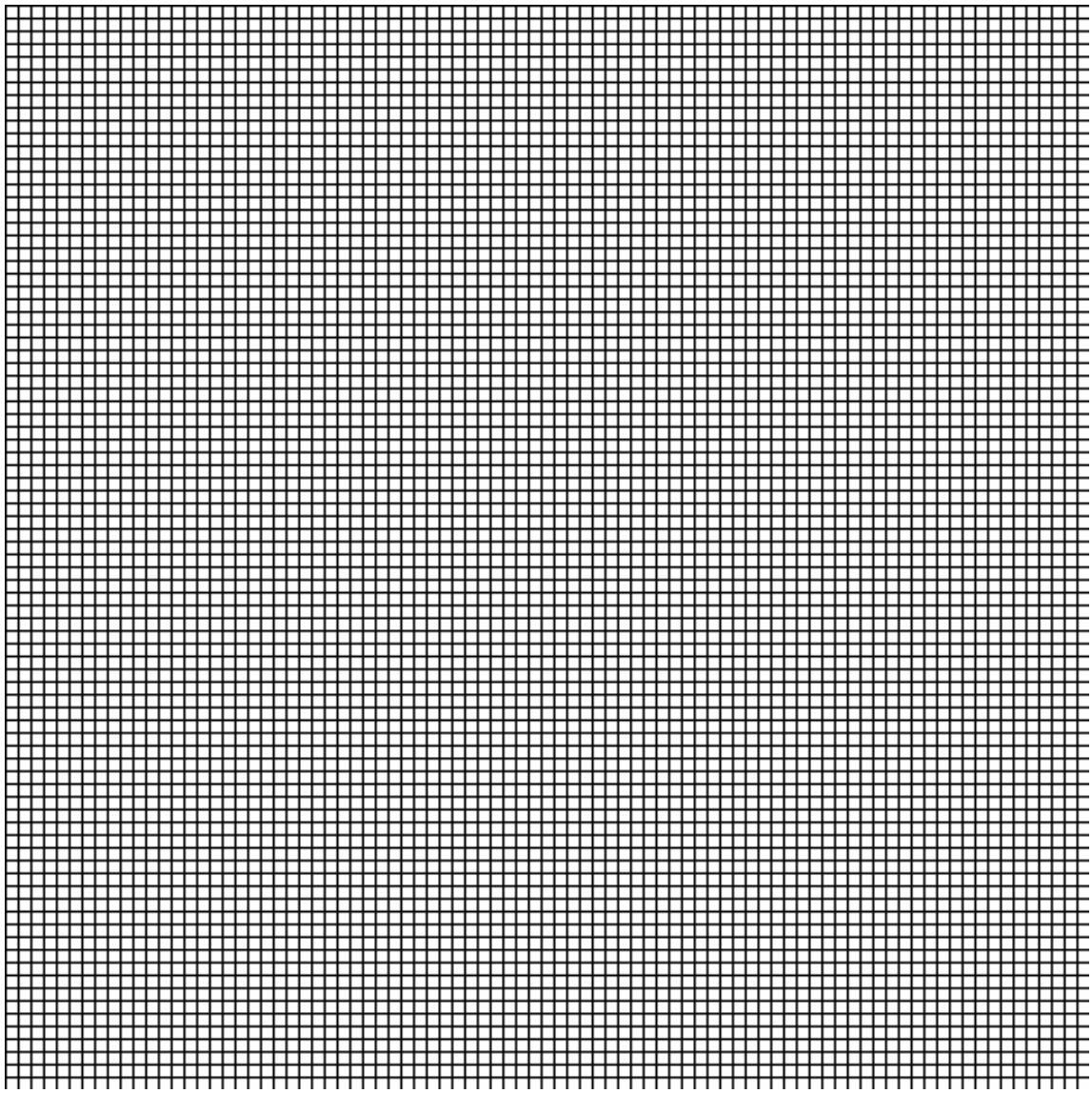

Figure 53: Software Mask for Low Density FIB Sample

APPENDIX G: SOFTWARE MASK FOR HIGH DENSITY FIB SAMPLE

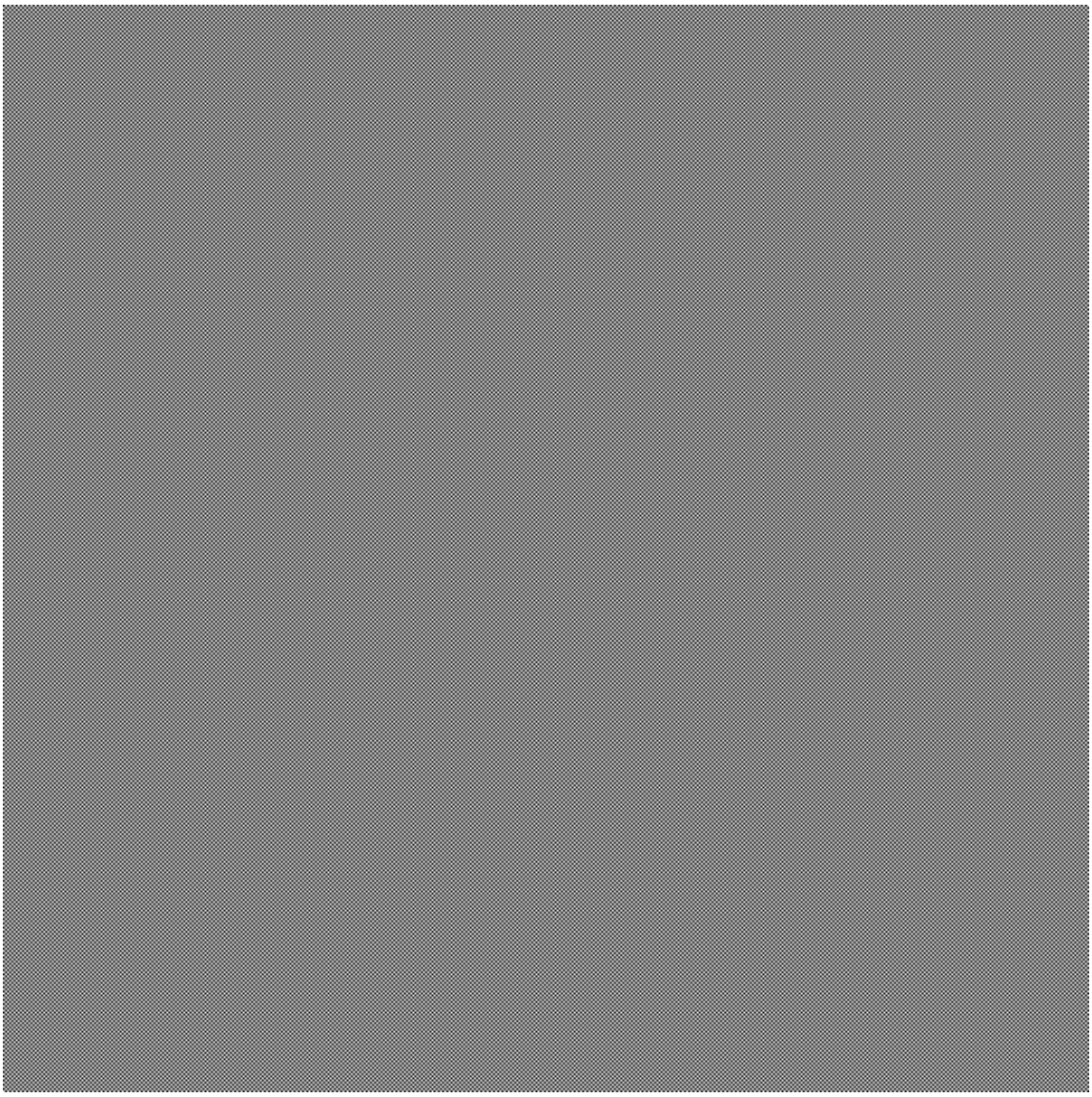

Figure 54: Software Mask for High Density FIB Sample

APPENDIX H: OPTICAL IMAGES OF SLIDER HEADS

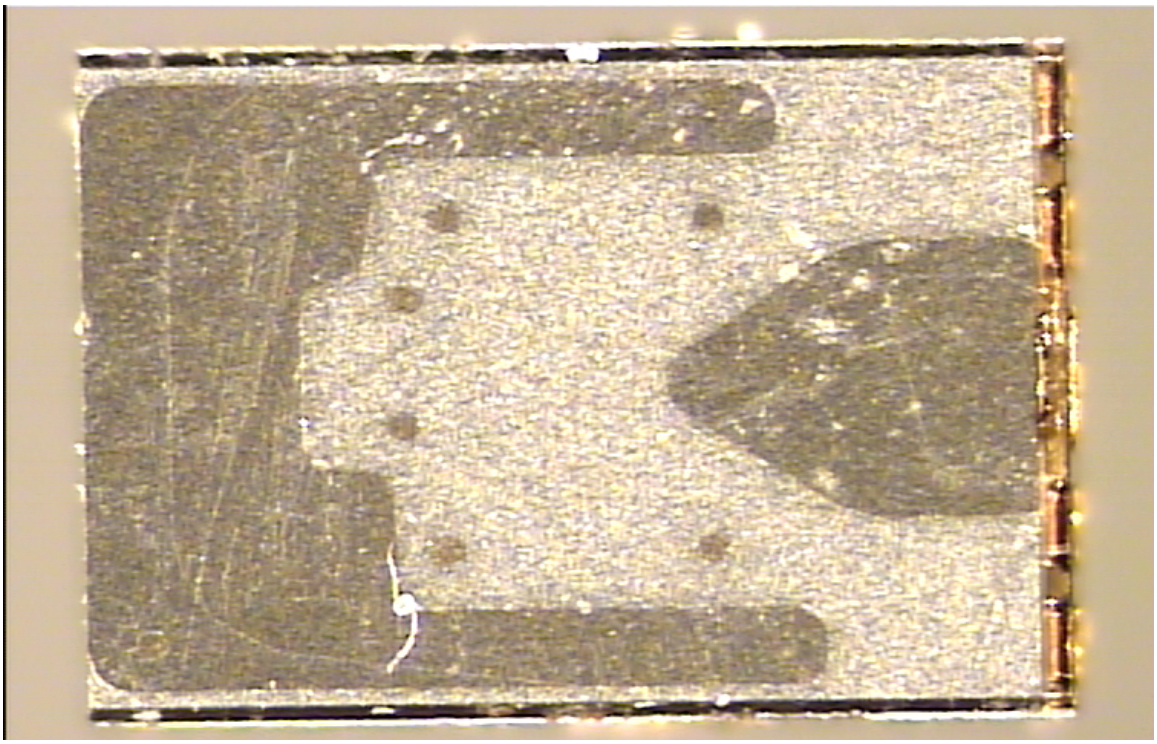

Figure 55: Air Bearing Surface, Style #1

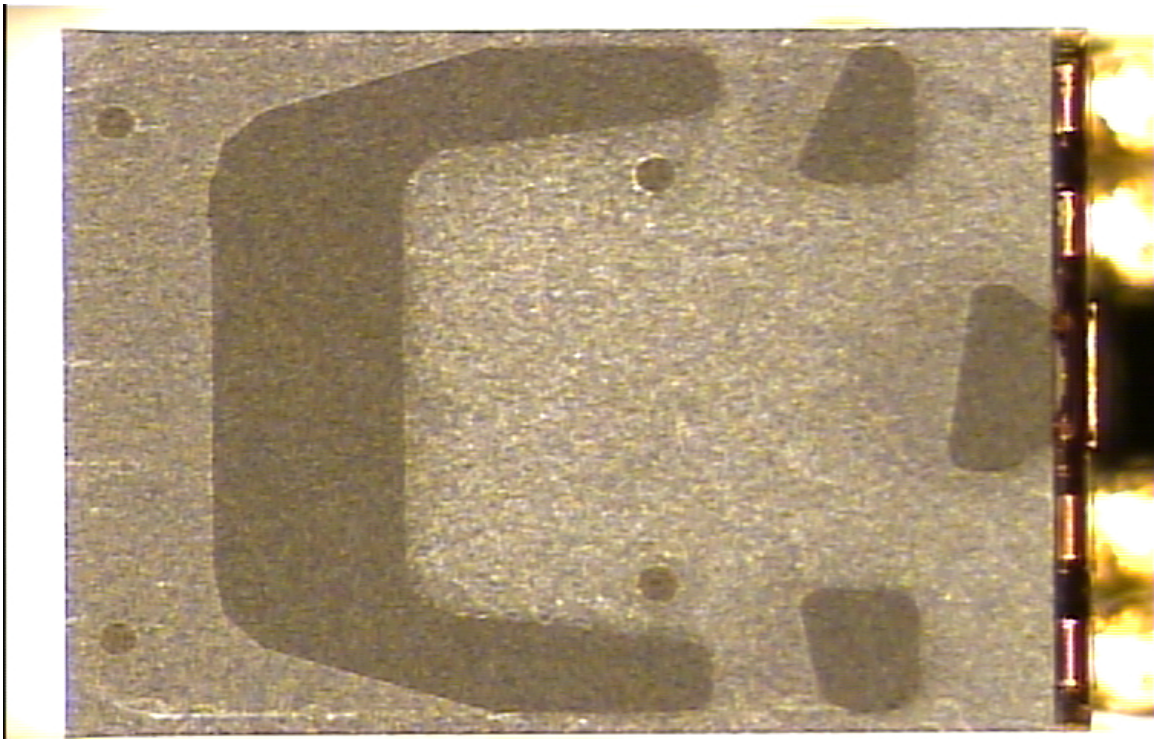

Figure 56: Air Bearing Surface, Style #2

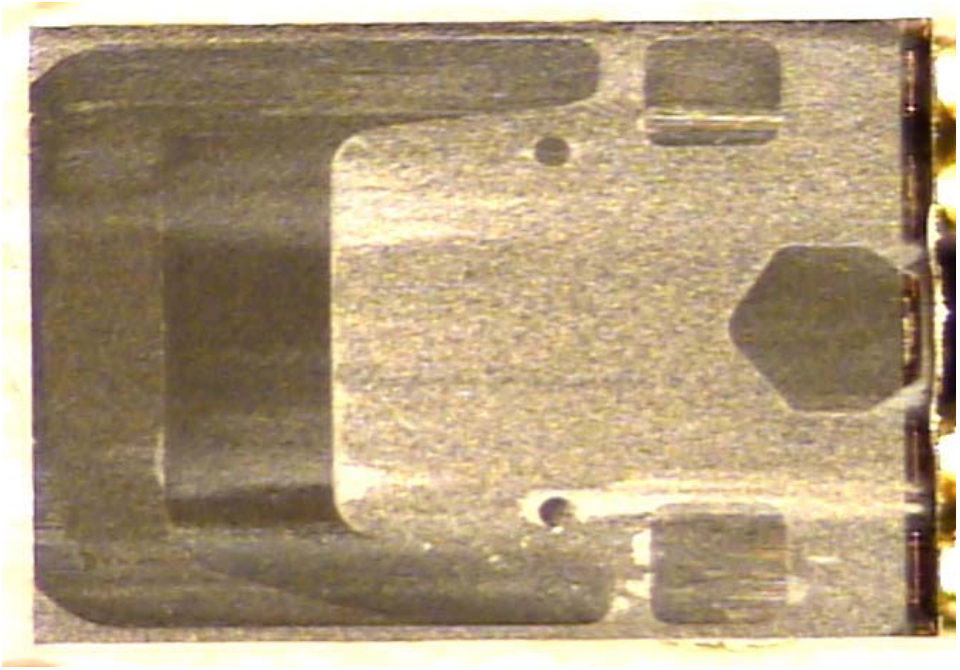

Figure 57: Air Bearing Surface, Style #3 (After Use)

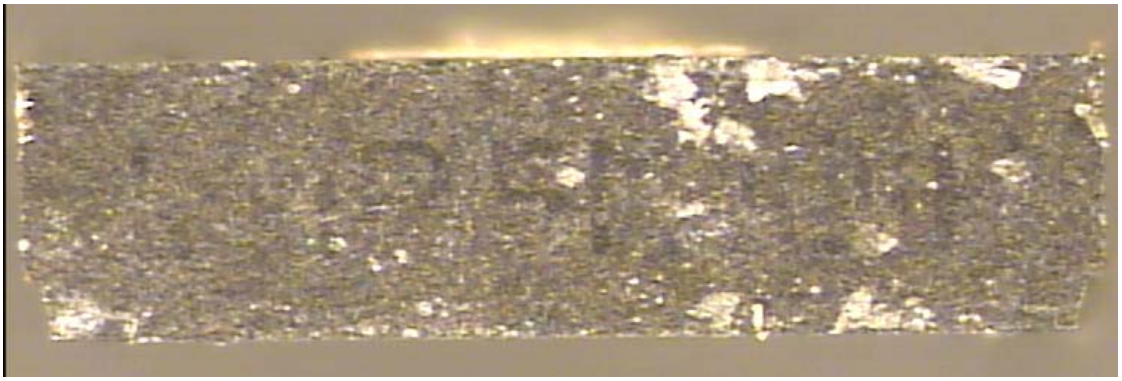

Figure 58: Front View of Slider Head

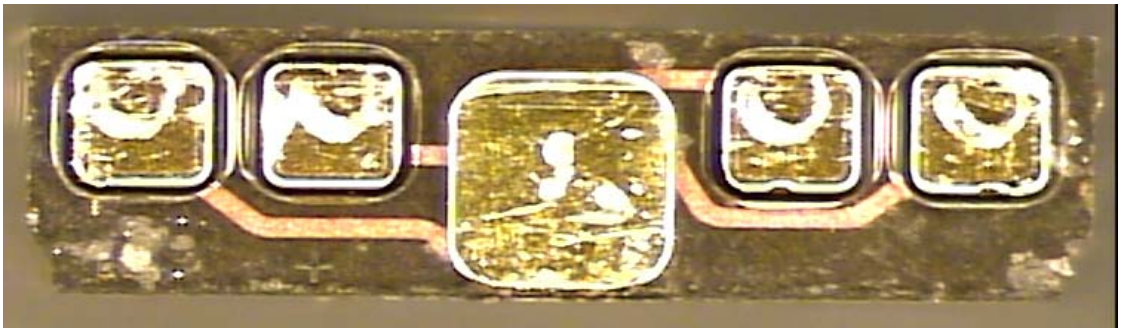

Figure 59: Back View of Slider Head

REFERENCES

[1] A. Moser, K. Takano, D.T. Margulies, M. Albrecht, Y. Sonobe, Y. Ikeda, S. Sun, E.E. Fullerton, "Magnetic Recording: Advancing into the Future," Journal of Physics D: Applied Physics, v. 35, pp. R157-R167, 2002.

[2] D. Weller, A. Moser, "Thermal Effect Limits in Ultrahigh-Density Magnetic Recording," IEEE Transactions on Magnetics, v. 35 n. 6, pp. 4423-4439, 1999.

[3] S.H. Charap, P.-L. Lu, Y. He, "Thermal Stability of Recorded Information at High Densities," IEEE Transactions on Magnetics, v. 33 n. 1, pp. 978-982, 1997.

[4] H.F. Hamann, Y.C. Martin, H.K. Wickramasinghe, "Thermally Assisted Recording Beyond Traditional Limits," Applied Physics Letters, v. 84 n. 5, pp. 810-812, 2004.

[5] S.H. Charap, P.L. Lu, Y. He, "Thermal Stability of Recorded Information at High Densities," IEEE Transactions on Magnetics, v.33, pp. 978-983, 1997.

[6] D. Weller, A. Moser, "Thermal Effect Limits In Ultrahigh Density Magnetic Recording," IEEE Transactions on Magnetics, v.35, pp. 4423-4439, 1999.

[7] H. Fang, "Micromagnetic Studies of Thermal Stability of Media Signal and Noise," IEEE Transactions on Magnetics, pp.AA-02

[8] K. Ouchi, N. Honda, "Overview of Latest Work on Perpendicular Recording Media," IEEE Transactions on Magnetics, v. 36 n. 1, pp. 16-22, 2000.

[9] S.-I. Iwasaki, "Perpendicular Magnetic Recording," IEEE Transactions on Magnetics, v. MAG-16 n. 1, pp. 71-76, 1980.

[10] L. Wang, S. Li, J.H. Giusti, J. Fernandez-de-Castro, "Micromagnetic study of effect of media intergranular exchange interaction in perpendicular recording," Journal of Applied

Physics, v. 91 n. 10, pp.8381-8383, 2002.

[11] M.J. Madou, *Fundamentals of Microfabrication, Second Edition*. CRC Press; Boca Raton, Florida, 2002.

[12] C.T. Rettner, S. Anders, T. Thomson, M. Albrecht, Y. Ikeda, M.E. Best, B.D. Terris, "Magnetic Characterization and Recording Properties of Patterned $Co_{70}Cr_{18}Pt_{12}$ Perpendicular Media, IEEE Transactions on Magnetics, v. 38 n. 4, pp.1725-1730, 2002.

[13] J.-G. Zhu, X. Lin, L. Guan, W. Messner, "Recording, Noise, and Servo Characteristics of Patterned Thin Film Media," IEEE Transactions on Magnetics, v. 36 n. 1, pp.23-29, 2000.

[14] J. Lohau, A. Moser, C.T. Rettner, M.E. Best, B.D. Terris, "Effect of Ion Beam Patterning on the Write and Read Performance of Perpendicular Granular Recording Media," IEEE Transactions on Magnetics, v. 37 n. 4, pp. 1652-1656, 2001.

[15] S. Anders, S. Sun, C.B. Murray, C.T. Rettner, M.E. Best, T. Thomson, M. Albrecht, J.-U. Thiele, E.E. Fullerton, B.D. Terris, "Lithography and Self-Assembly for Nanometer Scale Magnetism," Microelectronic Engineering, v. 61-62, pp. 569-575, 2002.

[16] M. Albrecht, A. Moser, C.T. Rettner, S. Anders, T. Thomson, B.D. Terris, "Writing of High-Density Patterned Perpendicular Media with a Conventional Longitudinal Recording Head," Applied Physics Letters, v. 80 n. 18, pp. 3409-3411, 2002.

[17] C.T. Rettner, M.E. Best, B.D. Terris, "Patterning of Granular Magnetic Media with a Focused Ion Beam to Produce Single-Domain Islands at > 140 Gbit/in^2", IEEE Transactions on Magnetics, v. 37 n. 4, pp. 1649-1651, 2001.

[18] K.W. Guarini, C.T. Black, S.H.I. Yeung, "Optimization of Diblock Copolymer Thin Film Self Assembly," Advanced Materials, v.14 n. 18, pp.1290-1294, 2002.

[19] F.S. Bates, G.H. Fredrickson, "Block Copolymers-Designer Soft Materials," Physics Today, pp. 32-38, 1999.

[20] D.G. Walton, G.J. Kellogg, A.M. Mayes, P. Lambooy, T.P. Russell, "A Free Energy Model for Confined Diblock Copolymers," Macromolecules, v. 27, pp. 6225-6228, 1994.

[21] H. Yokohama, T.E. Mates, E.J. Kramer, "Structure of Asymmetric Diblock Copolymers in Thin Films," Macromolecules, v. 33, pp. 1888-1898, 2000.

[22] G.J. Kellogg, D.G. Walton, A.M. Mayes, P. Lambooy, T.P. Russell, P.D. Gallagher, S.K. Satija, "Observed Surface Energy Effects in Confined Diblock Copolymers," Physical Review Letters, v. 76 n. 14, pp. 2503-2506, 1996.

[23] P. Mansky, T.P. Russell, C.J. Hawker, J. Mays, D.C. Cook, S.K. Satija, "Interfacial Segregation in Disordered Block Copolymers: Effect of Tunable Surface Potentials," Physical Review Letters, v. 79 n. 2, pp. 237-240, 1997.

[24] P. Mansky, Y. Liu, E. Huang, T.P. Russell, C. Hawker, "Controlling Polymer–Surface Interactions with Random Copolymer Brushes," Science, v. 275, pp. 1458-1460, 1997.

[25] K.W. Guarini, C.T. Black, K.R. Millkove, R.L. Sandstrom, "Nanoscale Patterning Using Self-Assembled Polymers for Semiconductor Applications," Journal of Vacuum Science Technology, v. 19 n. 6, pp. 2784-2788, 2001.

[26] S.Y. Chou, "Patterned Magnetic Nanostructures and Quantized Magnetic Disks," Proceedings of the IEEE, v. 85 n. 4, pp. 652-671, 1997.

[27] J.L. Streator, J. Huang, J. Zheng, "High Shear Rate Response of Thin Lubricant Films

in a Slider-Disk Interface," Thinning Films and Tribological Interfaces, pp.285-291, 2000.

[28] Polymer Source, 124 Avro Street, Dorval (Montreal) Quebec, H9P 2X8, Canada.

[29] http://www.sigmaaldrich.com

[30] J.L. Streator, "Considerations of a Simplified Analysis of Transducer Dynamics for Measuring Friction," Journal of Tribology, v. 114 n. 2, pp. 360-369, 1992.